VERIFICATION OF SIMULATED DSDS AND SENSITIVITY TO CCN CONCENTRATION IN ENKF ANALYSIS AND ENSEMBLE FORECASTS OF THE 30 APRIL 2017 TORNADIC QLCS DURING VORTEX-SE

by

Connor Paul Belak

A Thesis

Submitted to the Faculty of Purdue University

In Partial Fulfillment of the Requirements for the degree of

Master of Science

Department of Earth, Atmospheric, and Planetary Sciences

West Lafayette, Indiana

May 2021

THE PURDUE UNIVERSITY GRADUATE SCHOOL
STATEMENT OF COMMITTEE APPROVAL

Dr. Daniel Dawson II, Chair

Department of Earth, Atmospheric, & Planetary Sciences

Dr. Robin Tanamachi

Department of Earth, Atmospheric, & Planetary Sciences

Dr. Michael Baldwin

Department of Earth, Atmospheric, & Planetary Sciences

Approved by:

Dr. Daniel J. Cziczo

ACKNOWLEDGMENTS

This research would not be possible without the funding support of National Oceanic and Atmospheric Administration grant NA18OAR4590313. I want to first thank my primary advisor, Daniel Dawson. Thank you for allowing me to be a member of your research group, for the countless hours spent helping me with research and revising this thesis, and for challenging me to fulfill my full potential. I would also like to thank my committee members, Robin Tanamachi and Michael Baldwin, for their guidance and insight.

I am grateful for those who provided assistance to me throughout this research. Qin Jiang and Milind Sharma provided help with several coding aspects of this project for which I am appreciative of their expertise. I would also like to thank Edward Mansell for his insight regarding the NSSL-TM microphysics scheme as well as VORTEX-Southeast participants who helped with the planning and deployment of the PIPS. The numerical experiments would not be possible without the help and guidance of the Information Technology at Purdue (ITaP) Research Computing staff.

I would like to express a special thank you to you, Susie. These words do not do justice for the patience you have graced me with over the years. Thank you for all of the support you gave me even when I did not know I needed it. I love you and would not be where I am today without your constant encouragement.

Finally, I would especially like to express my deepest gratitude to my parents for pushing me to be my best and helping me achieve my dreams. Without them, none of this would have been possible.

Thank you, and always keep your eye on the sky.

TABLE OF CONTENTS

LIST OF TABLES

LIST OF FIGURES

ABSTRACT

Storms in the SE-US often evolve in different environments than those in the central Plains. Many poorly understood aspects of these differing environments may impact the tornadic potential of SE-US storms. Among these differences are potential variations in the CCN concentration owing to differences in land cover, combustion, industrial and urban activity, and proximity to maritime environments. The relative influence of warm and cold rain processes is sensitive to CCN concentration, with higher CCN concentrations producing smaller cloud droplets and more efficient cold rain processes. Cold rain processes result in DSDs with relatively larger drops from melting ice compared to warm rain processes. Differences in DSDs impact cold pool and downdraft size and strength, that influence tornado potential. This study investigates the impact of CCN concentration on DSDs in the SE-US by comparing DSDs from ARPS-EnKF model analyses and forecasts to observed DSDs from portable disdrometer-equipped probes collected by a collaboration between Purdue University, the University of Oklahoma (OU), the National Severe Storms Laboratory (NSSL), and the University of Massachusetts in a tornadic QLCS on 30 April 2017 during VORTEX-SE.

The ARPS-EnKF configuration, which consists of 40 ensemble members, is used with the NSSL triple-moment microphysics scheme. Surface and radar observations are both assimilated. Data assimilation experiments with CCN concentrations ranging from 100 cm^{-3} (maritime) to 2,000 cm^{-3} (continental) are conducted to characterize the variability of DSDs and the model output DSDs are verified against the disdrometer observations. The sensitivity of the DSD variability to CCN concentrations is evaluated. Results indicate continental CCN concentrations (close to CCN 1,000 cm^3) produce DSDs that align closest to the observed DSDs. Other thermodynamic variables also accord better to observations in intermediate CCN concentration environments.

CHAPTER 1. INTRODUCTION

1.1 VORTEX-SE background and motivation

The epicenter of tornado related fatalities in the United States (U.S.) is centered over the southeastern United States (SE-US) (Ashley 2007). The disproportionally large number of tornado fatalities across this region has been attributed to SE-US tornadoes often occurring before the nationwide climatological "peak" tornado season, at night, and in densely forested and populated areas with insufficient shelters, increasing the vulnerability of the population (Ashley 2007; Ashley 2008). As a result, the need arose for a greater understanding of severe storm environments in the SE-US and the Verification of the Origin of Rotation in Tornadoes EXperiment-Southeast (VORTEX-SE) field campaign was introduced.

One of the overarching goals of VORTEX-SE is to collect datasets on SE-US severe and tornadic storm environments. A majority of what is known about severe storms and tornadoes stems from studies focused on the central Plains; however, SE-US storms evolve in different thermodynamic and moisture environments than their better-studied counterparts of the central Plains (Rasmussen 2015). A differentiating characteristic of SE-US tornadic storm environments is the increased frequency of lower convective available potential energy (CAPE) compared to the central Plains (Davis and Parker 2014). High CAPE environments can still occur in the SE-US.

CAPE measures the instability of the atmosphere and gives an approximation of updraft strength within a thunderstorm, with larger CAPE values representing an increasingly unstable atmosphere capable of producing a stronger updraft. Low CAPE values coupled with high wind shear are referred to as high-shear, low-CAPE (HSLC) environments (Sherburn and Parker 2014). SE-US HSLC environments differ from central Plains environments, which commonly consist of high-shear, high-CAPE (HSHC) (Thompson et al. 2004, 2013; Schneider et al. 2006). HSLC

environments are defined as having a 0–6-km shear vector magnitude ≥ 18 m s^{-1} and surface-based (SB) and mixed layer (ML) CAPE between 0–500 J kg^{-1} (Sherburn and Parker 2014). HSLC environments occur frequently, but the SE-US accounts for the highest percentage of HSLC environments that produce severe thunderstorms and tornadoes (Davis and Parker 2014; Anderson-Frey et al. 2019).

Microphysical processes may be sensitive to the different thermodynamic and moisture aspects of the environment in the SE-US and thus may produce different drop size distributions (DSDs) relative to elsewhere. The development of the cold pool, precipitation rates, the size and strength of downdrafts, and tornado potential are all influenced by changes in the size and shape of the DSD (e.g., Gilmore et al. 2004; Dawson et al. 2010, 2015, 2016; Friedrich et al. 2013; Kumjian et al. 2015). These processes and their sensitivities are not well understood in the SE-US.

To understand the microphysics of convective storms, knowledge of DSDs is essential. DSDs provide insight into which microphysical processes could be occurring in a storm, such as collision, coalescence, drop breakup, and evaporation, which alter the DSD shapes (Kalina et al. 2014). DSDs vary not only within storms, but also between different environments. Since cloud condensation nuclei (CCN) concentration is at a minimum over the open ocean and gradually increases as the distance inland increases (Fig. 1.1), the CCN concentration in the SE-US could be different from the central Plains due to uncertainty surrounding how quickly CCN concentration increases inland away from the Gulf of Mexico (e.g., Rauber 2003; Yue et al. 2019; Spracklen et al. 2011). Additionally, the higher frequency of industrial and metropolitan areas in the SE-US could lead to higher CCN concentrations than the central Plains as observed in Fig. 1.1 (Spracklen et al 2011). Different CCN concentrations can result in different DSDs (Andreae et al. 2004; Tao et al. 2012; Jouan and Milbrandt 2019). DSDs are sensitive to the CCN concentration due to the

latter's effects on the relative influence of warm and cold rain processes (e.g., Squires and Twomey 1966; Warner and Twomey 1967; Warner 1968; Rosenfeld and Woodley 2000; Rosenfeld and Ulbrich 2003; Andreae et al. 2004; Tao et al. 2012). Higher CCN concentrations yield more efficient cold rain processes with relatively larger drops from melting ice compared to warm rain processes (e.g., Squires 1958; Squires and Twomey 1966; Warner and Twomey 1967; Warner 1968; Rosenfeld 1999; Rosenfeld and Ulbrich 2003; Andreae et al. 2004; Tao et al. 2012).

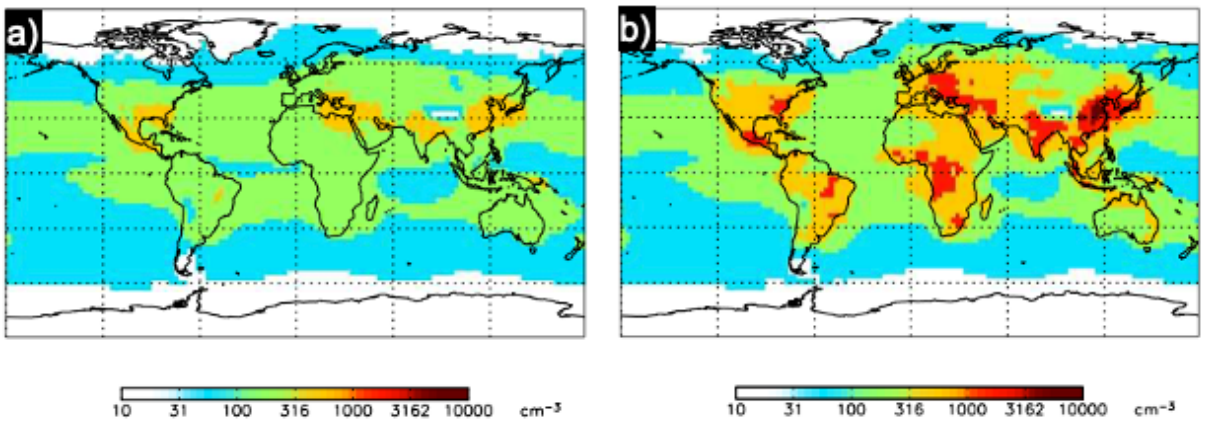

Figure 1-1. The simulated annual mean surface CCN concentration for model simulations (a) without carbonaceous aerosol acting as CCN; (b) with carbonaceous aerosol acting as CCN. This image was adapted from Fig. 1 in Spracklen et al. 2011.

1.2 QLCS events in the SE-US

While HSLC environments can support discrete supercells that produce tornadoes, they often produce quasi-linear convective systems (QLCS) with embedded supercells and tornadoes. The term QLCS is an all-encompassing term for describing linear convective systems (e.g., squall lines, bow echoes, and mesoscale convective systems). Mature QLCSs have a region of enhanced winds that travel from some higher level in the rear of the system in the stratiform precipitation region towards the surface in the front of the QLCS (Fig. 1.2), known as the rear-inflow-jet (RIJ)

(Smull and Houze 1987). The RIJ forms in response to the updraft being tilted upshear over the cold pool, causing an acceleration of air downshear to the front of the system (Weisman 1992). A strong RIJ can cause bowing segments along the leading edge of the QLCS as was the case for the 30 April 2017 QLCS (Fig 1.3).

Mesovortices are sometimes observed on the leading edge of QLCSs. Leading mesovortices are favorable locations for tornado development and have been observed by Weisman and Trapp (2003) as having strengths comparable to supercells. Climatologically, discrete cellular tornadoes have the highest frequency of occurrence in the central Plains, whereas QLCS tornadoes have the highest frequency of occurrence east of the central Plains, over the Ohio Valley and Mississippi River Valley region (Smith et al. 2012). QLCS tornadoes are more likely during the cool season (January through March) than supercellular tornadoes (Smith et al. 2012). The main difference between QLCS mesovortices and supercell mesocyclones is that QLCS vortices typically form near the ground, expand upward, and are not as long-lived as mid-level rotating updrafts associated with mesocyclones in supercells (Mahale et al. 2012). Not all mesovortices present in QLCSs produce tornadoes; however, stronger, longer-duration, and vertically deeper mesovortices are more likely to do so (e.g., Atkins et al. 2004; Sherburn and Parker 2019).

Numerous QLCSs impact the SE-US every year. However, there are few known numerical simulation studies of QLCSs across the VORTEX-SE domain that assimilate radar data. Therefore, such studies are desirable to analyze the storm-scale environment and storm-scale processes in a manner that is not currently feasible in real time but allows for more direct comparisons and verification with observations. This is part of the motivation for this study in which data assimilation is performed in a numerical model of a tornadic QLCS on 30 April 2017.

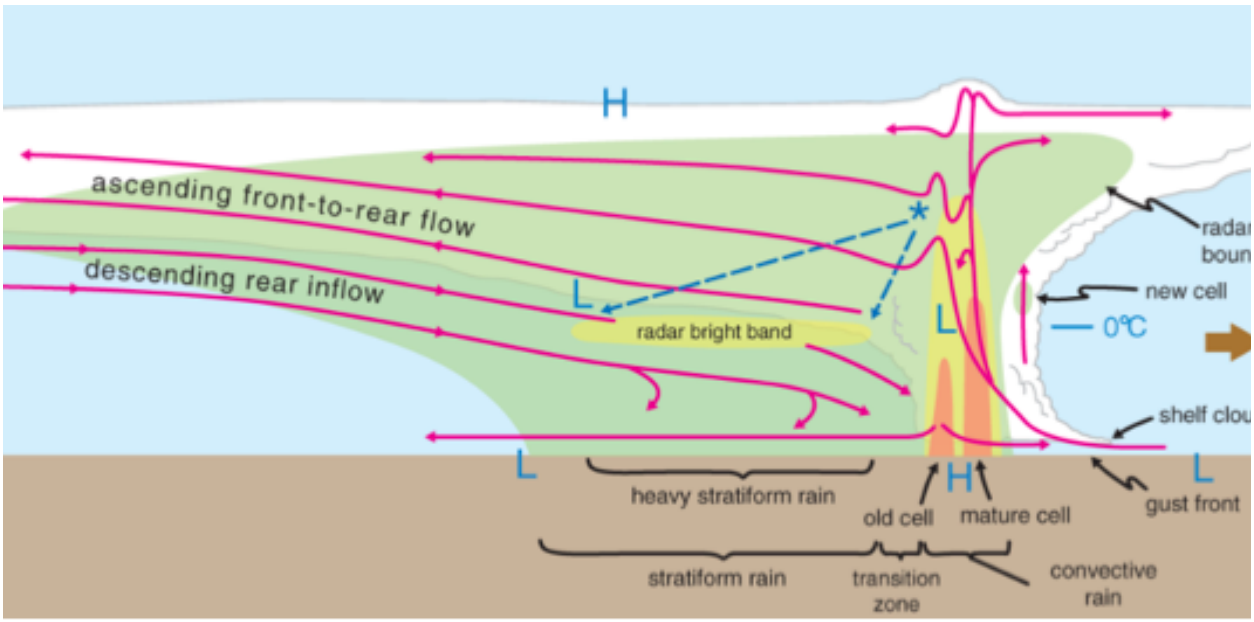

Figure 1-3. A cross section of a squall line. This image is from Markowski and Richardson (2010), which was adapted from Houze et al. (1989).

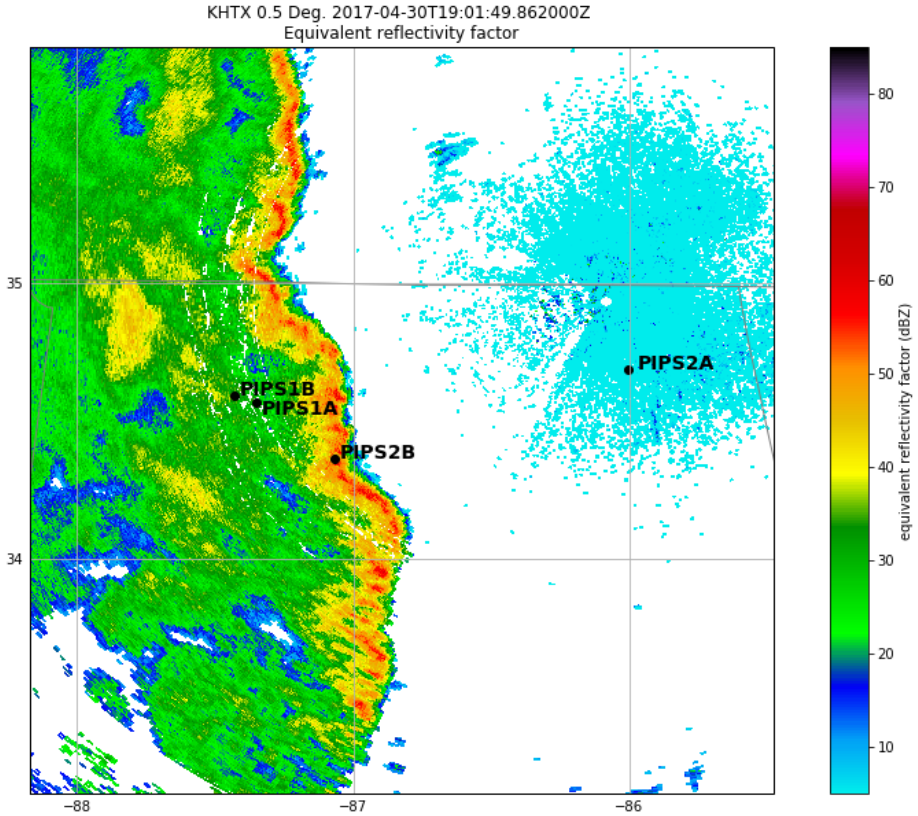

Figure 1-2. The 0.5° *Z* from the Huntsville, Alabama WSR-88D (KHTX) of the 30 April 2017 QLCS at 1902 UTC.

1.3 SE-US vulnerabilities

Brotzge and Erickson (2010) concluded that QLCSs have a higher ratio of unwarned tornadoes than discrete storms. Compared to HSHC environments, HSLC environments have a higher false alarm ratio and lower probability of detection (Dean and Schneider 2008). HSLC environments have proved to be a forecasting challenge because conventional forecasting metrics, such as those used by National Weather Service (NWS) offices, perform poorly in HSLC environments (Sherburn and Parker 2014). This is in part because the Weather Surveillance Radar-1988 Doppler (WSR-88D) network may not be able to observe small circulations at large distances away from the radar or close to the ground (Davis and Parker 2012). Additionally, upper-level flow is stronger during the cold season resulting in faster storm motion and decreased warning lead times, increasing the region's vulnerability (Ashley 2007).

Aside from forecasting challenges, differences exist between the geographic landscape and socioeconomic makeup of the SE-US and central Plains. Ashley et al. (2008) suggests the high tornado fatality rate in the SE-US (Fig 1.4c) could be due to SE-US tornadoes occurring primarily overnight during the cold season, because the public is not as likely to receive severe weather alerts while asleep. The fatality rate is nearly doubled for nocturnal tornadoes when compared to those that occur during the daytime (e.g., Ashley 2007; Ashley et al. 2008; Brotzge and Erickson 2010).

Unlike the Great Plains, the SE-US is densely forested with numerous orographic features (hills, lakes, etc.) (Brotzge and Erickson 2010). These features coupled with low cloud bases make identifying tornadoes difficult for both the general public and trained storm spotters, especially at night (Ashley et al. 2008). Moreover, the SE-US tornado season occurs before the nationwide climatological peak, when the population is least expecting severe weather (Ashley 2007). Adding to the SE-US's susceptibility is a higher percentage of mobile homes or homes with weak framing, compared to other regions in the U.S. (Ashley 2007). Mobile homes account for over 40% of all

tornado fatality locations (Ashley et al. 2008). This, along with a higher elderly population and larger percentage of the population living under poverty, results in increased vulnerability (Ashley 2007). Therefore, understanding the environments in which SE-US tornadic storms form is crucial to warn the public of impending severe weather events with as much lead time as possible. The SE-US vulnerabilities were a large motivation for VORTEX-SE (Rasmussen 2015).

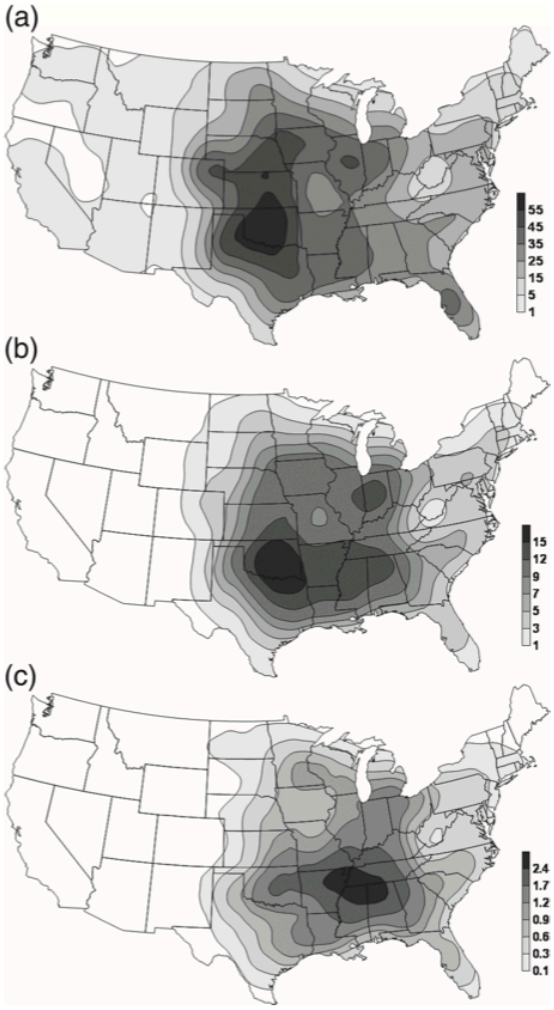

Figure 1-4. The smoothed frequency of (a) tornadoes, (b) F/EF2 + tornadoes, and (c) deadly tornado events from 1950-2004 from Ashley (2007).

1.4 Motivation for this study

The primary goal of VORTEX-SE is to improve the understanding of SE-US tornadoes, their parent storms, and the environments in which they form; this includes how microphysical processes in the SE-US may be influenced by the environment differently than in the Great Plains (Rasmussen 2015). Most studies concentrating on the feedbacks between microphysics and cold pool dynamics in severe convective storms have focused on HSHC environments, while HSLC environments have received comparatively less attention. DSDs and associated impacts on downdraft and cold pool properties, and potential tornadogenesis likely contain different sensitivities in HSLC vs. HSHC environments.

While thermodynamic differences related to microphysical variations can be assessed using observations, an alternative method to understand the storm scale environment is through numerical simulations that assimilate environmental data, such as radar data and surface observations. Numerical simulations allow for an in-depth examination of storm scale processes and environments that are not feasible in real time from existing observational networks. Various model parameters can be changed allowing different processes to be turned on, off, or isolated and therefore better understood. While numerical simulations are beneficial, there are numerous assumptions made regarding the configuration of parameterization schemes selected in the model to best represent microphysical and other physical processes.

The underlying bulk microphysics parameterization (BMP) scheme influences several characteristics of simulated storm behavior including the cold pool size and strength (e.g., Gilmore et al. 2004; Snook and Xue 2008). Many BMP schemes represent the size spectra of each precipitating hydrometeor using the standard gamma distribution:

$$N(D) = N_0 D^{\mu} e^{-\lambda d} \quad (1)$$

where $N(D)$ $(mm^{-1}m^{-3})$ is the *DSD, D* is the sphere equivalent volume diameter (*mm*), N_0 is the intercept parameter ($mm^{-1\,\mu}\,m^{-3}$), λ is the slope parameter (mm^{-1}), and μ is the distribution shape parameter (Ulbrich 1983). Prognostic equations are required for one or more of the moments of the distribution function to predict changes in the distribution by predicting changes of these parameters (Milbrandt and Yau 2005a, 2005b). To determine the three parameters explicitly, three separate predictive moment equations are required.

Therefore, the National Severe Storms Laboratory (NSSL) triple-moment (NSSL-TM) microphysics scheme is used in this study (Mansell et al. 2010; Dawson et al. 2014). When the number of predicted moments in the gamma size distribution is set to three in the NSSL-TM microphysics scheme so that all three free parameters of the gamma size distribution are prognosed, a more physically realistic representation of size sorting and other microphysical processes (i.e., collision, coalescence, drop breakup, rain evaporation, and melting of hail) is achieved (e.g., Dawson et al. 2010, 2014).

As in all BMPs, numerous assumptions are made in the NSSL-TM scheme. The most obvious of which is that gamma size distributions adequately represent the range of DSDs in the real world; this is corroborated by numerous studies, but deviations from a standard gamma size distribution are known to exist (e.g. Thurai et al. 2018). Other assumptions include how rain DSDs evolve through collision and coalescence, how rain DSDs are initialized from the melting and shedding of hail, to name a few. The comparison of model simulated DSDs from the NSSL-TM microphysics scheme with observed DSDs is a useful way of verifying the assumptions lead to a solution close to observations. The verification of model output DSDs with observed DSDs has also not been explored in great detail, leading to additional motivation for this study.

Thus, the Advanced Regional Prediction System (ARPS) (e.g., Xue et al. 2000, 2001, 2003) coupled with an ensemble Kalman filter (EnKF) (Tong and Xue 2005) data assimilation system will use the NSSL-TM microphysics scheme to model the tornadic QLCS that moved over the VORTEX-SE domain in northern Alabama on 30 April 2017. Simulations with CCN concentrations ranging from 100 cm^{-3} (maritime) to 2000 cm^{-3} (continental) are conducted to characterize the variability of DSDs and the model output DSDs are verified against the disdrometer observations. In addition to DSD parameters, thermodynamic and kinematic variables are also compared to observations from the Purdue/OU/NSSL Portable In-situ Precipitation Stations (PIPS). The sensitivity of the DSD variability to CCN concentrations is evaluated. Better understanding of how microphysical processes impact DSDs and influence the cold pool in storms in the SE-US will allow for HSLC environments to be better modeled, which will result in increased situational awareness for NWS meteorologists and in turn, improve tornado predictability, warnings, and inherently save lives.

It is hypothesized (1) the NSSL-TM scheme will accurately represent the range of DSDs present in disdrometer observations as quantified by various DSD related parameters between model output and observations; and (2) the SE-US severe storm environment may be best modeled by CCN concentrations similar to those of the central Plains.

CHAPTER 2. BACKGROUND

2.1 Data assimilation

The goal of data assimilation in meteorology is to establish the best possible state of the atmosphere using a combination of observations and short-range forecasts. Data assimilation is usually a sequential procedure where a previous model forecast (called the "background") is statistically combined in some optimal manner with newly received observations to produce an improved analysis of the atmospheric state. A new forecast is then generated from this state (Park and Liang 2013). Common data assimilation methods include three-dimensional data assimilation (3DVAR), four-dimensional data assimilation (4DVAR), and the ensemble Kalman filter (EnKF) among others. The initial conditions generated through data assimilation and how the initial conditions are derived are an important aspect of a Numerical Weather Prediction (NWP) model (e.g., Kalnay 2003; Dawson and Xue 2006; Park and Liang 2013).

2.1.1 Background of data assimilation

Early attempts at data assimilation proceeded manually by interpolating observations to a regular grid that was then digitized (e.g., Richardson 1922; Charney et al. 1950). The need for a less tedious and time intensive objective analysis was evident, leading to the development of automatic interpolation methods that fit observations to a grid (Kalnay 2003). Nonetheless, a problem quickly arose; not enough data were available to initiate operational primitive equations in models via the spatial interpolation of observations into regular grids (Kalnay 2003).

A complete first guess at all grid points is required including locations with irregularly spaced data or data-lacking locations in less populated regions (Bergthorsson et al. 1955). The first guess, otherwise known as the prior information or background field, is the best approximation of

the state of the atmosphere before using observations (Park and Liang 2013). Originally, climatology (possibly combined with a short-range model forecast) was used as the first guess (Bergthorsson et al. 1955). However, as model forecasting skill increased, short-range forecasts were increasingly used alone as the first guess.

2.1.2 Data assimilation methods

Data assimilation using a short-range forecast as the first guess is essential in transporting data from data-heavy to data-sparse regions and providing a four-dimensional state of the atmosphere (Park and Liang 2013). In regions with more data, the analysis is heavily influenced by the observations. In data-sparse regions, the forecast benefits from the information upstream (Park and Liang 2013). Most operational models use an analysis cycle, which is an intermittent data assimilation system (Kalnay 2003). Intermittent methods are technically convenient since observations are processed in small batches. Continuous methods use batches over long periods of time which is more realistic since the correction to the analysis is smoother in time (Kalnay 2003). Figure 2.1 explains the concept of data assimilation in a global and regional model. In regional models such as ARPS, lateral boundary conditions provided from a model forecast on a larger domain are necessary. Various data assimilation methods (i.e. the successive corrections method (SCM), optimal interpolation (OI), 3D-VAR, 4D-VAR, the Kalman Filter, and the EnKF exist, but each method combines the background and observations in a manner that minimizes the error in the analysis in a least-squares sense.

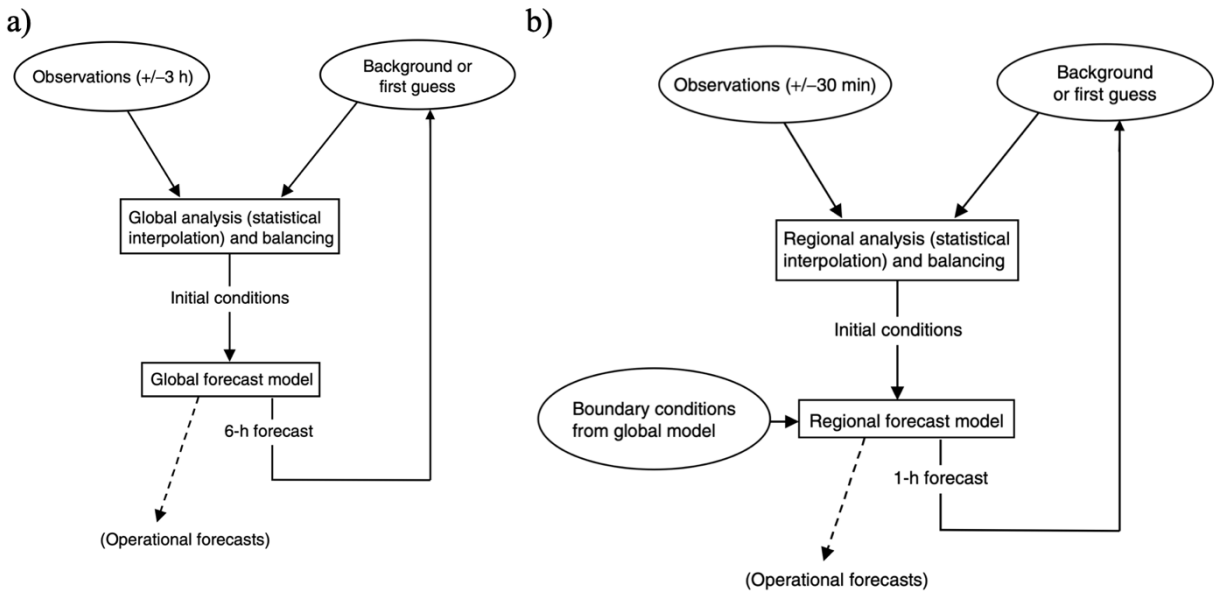

Figure 2-1. Example for (a) a global 6-hour analysis cycle; (b) a regional analysis cycle. The main difference is the timescales of assimilation in addition to the regional models requiring lateral boundary conditions. This image was adapted from Fig. 1.4.2 in Kalnay 2003.

2.2 Ensemble numerical weather prediction

Data assimilation creates a base state that can be perturbed to generate different initial conditions among ensemble members. Ensemble forecasting involves multiple forecasts for the same model in which the initial conditions are perturbed in slightly different ways across all ensemble members (Evensen 2009). Although the use of ensemble forecasting was originally implemented to improve the forecast skill of long-term forecasts, ensemble forecasting has become popular for high-resolution short-term NWP due to the increased lead time and accuracy of tornado warnings (e.g., Snook et al. 2012, 2019). Ensemble forecasts display possible scenarios of storm evolution and movement as well as mesocyclone or tornado potential (Snook et al. 2019).

Storm-scale (i.e. grid spacings on the order of a few km or less) prediction has become computationally tractable, but the explicit prediction of tornadoes is still not feasible. However,

storm-scale circulations (i.e. mesocyclones) can still be resolved and provide information regarding tornado probabilities (Skinner et al. 2016). Studies have successfully used the EnKF to model convective storms (e.g., Snyder and Zhang 2003; Dowell et al. 2004; Aksoy et al. 2010; Jung et al. 2012; Snook et al. 2012; Tanamachi et al. 2013; Dawson et al. 2012, 2013). These studies demonstrate the necessity for using ensemble forecasts and data assimilation in short-range convective scale NWP due to the intermittent nature, decreased spatial and temporal scale, decreased data coverage, and large forecast sensitivities of convective storms (Stensrud et al. 2009).

2.3 The ensemble Kalman filter (EnKF)

The so-called "extended" Kalman filter is a method of data assimilation which utilizes the method of maximum likelihood estimation using all available information to minimize the errors (Evensen 2009). Even with a modest representation of the first guess of the state of the atmosphere, after some time the extended Kalman filter will provide the greatest linear unbiased estimate of the atmospheric state and the associated error covariance (Kalnay 2003). Therefore, the extended Kalman filtering is often referred to as the "gold standard" of data assimilation (Evensen 2009). Unfortunately, since the extended Kalman filter uses the full error covariance matrix, it is intractably large for all but the simplest meteorological applications and computationally expensive. The EnKF reduces the computational demand drastically by sampling the error covariance matrix using a relatively small ensemble of forecasts (Evensen 1994).

The EnKF has become increasingly popular in the meteorological community (e.g., Snyder and Zhang 2003; Dowell et al. 2004; Aksoy et al. 2010; Jung et al. 2012; Snook et al. 2012; Tanamachi et al. 2013; Dawson et al. 2012, 2013) due to the affordable computational requirements, the simple conceptual formulation, and the relative ease of implementation (Evensen

2009). Radar observations, upper-air soundings, and surface observations have been assimilated via the EnKF in convective scale NWP models (e.g., Lilly 1990; Sun 2005; Stensrud et al. 2009; Snook et al. 2012; Tanamachi et al. 2013; Dawson et al. 2013). One major advantage the EnKF has over 3D-VAR is it produces meaningful flow-dependent covariances between the model state variables and observations (Snook et al. 2012). This results in an analysis mean (ensemble mean) as well as an uncertainty estimate (ensemble spread) (Dowell et al. 2011). The ensemble mean theoretically is the best state estimate of the true state of the atmosphere and the spread of the ensembles around the mean is a good estimate of the uncertainty present in the ensemble mean (Snook et al. 2012). This assumes the ensemble envelope contains the true state and is not underdispersed. A key benefit of the EnKF is the evolving (i.e. flow-dependent) covariances between observations and the model state allow for statistically robust estimates of the model state variables, most of which are unobserved (Snook et al. 2012). The linearization of the evolution of the forecast error covariance is not necessary (Kalnay 2003). The correlations are better estimated when more ensemble members are present and the root-mean-square error of the analysis decreases (Houtekamer and Mitchell 1998).

The EnKF is suitable for radar data assimilation due to the ability to handle forward observation operators used to derive radar reflectivity (Z) and other fields from the model state (Jung et al. 2008a,b). The assimilation of Z yields analyses of the thermodynamic and microphysical fields that are more consistent with observations (e.g., Lily 1990; Sun 2005; Stensrud et al. 2009; Snook et al. 2012). Additionally, assimilating radar data into convective scale NWP models is essential in reproducing various storm-scale convective features since radar is the only platform that reliably gives information about the structure and dynamics on the time and space scales relevant to convective evolution (e.g., Dawson and Xue 2006; Snook et al. 2012; Xue

et al. 2014). The extent of the radar data coverage is an important aspect of radar data assimilation. To best model an environment, assimilating more than one WSR-88D may be required owing to decreasing skill due to the model error growth no longer being controlled once a storm moves out of the radar coverage network (Xue et al. 2005).

2.4 The Advanced Regional Prediction System (ARPS)

Regional NWP models, such as ARPS, have been developed to resolve smaller-scale weather phenomena (like convective storms) that cannot be explicitly represented on coarser grids. The use of a larger regional, hemispheric, or global model is necessary in regional models like ARPS to specify the lateral boundary conditions (Kalnay 2003). ARPS was developed by the Center for Analysis and Prediction of Storms (CAPS) at OU (Johnson et al. 1994) and designed to serve as a tool for research regarding the prediction of convective storms. ARPS is a compressible and non-hydrostatic model useful for mesoscale to convective scale studies over a fixed domain (Johnson et al. 1994). The three-dimensional governing equations were transformed from Cartesian to curvilinear to account for terrain and stretched grids (Johnson et al. 1994). For a full description of ARPS, please reference Xue et al. (2000, 2001, 2003).

Like most NWP models, ARPS consists primarily of two steps: an initialization step and an iteration step. The initialization step creates arrays containing the initial gridded model state after reading the data, whereas the iteration portion advances the prognostic equations for the state variables forward in discrete time steps (Johnson et al. 1994). Several studies have successfully used ARPS for the types of problems investigated in this study (e.g., Dawson and Xue 2006; Schenkman et al. 2011, 2012; Xue et al. 2014; Dawson et al. 2015). ARPS is beneficial in many studies since information can be extracted about storm environments that is not possible via observations alone. A full description of how ARPS was configured for is found in the section 5.1.

2.5 Drop size distributions (DSDs)

Observed DSDs are approximated via analytical and parametric methods to help reduce the degrees of freedom. Marshall and Palmer (1948) originally proposed that rain DSDs can be expressed by the exponential distribution via the N_0 (intercept) and Λ (slope) parameters. DSDs have been observed as exponential distributions over long sampling periods; however, for shorter sampling periods the number of small and large drops tend to be overestimated by the exponential distribution (Vivekanandan et al. 2004).

The standard three-parameter gamma distribution (Eq. 1) displayed improvements from the exponential distribution in the observed and estimated rain rates in Ulbrich and Atlas (1984). There are three parameters present in the gamma distribution: shape (μ, unitless), slope (Λ, mm^{-1}), and intercept (N_0 $mm^{-1-\mu}$ m^{-3}). The shape parameter can be positive or negative. $N(D)$ (mm^{-1} m^{-3}) is the drop size distribution as a function of the sphere-equivalent volume diameter (D). The three parameters of the gamma distribution help to better describe the natural variations of the DSD shape (Ulbrich 1983). The shape of the DSD is determined by μ. When μ is positive (negative), the shape of the DSD on an $ln[N(D)]$ versus D is concave up (down). However, when $\mu = 0$, the exponential distribution is revealed as a special case (Fig. 2.2). The gamma function has been observed to perform well in both observational and numerical studies (Ulbrich 1983).

Many methods exist to estimate parameters of the gamma or exponential DSD that best fit observed DSDs from disdrometers. Numerous studies have used disdrometers to observe rain drop sizes (e.g., Atlas and Ulbrich 1977; Ulbrich 1985; Tokay and Short 1996). Tokay et al. (2013) describe three commonly used disdrometers: 1) laser optical disdrometers such as the OTT PARticle Size and VELocity (Parsivel^2) disdrometer; 2) the 2-dimensional video disdrometer (2DVD); and 3) the Joss-Waldvogel Disdrometer (JWT). These disdrometers measure the DSD by a different method. The Parsivel^2 disdrometer, which is used in this study, measures the size

and fall speed of particles as they fall through a sheet of laser light (Löffler-Mang and Joss 2000). The 2DVD uses two orthogonal high-speed cameras whereas the JWD uses the force of the drop on a sensor to measure the drop. Tokay et al. (2013) discusses each of these disdrometers in detail.

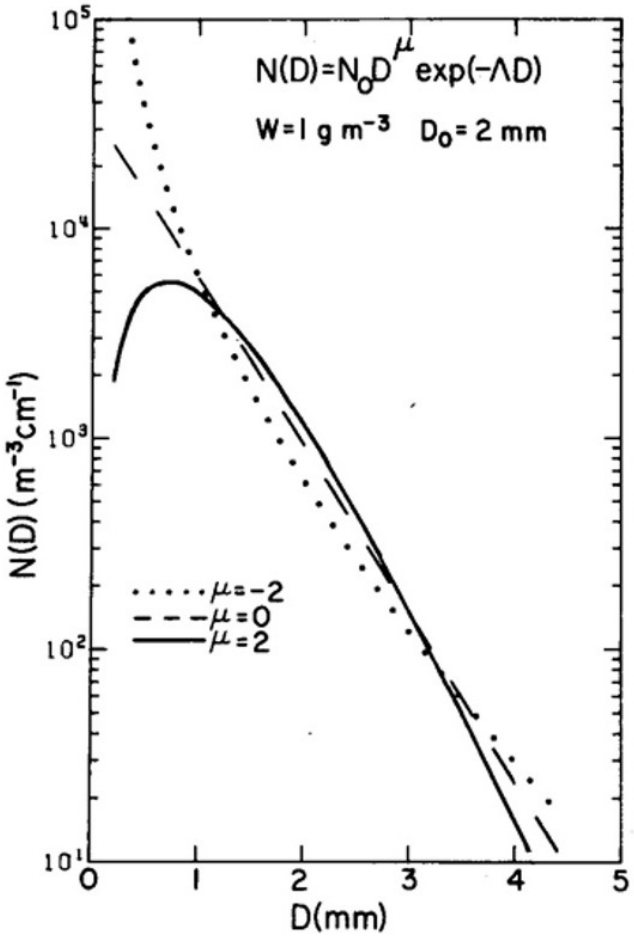

Figure 2-2. A diagram of gamma raindrop size distributions for μ = -2, 0, and 2 with a liquid water content (W) = 1 g m^{-3} and the median drop diameter (D_0) = 2 mm. This image was adapted from Fig. 2 in Ulbrich et al. (1983).

2.5.1 Estimating DSD parameters

To estimate the gamma DSD parameters from disdrometer observations, a method needs to be selected. Various estimation methods exist, including the method of moments (Ulbrich 1993; Tokay and Short 1996), the truncated method of moments (Ulbrich and Atlas 1998), maximum

likelihood, and L-moment estimators (Hosking 1992). The most common methods are the method of moments and the truncated method of moments. Errors arise from considering all drop sizes in the parameter estimation in the method of moments since the moment integral extends from 0 to ∞ (Ulbrich and Atlas 1998). However, considering all mathematically possible drop sizes does not reflect reality since drop sizes are only ever observed over a finite interval D_{min} (mm) to D_{Max} (mm). The truncated method of moments (TMM) was introduced to reduce the errors when considering all drop sizes by integrating only over the observed drop size range (Vivekanandan et al. 2004; Cao et al. 2008). Fitting a gamma distribution to observed DSDs allows for a more direct comparison with model-predicted gamma DSDs.

2.6 Microphysics schemes

Hydrometeors, such as rain drops, have DSDs that are heavily influenced by microphysical processes parameterized by the model's BMP scheme (Rosenfeld and Ulbrich 2003). Collision, coalescence, and the breakup of raindrops need to be adequately represented in the BMP scheme of the model to best represent observed DSDs (Rosenfeld and Ulbrich 2003). Aspects of storm behavior (i.e. cold pool size and strength) are influenced by the underlying BMP scheme (e.g., Gilmore et al. 2004; van den Heever and Cotton 2004; Snook and Xue 2008; Dawson et al. 2010, 2015). BMPs often use a gamma function to characterize the hydrometeor size distribution. Single-moment BMPs are efficient computationally since only one moment is predicted (usually the mass content which is proportional to the third moment of the hydrometeor distribution function while two parameters are diagnosed or fixed), but several weaknesses contribute to significant errors on the storm scale (i.e., not representing size sorting of hydrometeors) (e.g., Dawson et al. 2010, 2014; Milbrandt and McTaggart-Cowan 2010). Double-moment schemes frequently predict the mass content and total number concentration so that λ and N_0 are independently prognosed while α

remains fixed or diagnosed as a function of them (Milbrandt and Yau 2005a, 2005b). Holding α constant can result in unrealistically large drops at the tail of the distribution (Milbrandt and Yau 2005a, 2005b). Increasing the predicted moments in the BMPs from one (single-moment) to three (triple-moment) allows for the three free parameters of the gamma size distribution to vary independently (Milbrandt and Yau 2005a, 2005b; Dawson et al. 2010).

Results from an idealized supercell simulation reveal the benefits of triple-moment microphysics (Dawson et al. 2010, 2014). Evaporation and size sorting processes are also improved in triple-moment schemes, which lead to DSDs which control the cold bias frequently found in single- or double-moment schemes (Dawson et al. 2010, 2014). Basic polarimetric features (mainly differential reflectivity (Z_{DR})) are reasonably reproduced using a triple-moment scheme when the bulk density of the rimed ice category is predicted (Dawson et al. 2014). Therefore, the NSSL-TM microphysics scheme is a natural choice for this study.

2.6.1 NSSL Triple-Moment microphysics scheme

The NSSL-TM microphysics scheme described in Dawson et al. (2014) is an updated version of the multimoment microphysics scheme used by Mansell et al. (2010), itself based on an earlier microphysics scheme developed by Ziegler (1985). The full NSSL-TM scheme has numerous options to control different microphysical processes including the number of moments predicted (Dawson et al. 2014). Additionally, the number of rimed-ice categories can be changed. There will always be a graupel/frozen drops category that includes graupel, frozen drops, or small hail depending on the size, density, and fall-speed assumptions, but an additional "large hail" category can also be enabled (Dawson et al. 2014). The NSSL-TM scheme also has an option to enable processes that control the variation of bulk densities of graupel/frozen drops and hail. Ultimately, the graupel/frozen drops category can represent several particle types including low-

density graupel, frozen drops, or small hail, but based on the dominating characteristics are referred to as either graupel or frozen drops (Dawson et al. 2014). The large hail category accounts for larger high density graupel/hail resulting from wet growth (Dawson et al. 2014). An important aspect of the NSSL-TM scheme is that up to three moments of the gamma size distribution (mixing ratio, number concentration, and Z) are predicted for rain, graupel/frozen drops, and hail (Dawson et al. 2014). This leads to a solution that represents size sorting and other microphysical processes (collision, coalescence, drop breakup, rain evaporation, and melting of hail) more realistically. For example, three prognostic moments are required to allow the distribution to narrow and size sorting to be accurately modeled (Milbrandt and Yao 2005). Using simple single-column simulations, Millbrandt and Yao (2005) showed the triple-moment scheme was closest to the Lagrangian analytical solution and a substantial improvement over the single- and double-moment schemes (Fig 2.3). Prognostic CCN, which is of particular relevance for this study, can be enabled in the NSSL-TM scheme. A diagram of the different hydrometeor categories and which quantities are predicted is found in Table 2.1.

Based on Milbrandt and Yau (2005a,b), the zeroth, third, and sixth moments are predicted. The closure scheme of the sixth moment rate equations follows that of Milbrandt and Yau (2005b). The gamma size distribution can be written as (Milbrandt and Yau 2005b):

$$N_x(D) = N_{Tx} \frac{3\mu_x}{\Gamma(\alpha_x+1)} \lambda_x^{(\alpha_x+1)3\mu x} D_x^{(\alpha_x+1)3\mu x-1} x \exp\left[-(\lambda_x D_x)^{3\mu x-1}\right] \quad (2),$$

where N_{Tx} is the total particle number concentration, α is the first shape parameter, μ is the second shape parameter (which is fixed at some value, reducing to a three-parameter gamma distribution), and λ_x is the slope parameter, and D_x is the sphere-equivalent volume diameter. The slope parameter can be defined by the zeroth and third moments of the distribution:

$$\lambda_x = \left[\frac{\pi(\alpha_x + 1)}{6v_0}\right]^{1/3} \quad (3)\ when\ \mu_x = 1\ ,$$

$$\lambda_x = \left[\frac{\pi(\alpha_x + 3)(\alpha_x + 2)(\alpha_x + 1)}{6v_0}\right]^{1/3} \quad (4)\ when\ \mu_x = 1/3\ ,$$

when the mean particle volume (v_0) is defined as:

$$v_0 = \frac{p_a q_x}{p_x N_{Tx}} \quad (5)$$

Part of the update described by Dawson et al. (2014) was the addition of warm rain equations by Cohard and Pinty (2000). This allows for rain to use the original gamma volume ($\mu_r = 1$) or the gamma of diameter ($\mu_r = 1/3$), which is used in this study. Additional details regarding the changes to the Mansell et al. (2010) scheme are highlighted in the Appendix of Dawson et al. (2014).

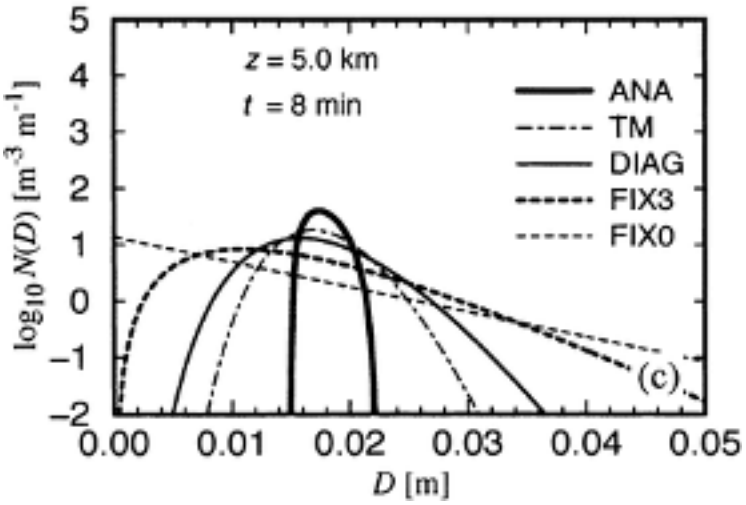

Figure 2-3. Particle size distributions from a Lagrangian analytical model (ANA, solid), triple-moment (TM, dot-dashed), diagnosed double-moment (DIAG, thick solid), double-moment with α_h =3 (FIX3, thick dashed), and double-moment with α_h =0 (FIX0, dotted). This image was adapted from Fig. 8 in Milbrandt and Yao (2005).

Table 2-1. Hydrometeor categories and quantities predicted in the NSSL-TM microphysics scheme.

	Mixing Ratio (q_x)	Number Concentration (n_x)	Reflectivity (z_x)	Bulk Volume (v_x)
Droplets	X	X		
Rain	X	X	X	
Cloud Ice	X	X		
Snow	X	X		
Graupel/Frozen Drops	X	X	X	X
Hail	X	X	X	X
CCN		X		

2.7 Cloud condensation nuclei (CCN)

Certain microphysical properties (i.e. changes in the cloud and rain drop sizes and numbers, and cloud and ice water paths) are more sensitive to changes in CCN concentration than changes in CAPE, resulting in notable differences in storm evolution and precipitation (Storer et al. 2010). Therefore, it is essential to understand the effects of any differences in CCN concentration across the VORTEX-SE domain compared to the central Plains, owing to geographical proximity to maritime vs. interior continental sources and the influence of metropolitan and industrial areas.

2.7.1 Geographic variations of CCN concentration

Yue et al. (2019) used satellites to observe the CCN concentration. The results are what are expected: minima in CCN values over the open ocean with a gradual increase as the distance inland increases, and localized higher values in metropolitan and industrial areas due to anthropogenic emissions (Yue et al. 2019). However, the majority of higher continental CCN concentrations are from natural sources as opposed to anthropogenic sources (Rauber 2003).

Spracklen et al. (2011) incorporated extensive CCN concentration observations into simulations of global CCN concentration. Simulations were conducted without (Fig. 1.1a) and with (Fig. 1.1b) carbonaceous combustion aerosol acting as CCN. These simulations synthesized observations from 55 different studies of CCN observations across the world and interpolated where data was absent (Spracklen et al. 2011). For a full list of the studies included, please reference Table 1 in Spracklen et al (2011). Simulated CCN concentrations are lower in the central Plains than the SE-US in both simulations. These results are plausible given the SE-US has more metropolitan and industrial areas than the central Plains (Rauber 2003; Spracklen et al. 2011).

Rauber (2003) separates CCN concentration values into three separate categories: 1) warm maritime (50-300 cm^{-3}); 2) mid-latitude rural (200-500 cm^{-3}); and 3) urban (700-3,000 cm^{-3}). While locally higher CCN concentrations are possible over land, Jones et al. (2018) found that reducing the CCN concentration in the NSSL scheme from 2,000 cm^{-3} to 1,000 cm^{-3} reduced the upper-tropospheric cloud areal coverage bias as compared with satellite observations. Therefore, a widely used continental CCN concentration value in the modeling of convective storms in the central Plains is 1,000 cm^{-3} (Jones et al. 2018). The CCN concentration in the SE-US is not a fixed value and there remains uncertainty of the ranges of CCN values in this region due to the proximity to the Gulf of Mexico so CCN experiments ranging from 100-2,000 CCN cm^{-3} are conducted.

2.7.2 CCN concentration influence on microphysics

In the simulations of Storer et al. (2010), the largest differences in microphysical properties existed between those with different CCN concentrations (Storer et al. 2010). The relative contributions of warm and cold rain processes are sensitive to CCN concentration. In higher CCN concentration environments, cloud droplets are more abundant and smaller; hence warm rain processes such as collision and coalescence are less efficient and cold rain processes dominate

(e.g., Squires 1958; Squires and Twomey 1966; Warner and Twomey 1967; Warner 1968; Rosenfeld 1999; Rosenfeld and Ulbrich 2003; Andreae et al. 2004; Tao et al. 2012). An increase in the CCN concentration also results in more cloud drops which provides more cloud water for riming and enhanced freezing (Cheng et al. 2010). The resulting DSDs have a greater proportion of larger drops from the melting of graupel, hail, and snow. Additionally, polluted clouds have a higher availability of ice water and cloud water content leading to larger precipitating hydrometeors both in the cloud and at the surface (Storer et al. 2010). In contrast, warm rain processes dominate in lower CCN concentration environments resulting in DSDs containing relatively smaller drops (e.g., Rosenfeld and Woodley 2000; Andreae et al. 2004). Tao et al. (2012) discusses the influence of the different processes in greater detail. In previous studies, higher CCN concentration simulations have been observed to delay autoconversion and the onset of precipitation (Saleeby et al. 2010). This is important to remember when doing direct comparisons of model output and observations. These differences in DSDs impact cold pool and downdraft size and strength, which in turn influence tornado potential, resulting in the motivation for this study.

2.7.3 CCN concentration influence on dynamics

The CCN concentration can impact the dynamics of convective storms (Storer et al. 2010). An increase in updraft strength should be seen in higher CCN concentration environments because of the activation and freezing of more cloud droplets resulting in an increased release of latent heat of condensation and freezing (e.g., Khain et al. 2005; van den Heever and Cotton 2007; Tao et al. 2012), but Storer et al. (2010) did not find this relationship in their simulation study. Higher CCN concentration environments have less total surface precipitation and fewer larger rain drops or larger hail stones compared to lower CCN concentration environments (Storer et al. 2010; Tao et al. 2012). Larger precipitating hydrometeors do not evaporate as efficiently due to higher fall

speeds and decreased surface area (Storer et al. 2010). Therefore, the reduced surface precipitation and differences in hydrometeor size reduce the evaporative cooling at the surface and lead to a weaker and warmer cold pool in higher CCN concentration environments (Storer et al. 2010). Kalina et al. (2014) found similar results for low relative humidity environments but noted this trend is not present for all thermodynamic environments. Tao et al. (2012) found low tropospheric environmental cooling to be essential to the relationship between CCN concentration and surface precipitation in determining if higher CCN concentrations reduce or enhance surface precipitation.

Differences in cold pool size and strength can lead to various dynamic feedbacks. The weaker and less spatially expansive cold pools associated with higher CCN concentrations provide less forcing for new convection (Storer et al. 2010). This results in less convective coverage and total surface precipitation compared to lower CCN concentrations (Storer et al. 2010; Kalina et al. 2014). The microphysical and dynamical properties impacted by changing the CCN concentration is an active area of research and needs to continue to be evaluated (e.g., Storer et al. 2010; Tao et al. 2012; Kalina et al. 2014).

Examining the influence of CCN concentration on DSDs of convective storms in the SE-US will provide a basis for which ranges of CCN concentrations represent the SE-US, which in turn can be used in future numerical models to improve the prediction of convective storms. Therefore, the goal of this study is to investigate the sensitivity of CCN concentration on DSDs in the SE-US by comparing model output DSDs with varying CCN concentrations to observed DSDs from portable disdrometer-equipped probes in a tornadic QLCS on 30 April 2017 during VORTEX-SE.

CHAPTER 3. CASE OVERVIEW

3.1 30 April 2017 case overview

The 30 April 2017 IOP 4C provided the unique opportunity to collect data on a well-developed QLCS that produced more than two dozen tornadoes across Mississippi during the morning hours of 30 April 2017 before approaching the VORTEX-SE domain (Fig. 3.1). This VORTEX-SE case was the last Intensive Operating Period (IOP) of the 2017 field season and does not fit the standard cold season set up. However, a HSLC environment was still observed.

Initially, limited instability, a substantial capping inversion, and weak 0–6-km shear were present during the morning of 30 April 2017 over northern and central Alabama as evidenced by the 1200 UTC Birmingham, AL sounding (Fig. 3.2) and Storm Prediction Center (SPC) Mesoanalysis (Fig. 3.3a and Fig. 3.3b) (Hart et al. 2017). The environment slowly improved as winds aloft increased due to a jet rounding the base of the upper level low as it moved across the SE-US. The 100 kt jet slowly moved eastward throughout the day over the VORTEX-SE domain, which was associated with a 998 hPa low pressure system located in east-central Kansas. The VORTEX-SE domain was located in the warm sector of the cyclone, with southerly surface winds advecting warm, moist air across the SE-US. Surface dew points ahead of the QLCS surged from 16–20 C. Air temperatures increased to 24–27 C, increasing low-level lapse rates.

Clouds initially slowed the diurnal heating of the boundary layer, but the strong low-level jet allowed for sufficient equivalent potential temperature (θ_e) advection. Breaks in the clouds provided additional support for CAPE to increase to 500–1,000 J kg^{-1} across western and northern Alabama, with slightly higher CAPE of 1,000–1,500 J kg^{-1} across central and eastern Alabama (Fig. 3.4a) (Hart et al. 2017). Determining if the atmosphere would recover and support severe weather across northern Alabama was an uncertainty NWS forecasters faced (NWS Storm

Prediction Center 2017). The marginal CAPE of 500–1,000 J kg^{-1} coupled with sufficient 0–6-km shear of 40–50 kt (Fig. 3.4b) and steepening lapse rates allowed the severe weather threat to continue across the VORTEX-SE domain. Most of the 0-6 km shear was confined to the lowest 3 km, resulting in strong low-level shear. The NWS SPC issued Tornado Watch #182 for northeastern Mississippi and western Alabama and eventually Tornado Watch #183 for eastern Alabama, central Tennessee, and northwest Georgia as the QLCS approached these areas (NWS Storm Prediction Center 2017). Embedded supercells, mesovortices, and damaging winds from the bowing segments were noted as the main threats (NWS Storm Prediction Center 2017).

As the QLCS approached the VORTEX-SE domain (Fig. 3.5), embedded mesovortices and an embedded mesocyclone formed, prompting a tornado warning south of the PIPS deployment locations (Fig. 3.6). The NWS in Huntsville, AL confirmed an EF-0 tornado east of Interstate 65 in Cullman County, AL and traveled northeast for 10 miles before dissipating near the Morgan County, AL line (NWS Huntsville, Alabama). This QLCS had a strong cold pool with perturbations of potential temperature (θ) of 5-8°C and θ_e of 9-12°C. Even with a strong cold pool, which has been shown to be unfavorable for tornadogenesis (Markowski et al. 2003; Hirth et al. 2008), a tornado was produced, leading to additional motivation for this study.

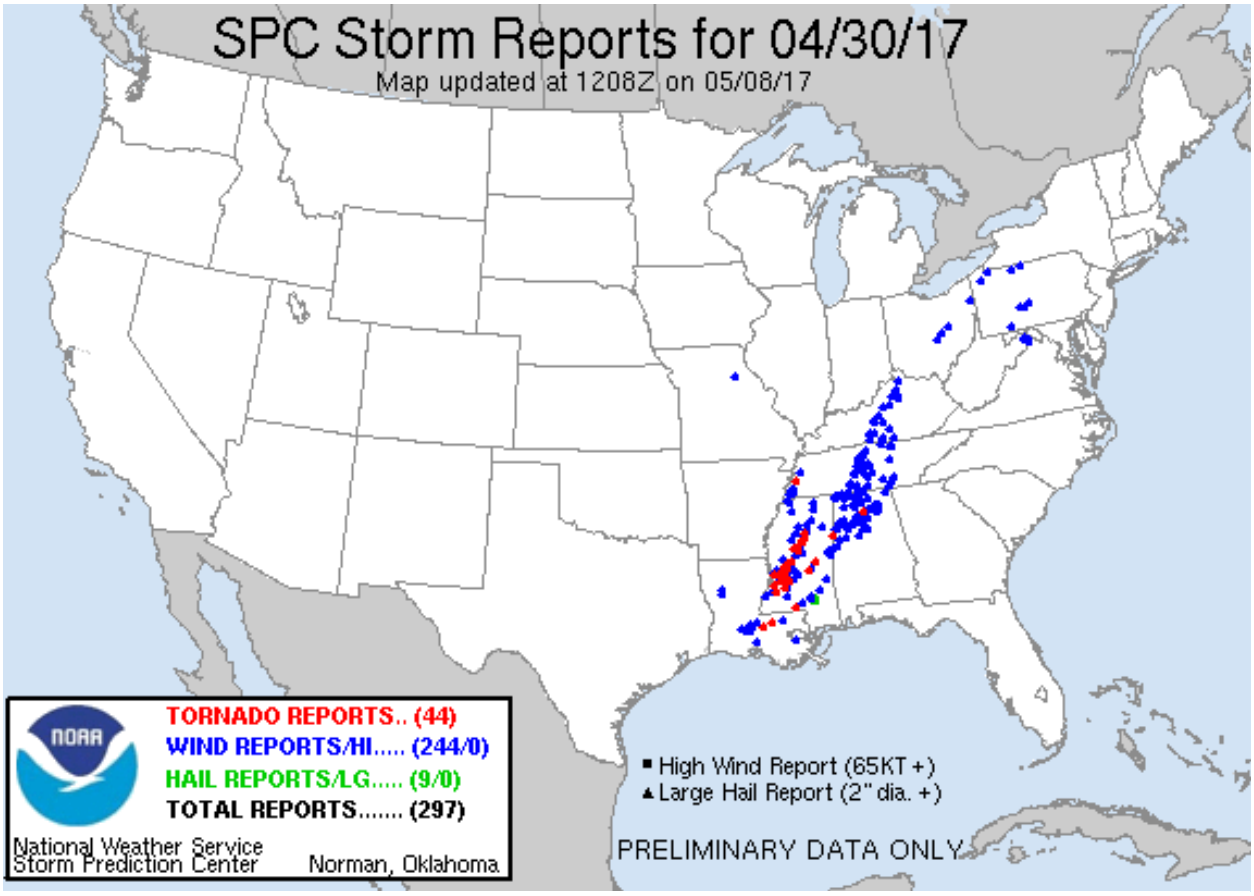

Figure 3-1. SPC storm reports from 30 April 2017 of confirmed tornadoes (red), wind damage (blue), and hail (green) (NWS Storm Prediction Center 2017).

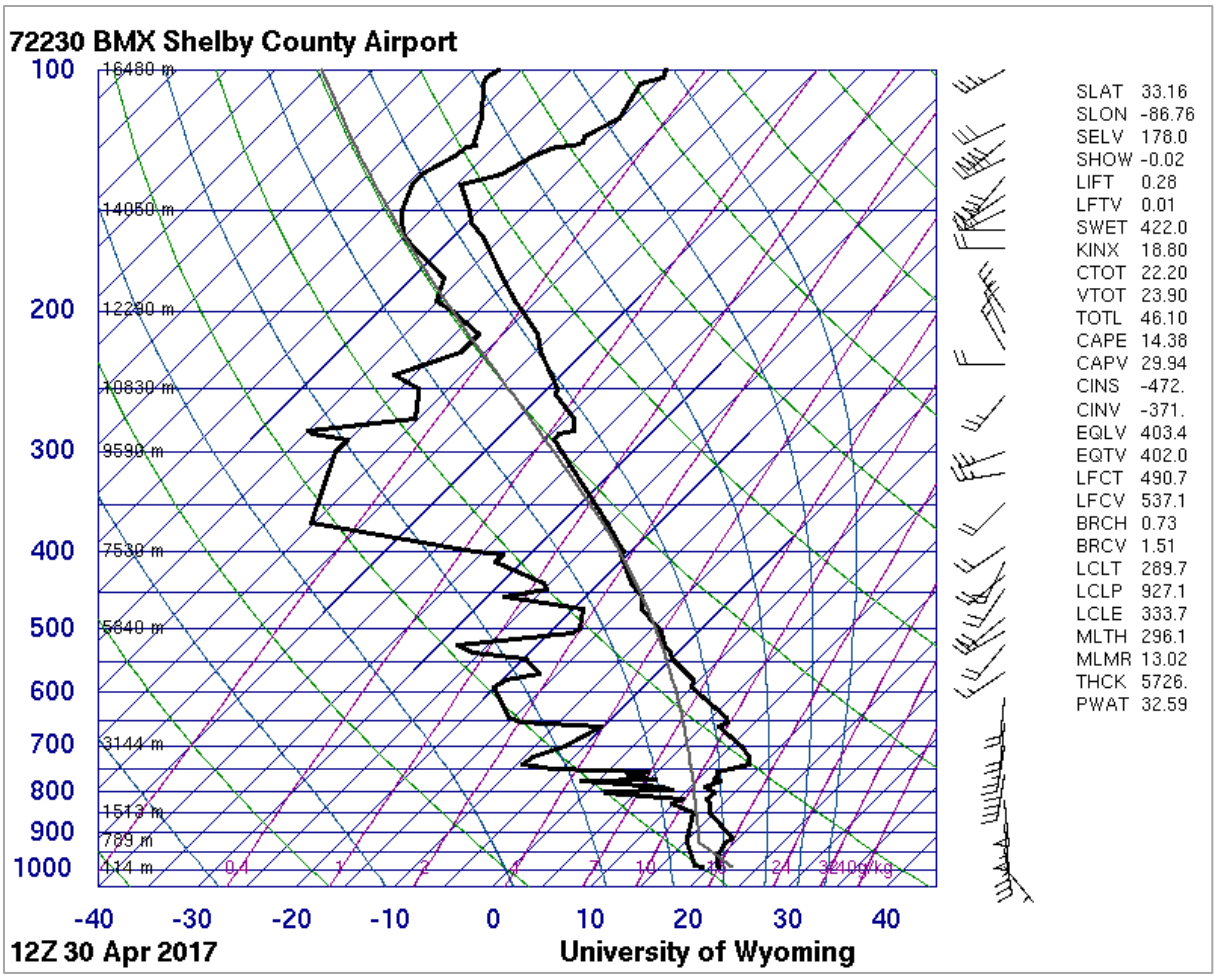

Figure 3-2. Upper-air sounding from KBMX (Birmingham, AL) at 1200 UTC 30 April 2017.

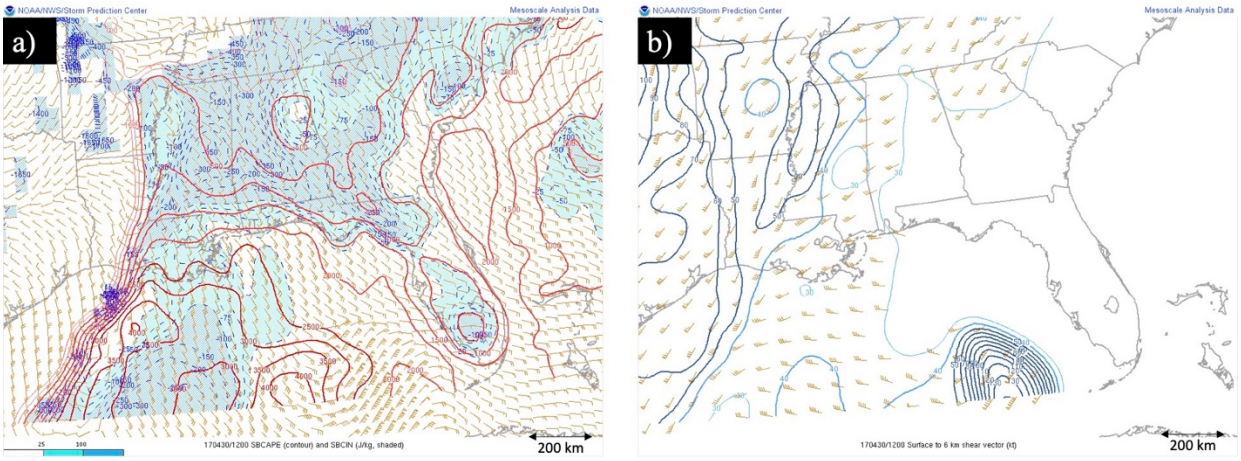

Figure 3-3. SPC Mesoanalysis valid at 1200 UTC 30 April 2017 showing: a) surface-based CAPE (red contours every 500 J kg^{-1}, with the first two contours being 100 J kg^{-1} and 250 J kg^{-1}) and surface-based convective inhibition (CIN, J kg^{-1}; shaded blue contours); and b) 0–6-km shear barbs (yellow barbs in kts) and isoshears (blue contours every 10 kt starting at 30 kt).

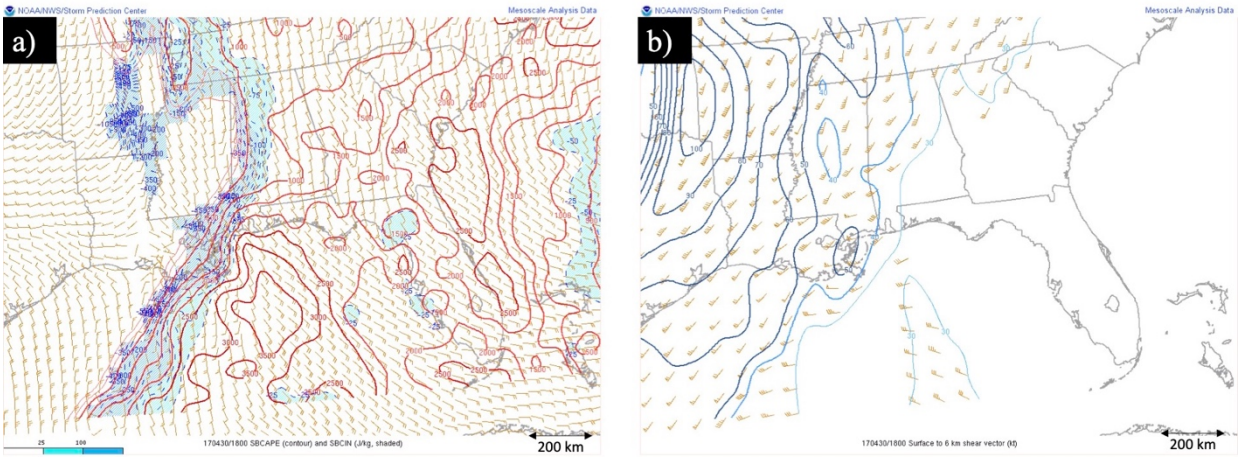

Figure 3-4. As in Fig. 3.2., but for 1800 UTC 30 April 2017.

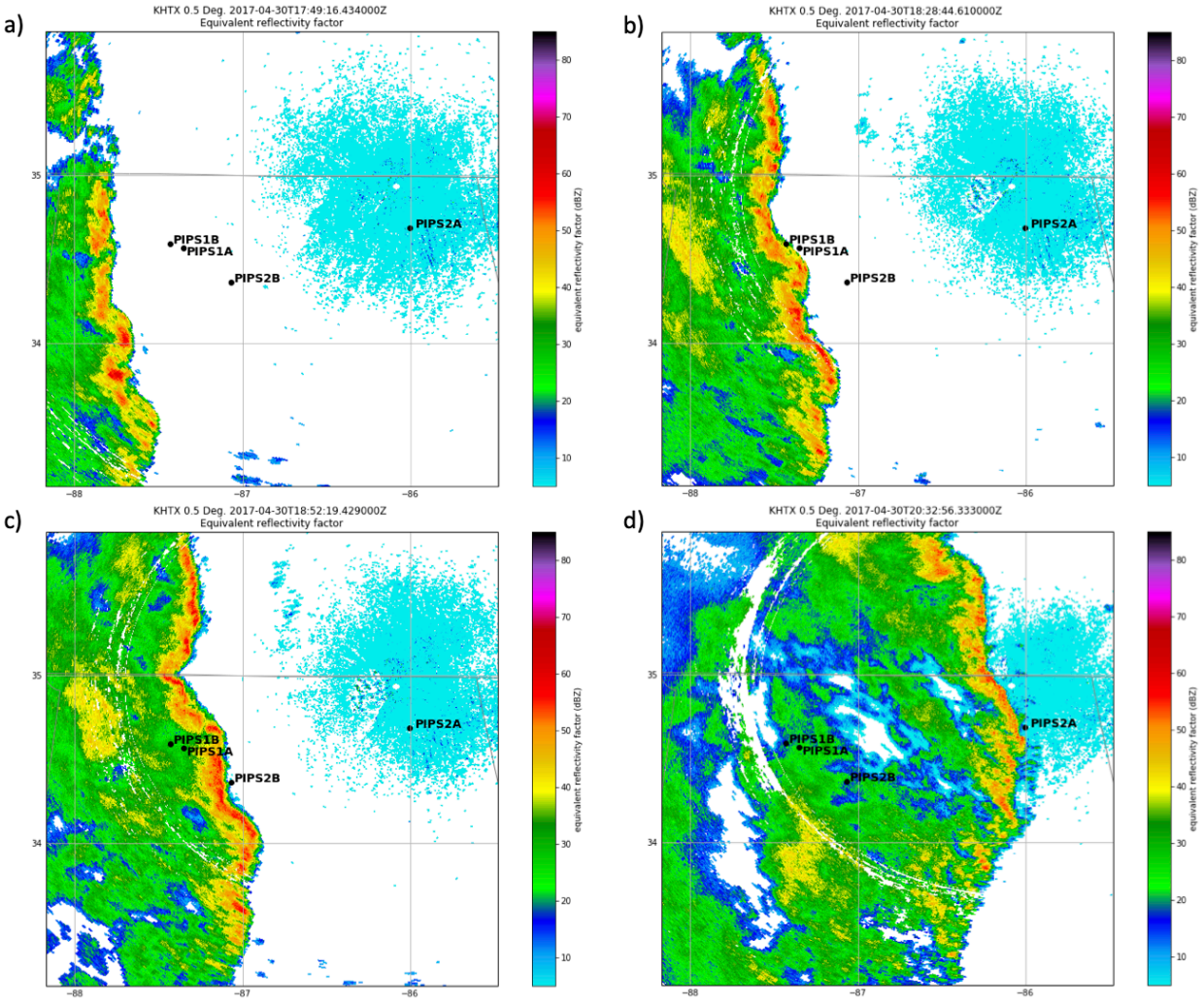

Figure 3-5. Base *Z* from the Huntsville, Alabama WSR-88D (KHTX) of the QLCS (a) entering the 1-km simulations grid, (b) approaching PIPS1A and PIPS1B, (c) approaching PIPS2B, and (d) weakening as it approaches PIPS2A.

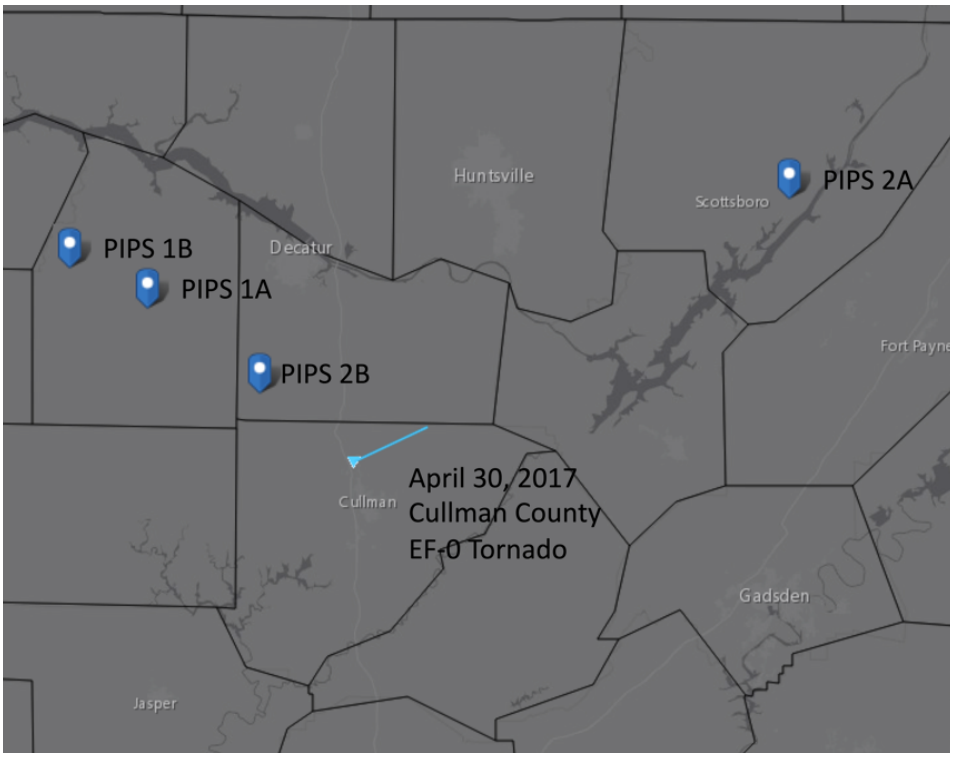

Figure 3-6. The touchdown location of the EF-0 tornado in Cullman County, Alabama (blue triangle) and the tornado track (blue line) in relation to the PIPS1A, PIPS1B, PIPS2A, and PIPS2B locations (Midwest Regional Climate Center 2021).

CHAPTER 4. DATA

4.1 Data collection

Both observational and model data are used in this study. The North American Mesoscale Model (NAM) provides the background and initial conditions for the outer-most ARPS grid. Observations from the PIPS are directly compared to model output from ARPS. Surface and radar observations were assimilated into ARPS via the EnKF method to analyze the evolution of the 30 April 2017 QLCS and its environment.

Climatological and geographic constraints were considered when planning the 2016 and 2017 VORTEX-SE field campaigns. Based on climatology, the southeastern U.S. sees a peak in tornado frequency during March and April, which is before the nationwide climatological average (Ashley 2007, 2008). A local maximum in tornado frequency is present over northern Alabama during this timeframe (NWS Storm Prediction Center 2020). Therefore, the VORTEX-SE field campaign was operated out of Huntsville, AL from March to May. Adding to the incentive to focus the campaign around Huntsville was the wide array of instruments already in place and owned by the University of Alabama-Huntsville. The VORTEX-SE domain during the 2016 and 2017 field campaigns was approximately within 100-200 km of Huntsville, AL. While this is a small domain when considering the SE-US as a whole, logistical constraints resulted in northern Alabama as the primary data collection site.

Numerous universities and partners participated in preparing the instruments for data collection, collecting the physical data, or aiding in forecasting potential IOPs. Collaborators include Texas Tech University, the University of Alabama-Huntsville, OU, Purdue University, the University of Massachusetts-Amherst, and the NSSL. These collaborators collected data from a wide range of instruments including portable weather stations, radiosondes, radar, and

disdrometers, among others. The portable weather stations and disdrometers (specifically the PIPS, co-owned by the NSSL, OU, and Purdue University) are most relevant to this study and will be described in section 4.2. Local NWS offices (e.g. NWS Birmingham, AL and NWS Huntsville, AL) also assisted in data collection by launching special radiosondes on days of IOPs.

Because the field campaign spanned several months, it was not feasible for all collaborators to continuously be in the domain. Rather, collaborators would converge on the VORTEX-SE domain for IOPs. Each year during VORTEX-SE, the synoptic weather pattern was analyzed by different program leaders and student forecasters in a daily briefing to highlight, with as much lead time as possible, potential IOPs. Typically, 3-5 days of notice was given for potential IOPs with a final decision coming from program leaders 1-3 days before the IOP. IOPs were identified by numbers (occasionally followed by letters for contiguous cases). The IOP this study will focus on is VORTEX-SE 2017 IOP4C on 30 April 2017.

4.2 Observational data

4.2.1 Disdrometer data

The observations used in this study were collected from four PIPS deployed during VORTEX-SE IOP4C on 30 April 2017: PIPS1A, PIPS1B, PIPS2A, and PIPS2B. The observed disdrometer data were retrieved from the VORTEX-SE Earth Observing Laboratory (EOL) website (https://data.eol.ucar.edu/dataset/541.029, Earth Observing Laboratory 2020). PIPS1A, PIPS1B, and PIPS2B were all deployed ahead of the incoming QLCS and retrieved after the QLCS passed. PIPS2A was collocated with the University of Massachusetts Frequency-Modulated Continuous-Wave (FMCW) radar for the duration of the 2017 VORTEX-SE field campaign at the Scottsboro, AL municipal airport. PIPS1A and PIPS1B were set up in central Lawrence County,

AL whereas PIPS2B was deployed in southwestern Morgan County, AL. A map of the PIPS deployment locations is found in Figure 3.6. The PIPS were deployed at the aforementioned locations during the event from: 1748-1956 UTC (PIPS1A), 1731-2007 UTC (PIPS1B), and 1846-1929 UTC (PIPS2B).

The PIPS (Fig. 4.1) include instrumentation to measure temperature (T), relative humidity, pressure (p), and wind (speed and direction). The PIPS are also equipped with an OTT Parsivel^2 laser disdrometer (Löffler-Mang and Joss 2000; Tokay et al. 2014). This disdrometer was selected for its relative low cost and easy transportation, making it ideal for a field campaign (Löffler-Mang and Joss 2000; Friedrich et al. 2013). A horizontal sheet of infrared light measures particle diameters ranging from 0.25-25 mm and velocities up to 20 m s^{-1} (Fig. 4.1). A noteworthy assumption is that only one particle goes through the laser beam at any given time, an assumption which may be violated for sufficiently high rain rates (Raupach and Berne 2015). When the particle passes through the laser beam, a reduction in voltage occurs that is measured by the instrument before being inverted, amplified, and smoothed. The duration of the reduction of the signal and its maximum amplitude quantify the velocity and diameter of the particle, respectively. The particles with diameters in the two bins below 0.25 mm are discarded because of the inherently low signal to noise ratio. The remaining particles are sorted into 32 non-equidistant bins for size and velocity and assigned to the diameter and velocity that match the bin center. The duration of recording for each DSD is 10 s. As part of the post-processing, these 10-s DSDs were aggregated into contiguous 60-s DSDs to increase the sample size. This is a tradeoff between improved statistics from better samples for a longer interval and avoiding smearing out of the DSD if the time interval becomes too long and the DSD varies too much during the integration interval.

While there are many benefits of the Parsivel^2 disdrometer, there are noteworthy limitations. Multiple studies have observed measurement errors for small and large drop concentrations (e.g., Tokay et al. 2013; Park et al. 2017). Due to instrument resolution and reduced sensitivity, retrieving accurate small drop number concentrations is difficult for Parsivel^2 disdrometers (Thurai et al. 2014). Thurai et al. (2011) found that during periods of heavy rainfall ($R > 20$ mm hr^{-1}), the Parsivel^2 disdrometer may misclassify several small drops passing through the laser beam simultaneously as one larger drop, leading to the overestimation of large drop concentrations. However, when $R < 20$ mm hr^{-1}, the Parsivel^2 disdrometer performs comparably to higher-resolution 2D video disdrometers (Thurai et al. 2011). Though not a major concern for this study because hail was minimal, Thurai et al. (2011) found the largest disagreement between Parsivel^2 and 2D video disdrometer data were larger magnitudes of the gamma DSD parameters when hail and graupel were present.

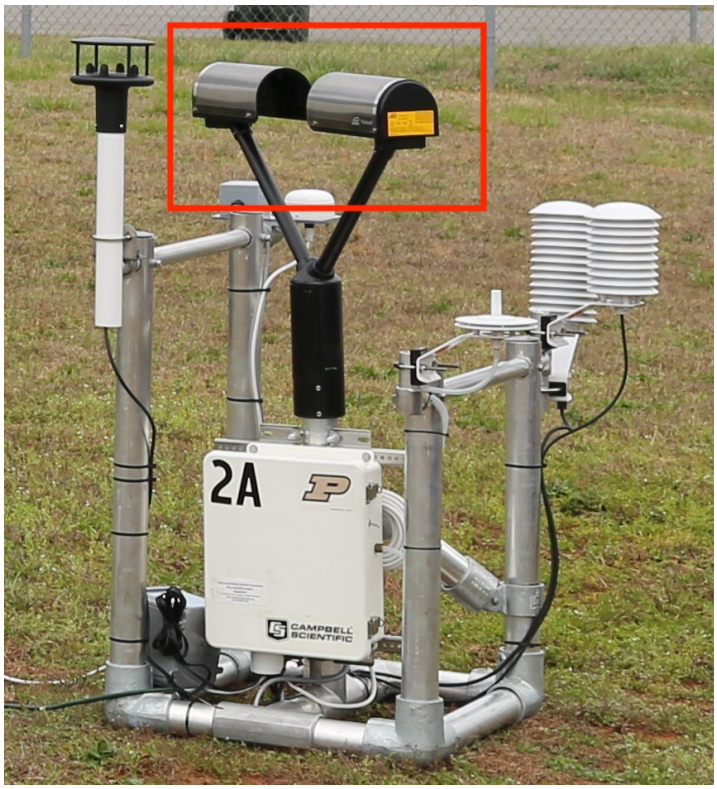

Figure 4-1. PIPS2A in a field with the Parsivel^2 disdrometer outlined in red (image courtesy of Daniel Dawson).

4.2.2 Disdrometer data quality control

The raw disdrometer data from the PIPS must be processed through several quality control steps to remove dubious observations, improve gamma DSD fits, and allow for fair comparison with the simulated DSDs. The stationary disdrometer data filtering method used on the Verification of the Origin of Rotation in Tornadoes Experiment-2 (VORTEX-2) disdrometer observations by Friedrich et al. (2013) is closely followed in this study. First, a hydrometeor classification scheme to differentiate between rain, hail and graupel is applied (Fig. 4.2). The hydrometeor classification scheme allows for the removal of data with a D greater than 8 mm, since rain drops typically have a diameter less than 8 mm owing to the onset of aerodynamic

breakup at larger sizes (Friedrich et al. 2013). Any remaining particles that fall into either the hail or graupel categories are removed. This leaves only particles categorized as rain remaining.

Strong winds, margin-falling drops, and the splashing of drops result in drops with unlikely fall speeds for the associated diameter (Friedrich et al. 2013). The measurement accuracy of the disdrometer during strong winds can be improved if the disdrometer is aligned perpendicular to the wind direction (Friedrich et al. 2013). Therefore, efforts were made to position the disdrometers perpendicular to the prevailing or expected wind direction at the onset of precipitation during VORTEX-SE. Strong winds (wind speed > 10 m s^{-1}) could still influence the quality of the disdrometer observations. The case of strong winds often results in large drops (D > 5 mm) having abnormally low fall speeds of less than 1 m s^{-1}. When this occurs, the associated data at that given time are removed from the dataset.

Raindrop terminal fall speeds as a function of drop diameter have been derived from empirical observations and theoretical calculations. The standard to which measurements and theoretical models are compared is the laboratory dataset of Gunn and Kinzer (1949) of the fall speed of water drops in still air. Thurai and Bringi (2005) performed an 80-m fall experiment with artificially generated drops up to 9.5 mm in D. The results agreed well with those of Gunn and Kinzer (1949) up to about 6 mm. Above 7 mm, Thurai and Bringi (2005) discovered a decreasing trend in fall speed owing to the increase in drag due to large drop distortion. The results of Gunn and Kinzer (1949) have been confirmed with general agreement using disdrometers that measure both fall speed and diameter (e.g., Friedrich 2013; Thurai et al. 2013).

Only drops that fall within ± 60% of the expected terminal fall velocity are passed through the quality control check. Margin fallers are identified as particles that have a fall velocity 60% greater than the observed value for rain or hail, whereas splashing drops are denoted as particles

with a fall velocity less than 60% of the expected (terminal) value and $D < 2$ mm (Friedrich et al. 2013). A margin faller is a particle that only partially passes through the beam, resulting in a small drop with a greater-than-expected (i.e., terminal) fall speed for that diameter. Splashing drops occur when drops hit a piece of equipment on the PIPS causing the drop to break-up into smaller drops before moving through the disdrometer at lower-than-expected fall speeds. An example of the raw PIPS data for the duration of the deployment is found in Fig. 4.3a for PIPS1A and the quality-controlled data in Fig 4.3b for the same time window.

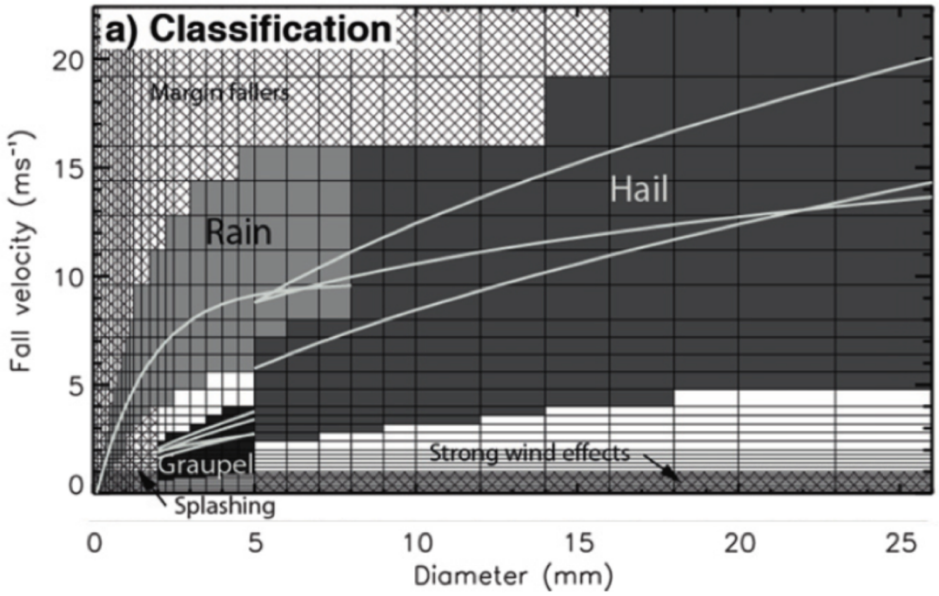

Figure 4-2. A schematic of the hydrometeor classification scheme used to remove particles that are not raindrops based on particle diameter and velocity relationships for rain (medium grey), hail (dark grey), and graupel (black grey). The light grey lines represent fall velocity-diameter relationships for rain, graupel, and hail respectively. Particles were also filtered out in certain areas of the diagram to remove margin fallers, splashing drops, or strong wind effects. This image was adapted from Fig. 5a in Friedrich et al. (2013).

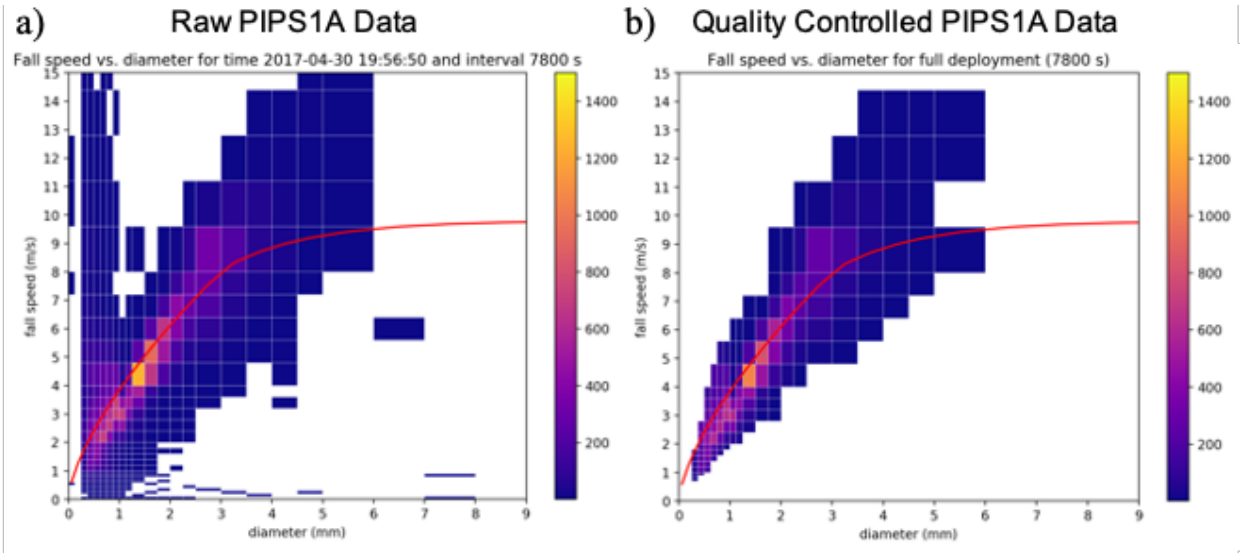

Figure 4-3. Fall speed vs. diameter plots for the 130-min window (7800 s) of the PIPS1A deployment for (a) the raw PIPS1A data; and (b) the quality-controlled data. The color shading represents the drop count in each bin where the red line is the theoretical relationship between fall speed and diameter.

4.2.3 Surface observations data

The surface observation data assimilated into ARPS consist of Automated Surface Observing System (ASOS) 5-min observations (https://www.ncdc.noaa.gov/data-access/land-based-station-data/land-based-datasets/automated-surface-observing-system-asos, NCEI Automated Surface Observing System (ASOS) 2020). The ASOS network consists of approximately 860 stations operated by the NWS, Federal Aviation Administration (FAA), FAA Expansion, Navy, and United States Air Force. Only ASOS stations located in the given ARPS domain were assimilated. When the 5-min data is assimilated, the model representation of the near-surface environment and its evolution is improved. 5-min ASOS data were used from 0600-2300 UTC on 30 April 2017.

4.2.4 Radar data

The NWS WSR-88D S-band radar data were collected from 6 different WSR-88D locations: Huntsville, AL (KHTX), Birmingham, AL (KBMX), Columbus Air Force Base, MS (KGWX), Memphis, MS (KNQA), Nashville, TN (KOHX), and Jackson, MS (KDGX) (https://www.ncdc.noaa.gov/nexradinv/, NCEI Radar Data 2017). Level 2 radar data are collected (when available) for each radar from 1200 to 2300 UTC. WSR-88D data were used not only to assimilate radar data into ARPS via the EnKF, but also to make comparisons of the modeled Z to Z at the given PIPS location captured by the closest radar (KGWX or KHTX). A full description of which radars were assimilated for which grid spacing intervals and the location of the radars in respect to the model domain is found in section 5.1.

4.3 Numerical model data

4.3.1 NAM model data

The NAM model data were retrieved for three NAM forecast cycles (0600 UTC, 1200 UTC, and 1800 UTC) on 30 April 2017 (https://www.ncdc.noaa.gov/data-access/model-data/model-datasets/north-american-mesoscale-forecast-system-nam, NCEI North American Mesoscale Forecast System (NAM), 2017). The NAM model data is used to generate the initial conditions and background conditions (ICBC) for the 6-km ARPS data assimilation experiments that served as the outer grid within which the 3- and 1-km experiment grids were nested. These experiments are described in the next chapter.

CHAPTER 5. METHODOLOGY

5.1 Numerical model

5.1.1 Configuration

The ARPS model employed the EnKF to assimilate surface observations and radar data for the tornadic QLCS on 30 April 2017. The time period of interest is 1800-2200 UTC 30 April 2017, as the QLCS moved over the PIPS locations in northern Alabama. Three nested data assimilation experiments (6-km, 3-km, and 1-km) were performed for each of the nine different initial CCN concentrations (100 cm^{-3}, 300 cm^{-3}, 500 cm^{-3}, 750 cm^{-3}, 1,000 cm^{-3}, 1,250 cm^{-3}, 1,500 cm^{-3}, 1,750 cm^{-3}, and 2,000 cm^{-3}) resulting in a total of twenty-seven experiments. Several test experiments were performed to fine tune parameters that resulted in a simulation that represented the observed QLCS and other atmospheric variables prior to conducting the 27 experiments analyzed in this study. These test experiments and their usefulness are discussed in section 6.1. The outermost 6-km grid of ARPS experiments started at 0600 UTC 30 April 2017 in order for ARPS to best represent the atmospheric conditions present when the QLCS moved over the domain. A timeline of the experiments performed is provided in Fig. 5.1. Each experiment consisted of 40 ensemble members and 53 vertical levels. The use of 40 ensemble members is large enough for reasonable ensemble spread, covariance structures and root-mean-square (RMS) analysis errors, but small enough to still be computationally efficient (Houtekamer and Mitchell 1998).

The first data assimilation experiment performed for each CCN concentration was a 6-km experiment with a grid spacing of 303 x 303 6-km grid cells (Fig. 5.2). Simulations with initially horizontally homogeneous vertical profiles of CCN concentrations on the 6-km grid ranging from 100-2,000 cm^{-3} were conducted. The 6-km experiments used the 0600 UTC NAM for ICBC for

0600-1200 UTC, the 1200 UTC NAM for ICBC from 1200-1800 UTC, and the 1800 UTC NAM from 1800-2300 UTC. A spin-up was performed from 0600-1200 UTC to allow for resolved structures smaller than that represented in the initial conditions to develop. The 6-km experiments produced output every 5 min (300 s) with data assimilation via the EnKF performed every 15 min (900 s) from 1200-2300 UTC. Surface observations were assimilated from 5-min ASOS data (NCEI Automated Surface Observing System (ASOS) 2020). The T, dew point temperature (T_d), p, and u and v components of the wind were assimilated from the surface observations. No radar assimilation was performed on the 6-km grid.

Experiments with a grid spacing of 153 x 153 3-km grid cells (Fig. 5.2) were nested inside the 6-km experiments such that the 6-km experiments provided the ICBC for the 3-km experiments (i.e. the 6-km CCN 1,000 cm^{-3} experiment was used for the 3-km CCN 1,000 cm^{-3} ICBC). These 3-km experiments had a spin-up time from 1200-1400 UTC. The 3-km experiments were performed from 1400-2200 UTC while producing output every 5 min. The EnKF assimilated surface observations from ASOS data (NCEI Automated Surface Observing System (ASOS) 2020) and Z and radial velocity observations from 6 different WSR-88Ds locations: KHTX, KBMX, KGWX, KNQA, KOHX, and KDGX every 5 min. These radars were selected due to their overlap on the 3-km grid (Fig. 5.2). An internal minimum Z threshold was set to -99.00 dBZ for all 3-km experiments so that all Z data including clear air data was assimilated via the EnKF.

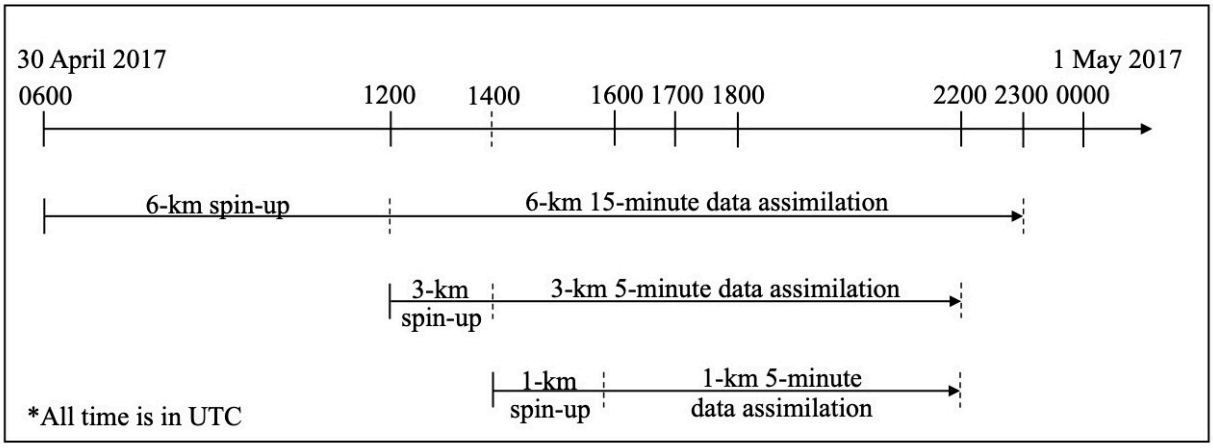

Figure 5-1. A timeline of the 6-km, 3-km, and 1-km experiments. All times are in UTC.

The 1-km grid was 243 km x 243 km in size and nested in the outer 3-km experiment for the corresponding CCN concentration (Fig. 5.2). Experiments on the1-km grid have an initial spin-up from 1400-1600 UTC before running from 1600-2200 UTC while assimilating radar data and surface observations from 5 different WSR-88D locations: KHTX, KBMX, KGWX, KNQA, and KOHX. Radar observations from KDGX were not assimilated because they did not significantly overlap the 1-km grid domain. The same minimum Z threshold of -99.00 dBZ was used when assimilating radar data in the 1-km experiments. Surface observations from ASOS data (NCEI Automated Surface Observing System (ASOS) 2020) were also assimilated. The 1-km experiments started at 1400 UTC to allow for the QLCS to be mature by the time it passed over the PIPS location from 1800-2200 UTC. Model output was produced at 5-min intervals from 1600-1815 UTC and then 1-min (60 s) intervals from 1815-2200 UTC to allow for a minute-by-minute comparison with the observed PIPS data.

All 14 tilts in each level-2 radar volume were remapped from the original radar coordinates in the horizontal directions only (i.e. they were left at the original sweep heights) onto the 3-km or 1-km grid prior to being assimilated. Following the approach of Supinie et al. (2016), the starting

time for each radar volume assimilated for each radar was required to be within 5 min prior to the assimilation time such that the assimilation time fell within the volume sampling interval (i.e. the KBMX radar data volume assimilated at 1200 UTC was required to start between 1155–1200 UTC). Testing showed that the assimilation occasionally resulted in instabilities in the model. To prevent these, u and v were not updated from assimilated Z in the 1-km experiments (Y. Jung, personal communication 2020). Additionally, to help limit spurious error growth in the 1-km experiments, the minimum mixing ratio (Q_x), minimum number concentration (N_x), and minimum reflectivity (Z_x) were adjusted from 0. Q_x was set to 1.0×10^{-14} kg kg^{-1}, N_x to 1.0×10^{-4} m^{-3} dry air, and Z_x to 1.0×10^{-32} m^3. The minimum hydrometeor volume (V_x) was left at 0 m^{-3} of hydrometeor air (not dry air).

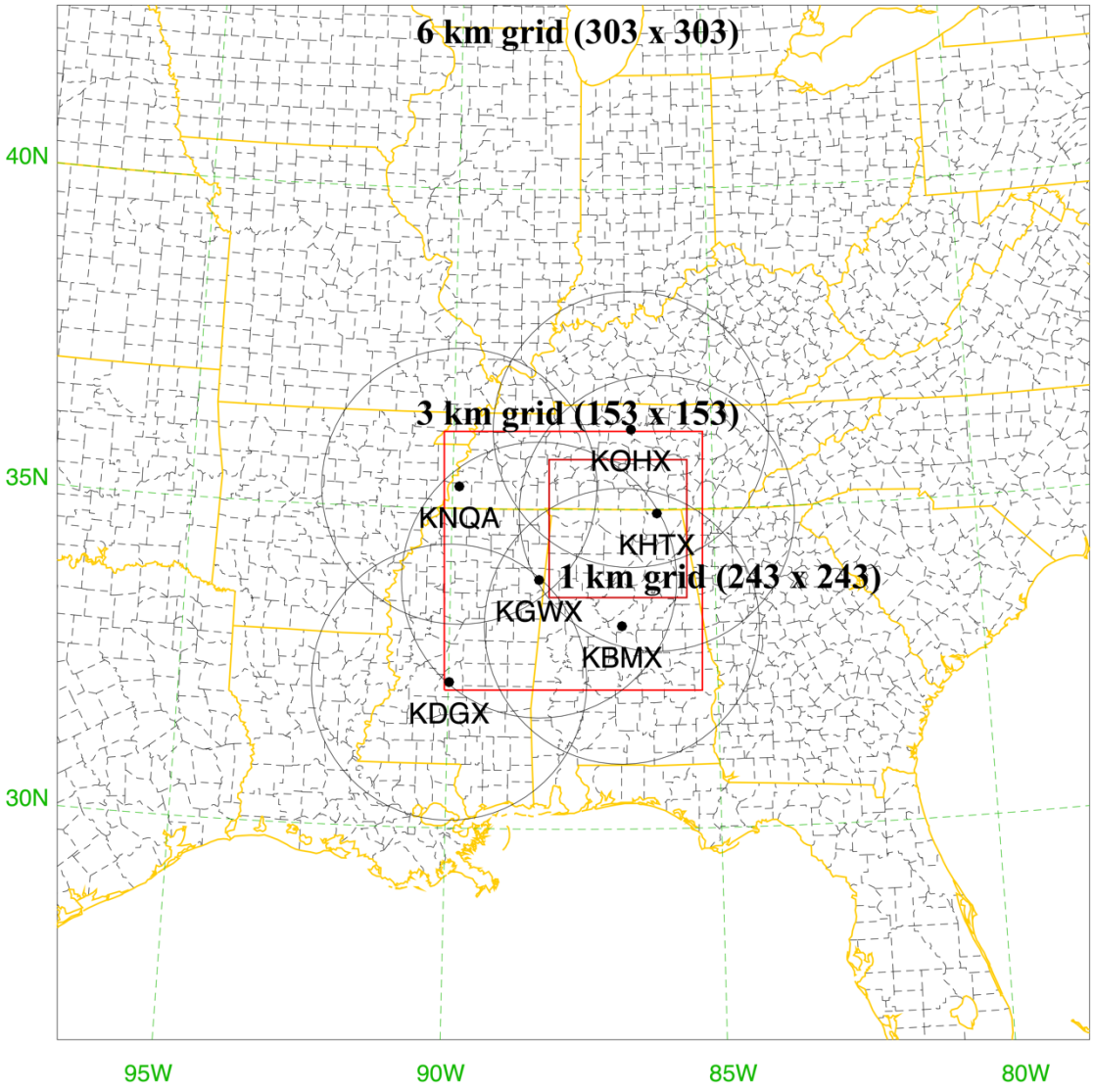

Figure 5-2. The location of the 6-km, 3-km, and 1-km grids with 6 WSR-88D radar location and range rings (245 km) overlayed. The 6-km grid is the entire image, where the 3-km (1-km) grid is the outer (inner) red square.

5.1.2 ARPS parameters

Like any NWP model, ARPS allows for various parameters to be adjusted to control different aspects of the simulation. The model was run in fully compressible mode. The advection solution method used the original leapfrog formulation with the Robert-Asselin time filter coefficient set to 0.05. Momentum and scalar advection were solved for the fourth order in the horizontal and vertical. The Coriolis parameter terms involving both horizontal and vertical wind are included, and the Coriolis parameters are latitude dependent with the effects of the spatial gradient of map factor and of Earth's curvature also included. As described in Xue et al. (2003), the long and short-wave radiation package used is based on the National Aeronautics and Space Administration (NASA) Goddard Space Flight Center (Chou 1990; 1992; Chou and Suarez 1994).

Surface fluxes are calculated from the stability-dependent surface drag coefficients and predicted surface temperature and surface volumetric water content. Land and water were treated differently. The planetary boundary layer (PBL) depth was diagnosed based on Xue et al. (1996). Surface characteristics were defined using a data file containing soil and vegetation type, leaf area index and surface roughness (NSSC, 1994; Kineman and Ohrenschall 1992; Kidwell, 1990). Terrain height is specified using a global digital elevation model (DEM), Global 30 Arc-Second Elevation (GTOPO30) for the various grid domains (Earth Resources Observation and Science Center/U.S. Geological Survey/U.S. Department of the Interior 1997). Elevations in GTOPO30 are regularly spaced at 30 arc-seconds (approximately 1-km) globally from -90° S to 90° N and -180° W to 180° E.

5.1.3 Microphysics scheme

The NSSL-TM microphysics scheme was integrated into ARPS-EnKF and used in this study. Both large ice categories were activated. Three moments of the gamma size distribution

(mixing ratio, number concentration, and Z) were predicted for rain, graupel/frozen drops, and hail. The density of graupel and hail were also predicted. Experiments with varying prognostic CCN concentrations as defined above were conducted. The CCN concentration defined controls only the initial background CCN concentration as mentioned in section 4.1.

5.2 Numerical model

5.2.1 Extracting model output to PIPS locations

Various parameters from the 60 second model output of a given 1-km experiment were compared to the observed 60 second PIPS data including: median drop diameter (D_0), Z, Z_{DR}, p, θ, θ_e, pressure, wind (speed and direction), and water vapor mixing ratio (q_v). The PIPS were compared to the model output during the passage of the initial convective region, transition region, and trailing stratiform region of the QLCS for each PIPS location from: 1815–1956 UTC (PIPS1A), 1815–2007 UTC (PIPS1B), 2000–2200 UTC (PIPS2A) and 1846–1929 UTC (PIPS2B). To compare the model output with the PIPS observations, the model output had to be extracted for the grid point in the model the PIPS location corresponded to for each ensemble member. A time series containing the model output for each ensemble was then created allowing for a comparison between the model output and observed PIPS data.

5.2.2 Variables calculated and compared

The model output was retrieved from the lowest level of the model (~9 m to 10 m above ground level (AGL)) and directly compared to PIPS observations with data at approximately 1 m AGL. All model variables compared with the corresponding PIPS observations were either present in the history dumps or could be derived from them. Z and Z_{DR} were derived from the observed

PIPS DSDs using a T-matrix-based forward operator in the form of scattering amplitude lookup tables (Jung et al. 2008a,b). The observed Z and Z_{DR} at the PIPS location from the PIPS were then compared with the Z and Z_{DR} computed with the same forward operator applied to the model output. θ and θ_e were derived from the observed T, p, and RH using the standard definition of θ and the formula from Bolton (1980), respectively. θ is the predicted state variable from the model, while θ_e is derived in the same way as for the observations. Water vapor mixing ratio (w) was derived from the observed T, p , and RH.

5.2.3 Statistical comparison

Multiple statistical comparisons were performed on the PIPS observations and ensemble member output to quantify the performance of the experiments with different CCN concentrations. Statistics were only calculated when data was present at a given time for both the PIPS observations and ensemble member output. If the PIPS observations did not pass the quality control check or there were no observations the data were not included in the statistics. One way to measure error between the PIPS observations and ensemble member output is bias. Bias allows for the average magnitude and direction of error to be determined. A negative bias is indicative of the model output being lower (underpredicted) on average than the PIPS observations, and a positive bias is indicative of the model output being larger (overpredicted) on average than the PIPS observations. Bias is calculated by the equation:

$$Bias = \frac{1}{n}\sum_{i=1}^{n} X_1 - Y_1 \quad (6)$$

with i representing the start time through the total number of minutes of observations for the respective PIPS location, n, X_1 representing the individual ensemble member value for a given minute, and Y_1 representing the PIPS observation of the variable at the same minute. The bias was

calculated for each minute of the PIPS and model output for each ensemble member. The average bias was then calculated by taking the average of each of the 40 ensemble members for the duration of the PIPS and model output comparison.

Another way of measuring the error between the ensemble member output and PIPS observations is to solve for the mean absolute bias. Absolute bias is a way to determine the average magnitude of error, without taking the direction into account. The equation is written as:

$$Absolute\ Bias = \frac{1}{n}\sum_{i=1}^{n}|X_1 - Y_1| \quad (7)$$

Additionally, the correlation coefficient was calculated to quantify the association between the observed PIPS values and the ensemble member output. Pearson's (product moment) correlation coefficient is used in this study which is the ratio of the covariance of the individual ensemble member (x) and the PIPS observation (y) to the product of their standard deviations:

$$r = \frac{\sum(x_i - \bar{x})(y_i - \bar{y})}{\sqrt{\sum(x_i - \bar{x})^2 \sum(y_i - \bar{y})^2}} \quad (8)$$

This equation concludes if larger (smaller) values of x tend to correspond to larger (smaller) values of y, the correlation (r) is positive (> 0). Additionally, if larger (smaller) values of x tend to correspond to smaller (larger) values of y, the correlation is negative. No correlation or weak correlation ($r \cong 0$) occurs when there is not clear association between the ensemble member output and PIPS observations. Pearson's correlation is restricted to any real values in the range $-1 \leq r \leq 1$. A value of +1 (-1) represents a perfect positive (negative) relationship between the ensemble member output and PIPS observations. A larger positive value of r represents a stronger positive linear relationship, whereas a larger negative value of r represents a stronger negative linear relationship. The correlation was calculated for the duration of the PIPS and model output

comparison for each ensemble member. The average correlation for a given CCN concentration experiment represents the average of all 40 ensemble members.

To account for an apparent small but systematic time lag between the PIPS and corresponding model time series, shifted statistics were calculated for each PIPS location for all CCN concentration experiments. The model output for each of the 40 ensemble members were shifted up to 6 minutes forward or backward in time on a per-variable basis and the bias, absolute bias, and correlation were recalculated at each minute. The best shifted statistics for a given PIPS location and CCN concentration experiment were determined as the shift that resulted in the lowest absolute bias and highest correlation which corresponded to shifting the model to the onset of the observed precipitation in the leading convective region of the QLCS for each PIPS location in every CCN concentration experiment. The time with the lowest absolute bias usually corresponded to the time with the highest correlation. For certain PIPS locations in different CCN concentration experiments, the shift resulting in the lowest absolute bias and highest correlation lead to a slight increase in bias. For some PIPS locations in various CCN concentration experiments, the "best" statistics were those without shifting the model output. This frequently occurred for the 1,000 CCN cm^{-3} experiments.

The overall bias, absolute bias, and correlation for each 1-km CCN concentration experiment were also calculated for the unshifted and shifted statistics. This was done by combining the PIPS observations and ensemble member output into a single dataset and calculating the overall average bias, absolute bias, and correlation coefficient between the model output for each experiment and the PIPS data. This enabled some of the noise between PIPS locations to be eliminated and any overall trends in a given variable as CCN concentration changes to be evaluated.

CHAPTER 6. RESULTS

6.1 Test experiment results

To achieve experiments that best represent the observed atmospheric conditions, test experiments were performed on the 3-km and 1-km grid spacing intervals. Initially, the 3-km (1-km) experiments both assimilated surface observations and six (five) WSR-88D radars with a minimum Z threshold of 10 dBZ. This produced spurious convection ahead of the main QLCS that was not present in observations (Fig. 6.1). Therefore, experiments assimilating surface observations with no Z threshold were performed. This suppressed some of the spurious convection ahead of the QLCS in the experiment by assimilating clear air data (Fig. 6.1b). A few showers and thunderstorms were still present in several ensemble members as reflected in the ensemble forecast mean Z plots shown in Fig. 6.1b, but overall this helped remove the majority of spurious convection ahead of the QLCS.

To attempt to eliminate the remaining spurious convection, experiments without surface observations and with no Z threshold were conducted. It was hypothesized the surface observations made the environment locally unstable due to being warmer or moister than the model background, making the local area unstable in the model. The EnKF localization allows the locally unstable environment of the surface observations to be extended beyond the surface, higher up into model levels through covariance structures potentially producing the spurious convection. Removing the assimilation of surface observations in combination with no Z threshold did not significantly reduce the spurious convection ahead of the QLCS. Instead, not assimilating surface observations decreased the overall value of the simulation by creating a warmer cold pool than experiments that assimilated surface observations. Therefore, all 3-km and 1-km simulations were

performed assimilating surface observations and no *Z* threshold. The *Z* threshold was set to -99.00 dB*Z* for all 3-km and 1-km experiments so all *Z* values including clear air data were assimilated.

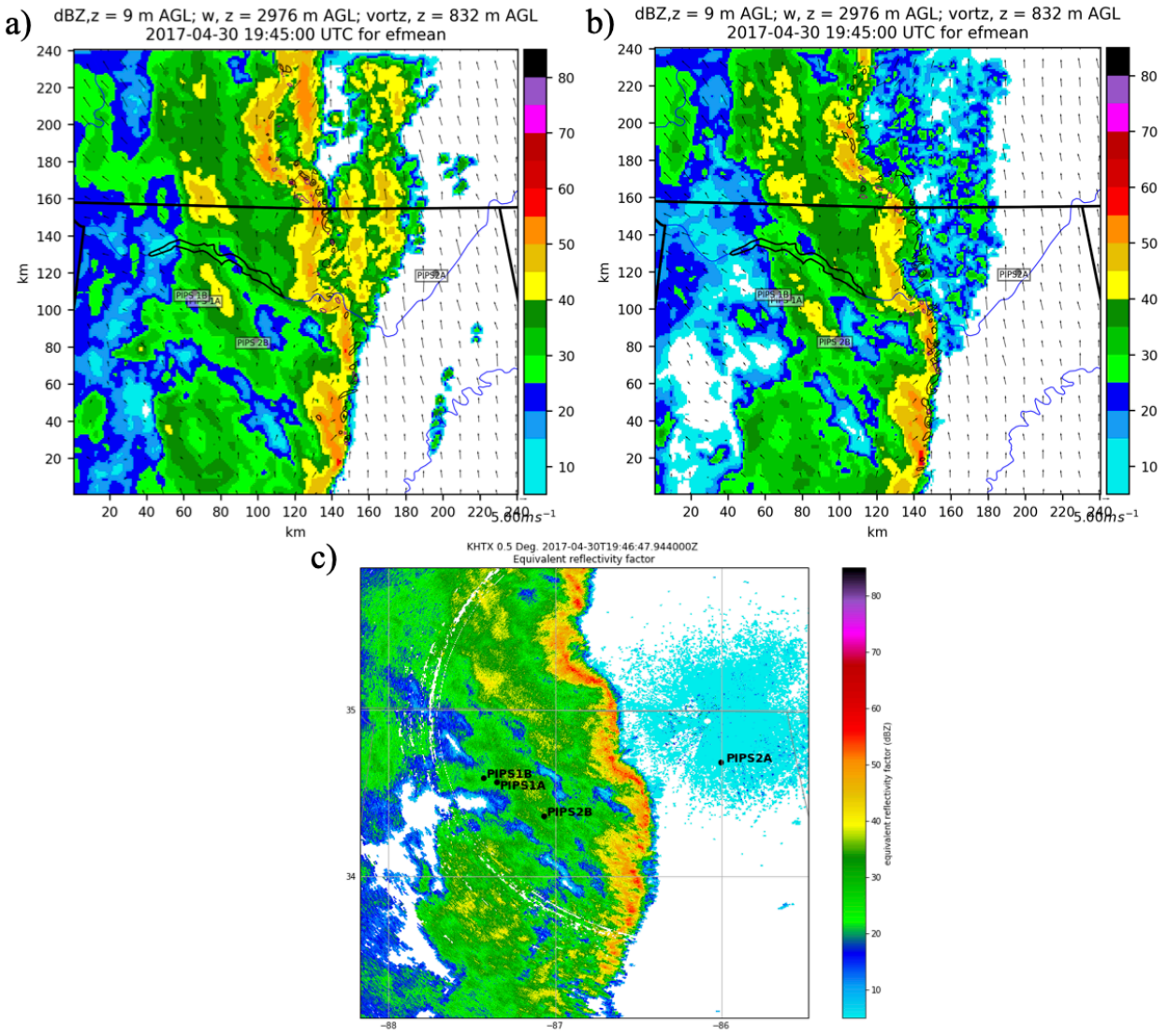

Figure 6-1. The forecast mean *Z*, vertical vorticity (ζ, purple contours), and vertical velocity (*w*, black contours) of all 40 ensemble members at 1945 UTC for (a) the 1-km CCN 1,000 cm^{-3} experiment with a 10 dB*Z* threshold for *Z* assimilation; (b) as in (a), but with no *Z* assimilation threshold; and (c) the observed 0.5° *Z* from KHTX at 1946 UTC.

Initially, experiments (both the 3-km and 1-km experiments) started at 1700 UTC with no spin-up, however, these experiments resulted in too weak of a cold pool in the 3-km and 1-km experiments. Therefore, the 3-km experiments were reran starting at 1200 UTC and the 1-km experiments at 1400 UTC to better capture the background environmental conditions. The experiments that originally started at 1700 UTC on the 3-km and 1-km grids did not have adequate time to develop the QLCS and therefore the cold pool was weaker (Fig. 6.2a). Starting the outer 3-km experiments, used for ICBC in the 1-km simulations, earlier in time resulted in a more mature QLCS by the time the QLCS approached the 1-km grid with a stronger cold pool (Fig. 6.2b). The colder cold pool aligns closer to the observed cold pool temperatures from the PIPS as discussed in section 6.4.

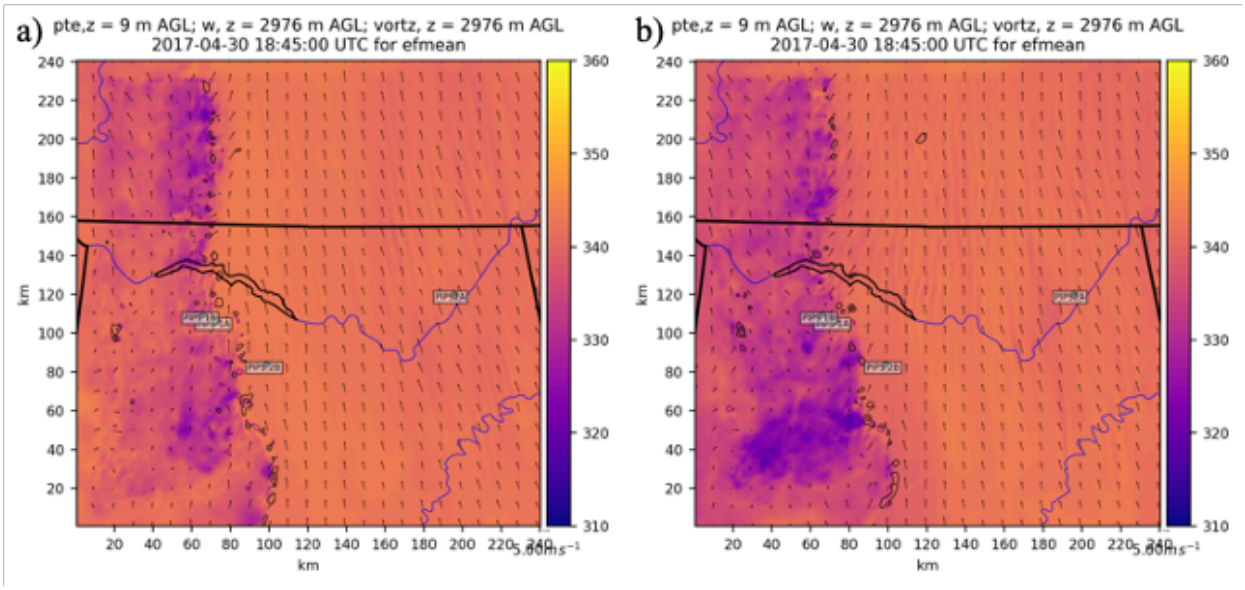

Figure 6-2. The forecast mean θ_e, ζ, and w of all 40 ensemble members for 1845 UTC for the 1-km CCN 1,000 cm^{-3} experiment with (a) the 3-km and 1-km experiments starting at 1700 UTC; (b) as in (a), but with the 3-km (1-km) experiment starting at 1400 (1600) UTC.

6.2 ARPS model output

The model output from the 6-km and 3-km experiments is not directly analyzed in this study. Instead, the results discussed focus on the 1-km results from the nine different CCN concentrations

(CCN 100 cm^{-3}, 300 cm^{-3}, 500 cm^{-3}, 750 cm^{-3}, 1,000 cm^{-3} , 1,250 cm^{-3}, 1,500 cm^{-3}, 1,750 cm^{-3}, and 2,000 cm^{-3}). The 6-km (3-km) simulations were evaluated to ensure they represented the overall background environment and provided adequate ICBC for the 3-km (1-km) experiments. The timing of the QLCS was slower than the observed QLCS in all 6-km simulations because the ICBC provided by the NAM were slow with the timing of the QLCS. Additionally, poorly resolved mesoscale circulations within the QLCS on the 6-km grid did not help correct the time delay. The assimilation of radar data in the 3-km experiments corrected for the delay present in the ICBC from the 6-km simulations. Overall, the 6-km and especially the 3-km experiments represented the timing and shape of the observed QLCS well and were essential in achieving the 1-km experiments discussed.

6.2.1 Simulated QLCS structure

The 1-km ARPS-EnKF experiments produced model output representative of the observed QLCS in all nine 1-km experiments with CCN concentrations ranging from 100–2,000 CCN cm^{-3}. This is evident in the forecast mean Z of the 40 ensemble members at 1845 UTC (Fig. 6.3) and 2045 UTC (Fig. 6.4) for the five 1-km experiments shown. The 1845 UTC timestep reveals the mature QLCS approaching PIPS2B after previously passing over PIPS1A and PIPS1B. Fig. 6.4 demonstrates the QLCS two hours later at 2045 UTC approaching PIPS2A. The QLCS has weaker reflectivities at 2045 UTC across all 1-km simulations than at 1845 UTC, which accords well with the observed Z of the QLCS from local WSR-88D radars (Fig. 6.4f).

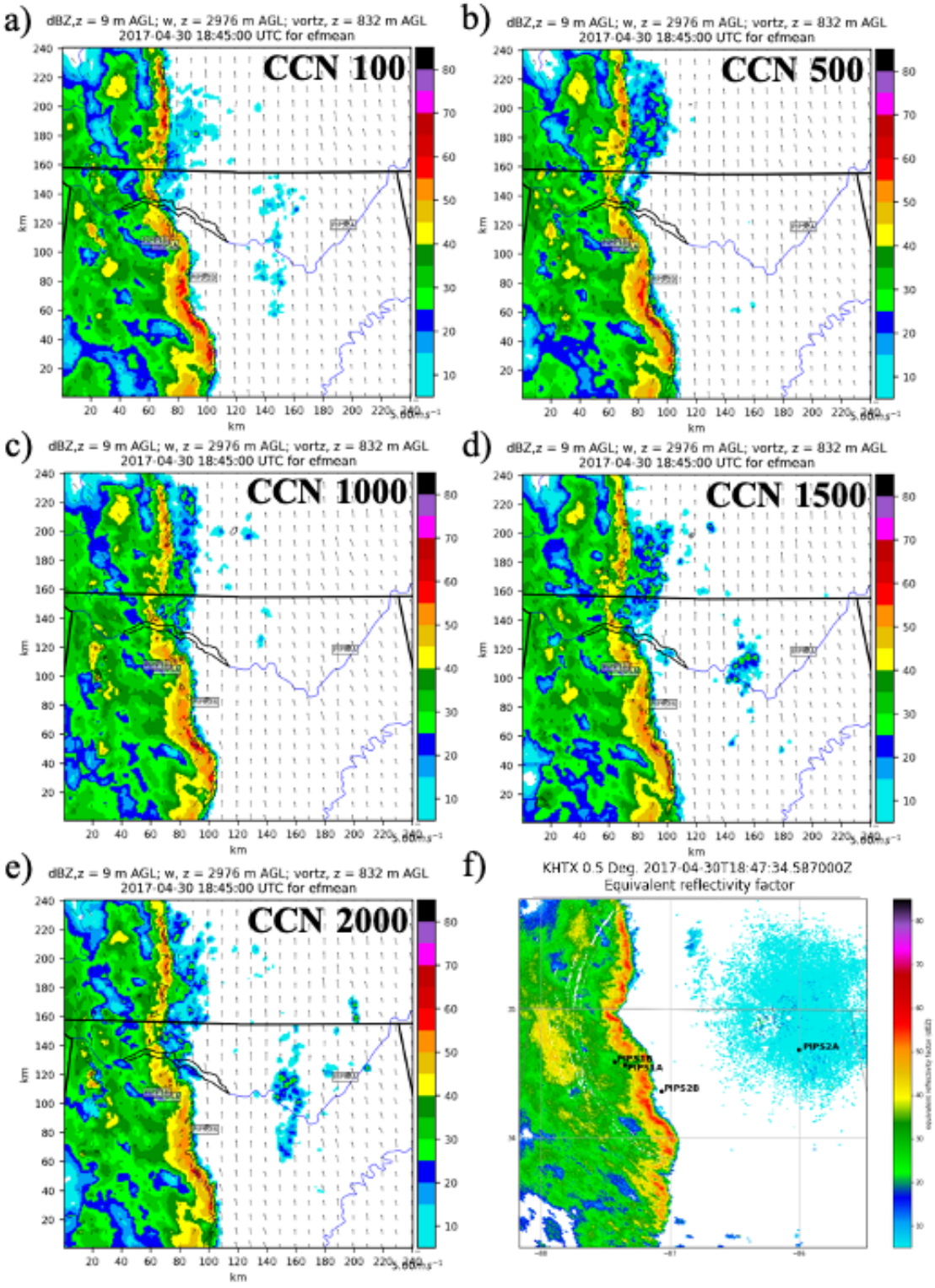

Figure 6-3. The forecast mean Z, ζ, and w of all 40 ensemble members for 1845 UTC for the 1-km experiments for the following CCN concentrations in units of cm^{-3} (a) 100; (b) 500; (c) 1,000; (d) 1,500; (e) 2,000; and (f) the observed 0.5° Z from KHTX at 1847 UTC.

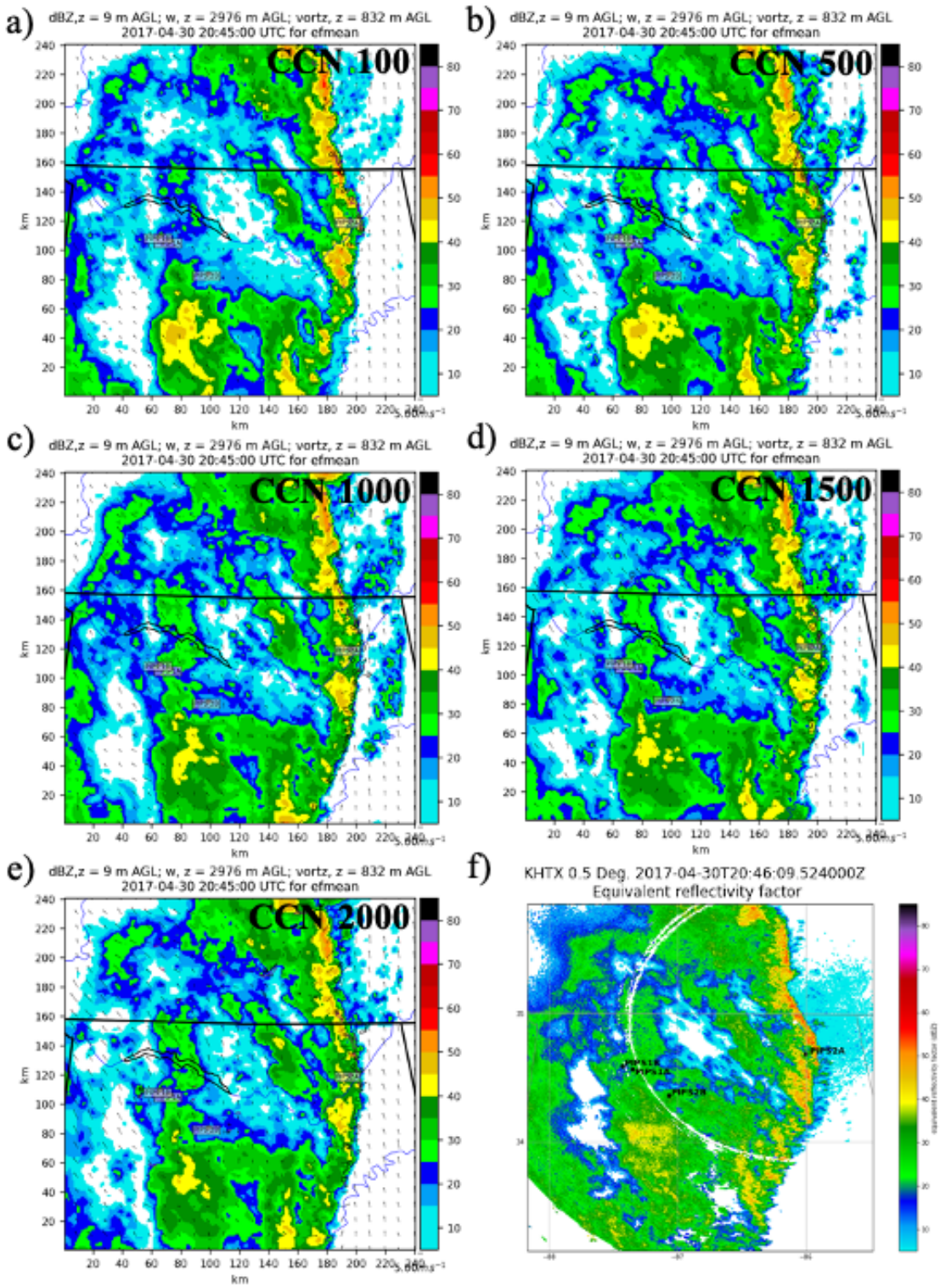

Figure 6-4. As in Fig. 6.3, but with the forecast mean valid 2045 UTC and the 0.5° *Z* valid 2046 UTC.

Subtle differences exist when comparing the structure of the five 1-km experiments shown in Fig. 6.3 and Fig. 6.4. The lower CCN concentrations (CCN 100–500 cm^{-3}) have the highest *Z* along the leading convective region of the QLCS. *Z* values decrease along the leading convective region as the CCN concentrations increase. Fig. 6.3a (CCN 100 cm^{-3}) has widespread maximum *Z* values of 55–60 dB*Z* along the leading convective region, whereas Fig. 6.3e (CCN 2,000 cm^{-3}) has lower maximum *Z* values of 50–55 dB*Z*. The same is true in Fig. 6.4a and 6.4e, however, the spatial coverage of higher reflectivities is lower because the QLCS weakened from 1845–2045 UTC. The 0.5° elevation angle *Z* from KHTX at 1847 UTC and 2046 UTC support the higher *Z* values found in the leading convective region of the lower CCN concentration experiments. The shape along the leading edge of the QLCS is well simulated across all CCN concentration experiments, likely because of the assimilation of radar data from five WSR-88Ds every 5 min.

Showers formed in the model ahead of the QLCS were not observed via radar or surface observations. In Fig. 6.3 at 1845 UTC, showers were observed in the model output ahead of the QLCS in two regions: 1) west of PIPS2A, and 2) ahead of the QLCS along the Alabama and Tennessee line. The intensity and spatial coverage of these spurious showers increases as the CCN concentration increases (Fig. 6.3). In Fig. 6.3a, the forecast mean *Z* of the showers ahead of the QLCS for CCN 100 cm^3 have maximum reflectivities of 25 dB*Z* whereas for CCN 1,000–2,000 cm^3 (Fig. 6.3c–e) the maximum *Z* for these showers approaches 40 dB*Z*. Similar conclusions can be made in Fig. 6.4. These showers are not present in every ensemble member for each CCN concentration, however, the frequency of showers ahead of the QLCS among ensemble members increases as indicated by increase in spatial coverage and magnitude of *Z* in the forecast mean *Z* in Fig. 6.3 and Fig. 6.4. The differences in *Z* in the transition and trailing stratiform region of the

QLCS is analyzed in section 6.3.4 and section 6.3.5. The overall coverage and placement of heavier convective cores in the forecast mean of the model at both 1845 UTC and 2045 UTC aligns with WSR-88D data (Fig. 6.3f and 6.4f).

6.3 1-km ARPS simulations to PIPS disdrometer comparisons

As discussed in section 5.2, the 1-km model output was extracted at the four PIPS locations to make time series and statistical comparisons with observed PIPS variables. D_0, Z, and Z_{DR} are analyzed to evaluate how well the NSSL-TM microphysics scheme represents different DSD-related quantities for different CCN concentrations. D_0 increases as the CCN concentration increases (e.g., Squires 1958; Squires and Twomey 1966; Warner and Twomey 1967; Warner 1968; Rosenfeld 1999; Rosenfeld and Ulbrich 2003; Andreae et al. 2004; Tao et al. 2012), so this study looks to confirm these trends during a QLCS in the SE-US. Z is sensitive to both the amount and size of drops in a volume but is weighted toward larger sizes; a lesser quantity of larger drops can have a higher Z value than a greater quantity of smaller drops. Additionally, Z_{DR} is dependent on the size of the raindrops (by virtue of their increasing oblateness) but is independent of the total amount in a volume. Together, these parameters provide information about the underlying DSD that can be connected to the results of previous studies based on the analysis of disdrometer and radar observations. The thermodynamics of the experiments are analyzed by evaluating θ, θ_e, and w. Lastly, the wind speed and direction are evaluated. Blue box and whisker plots as shown in Fig. 6.5 will be discussed throughout the results section. These plots demonstrate the distribution of the ensemble member model output for a given variable compared to the observed variable (red line) at 1-min intervals. When the observed variable from the PIPS does not pass the quality control metrics described in section 4.2.2, the observation is removed for that time. The blue boxes show the quartiles of the ensemble output for the given variable. The whiskers extend to show the rest

of the distribution. Outliers of the dataset are determined by a point being 1.5 times above (below) the upper (lower) quartile (Seaborn 2021). These box plots allow for the distribution of ensemble members to be visualized between the different CCN concentrations.

The difference in timing between the various CCN concentrations will be discussed throughout the results and could be related to several factors. One possibility is how the radar data were assimilated every 5 min via the EnKF. The same radar data were assimilated into each of the nine CCN concentration experiments, so the issue is not related to different data being assimilated. However, the radar data assimilated are assumed to be valid at the time of assimilation which is not strictly true. A radar scan takes approximately 5 min to complete, therefore, when the different levels of radar data are remapped and assumed to be valid at the same time, this could lead to a constant offset in timing among all experiments before accounting for differences in precipitation processes among the different CCN concentrations. For example, the assimilation at 1800 UTC would use radar data from 1755–1800 UTC but assume all levels of radar data are valid at 1800 UTC (the time radar data are remapped prior to and assimilated at), which is not a valid assumption. The radar data assimilated could account for the model output being delayed when compared to the observations since data at a given time step is assimilated up to 5 min later than observed via radar. The magnitude of the delay between the PIPS locations and different CCN concentrations is not constant. This may be related to how the model handles precipitation processes for the different CCN concentrations but is not further investigated here.

6.3.1 Unshifted D_0 comparisons

Comparing model output from the NSSL-TM microphysics scheme with observed disdrometer data has not been done before. The quality controlled D_0 measured by the OTT Parsivel^2 laser disdrometers are compared with the unshifted 1-km experiment model output for

all nine CCN concentrations at the PIPS locations (Fig. 6.5). From 1815–1830 UTC (Fig. 6.5) and 2000–2030 UTC (Fig. 6.6), the model output for the CCN concentration experiments produced D_0 not observed from the spurious showers ahead of the QLCS in the experiments discussed in the previous section. In accordance with previously discussed results, more showers are present ahead of the QLCS as the CCN concentration increases as seen in Fig. 6.5 and Fig. 6.6 by the increase in the width of the box and whiskers.

Several studies have analyzed DSD measurements in squall lines over the tropics (e.g., Maki et al. 2001, Nzeukou et al. 2004, Moumouni et al. 2008). The leading convective region was observed to have larger D_0 than the trailing stratiform region. Few studies have discussed DSD measurements in squall lines in mid-latitude regions such as the SE-US. Chen et al. (2016) used four disdrometers to study characteristics of rain DSDs in mid-latitude squall lines over eastern China. The leading convective edge was found to have a larger D_0 than the transition and trailing stratiform region. The trailing stratiform region was observed to have a larger D_0 than the transition region (Chen et al. 2016). The observed D_0 and model output D_0 across all experiments for PIPS1A (Fig. 6.5) and PIPS2A (Fig. 6.6) have the largest D_0 with the leading convective region which agrees with past studies (e.g., Makai et al. 2001; Nzeukou et al. 2004; Moumouni et al. 2008; Chen et al. 2016). However, at PIPS2A, D_0 does not increase from the transition region to the trailing stratiform region.

D_0 increases as the CCN concentration increases, which accords with previous studies of more efficient cold rain processes in higher CCN concentration environments with relatively larger drops from melting ice compared to warm rain processes (e.g., Squires 1958; Squires and Twomey 1966; Warner and Twomey 1967; Warner 1968; Rosenfeld 1999; Rosenfeld and Ulbrich 2003; Andreae et al. 2004; Tao et al. 2012). This is evident in the trailing stratiform region of the QLCS

over PIPS1A in Fig. 6.5 from approximately 1855–1955 UTC. In the lower CCN concentrations, D_0 is underpredicted at times throughout the trailing stratiform region (Fig. 6.5a–c). For the intermediate CCN concentrations (CCN 750–1,250 cm^{-3}), the modeled D_0 is close to the observed D_0 throughout the trailing stratiform region (Fig. 6.5d–f). The higher CCN concentrations (CCN 1,500–2,000 cm^{-3}) overpredict the D_0 at times throughout the trailing stratiform region from approximately 1850–1910 UTC (Fig. 6.5g–f). The intermediate CCN concentration simulations produce model output closest to observations for PIPS1A since the lower (higher) CCN concentrations underpredict (overpredict) the observed D_0 at times. Similar results are found across PIPS1B and PIPS2B.

To analyze any potential differences as the QLCS weakened, D_0 from PIPS2A is analyzed (Fig. 6.6). Similar results to PIPS1A are found with D_0 increasing as the CCN concentration increases. The main difference is the lower CCN concentration simulations (Fig. 6.6a–c) accord better with the observations of D_0 in the trailing stratiform region than the intermediate (Fig. 6.6d–f) and higher (Fig. 6.6g–i) CCN concentration experiments. The intermediate CCN concentration experiments do not overpredict the D_0 as much as the higher CCN concentrations. The lower CCN concentration simulations underpredict the observed D_0 in the leading convective region by 1–2 mm. The intermediate CCN concentration experiments for PIPS2A (Fig. 6.6d–f) again appear to accord best overall with the observed D_0 since D_0 is not significantly over or under modeled throughout the time series.

Across all PIPS locations, the lower CCN concentration simulations are the slowest with the onset of precipitation. The delay of the onset of precipitation decreases as the CCN concentration increases (Fig. 6.5 and Fig. 6.6). Overall, the NSSL-TM microphysics scheme produces model output D_0 that accords well with D_0 observed from the PIPS.

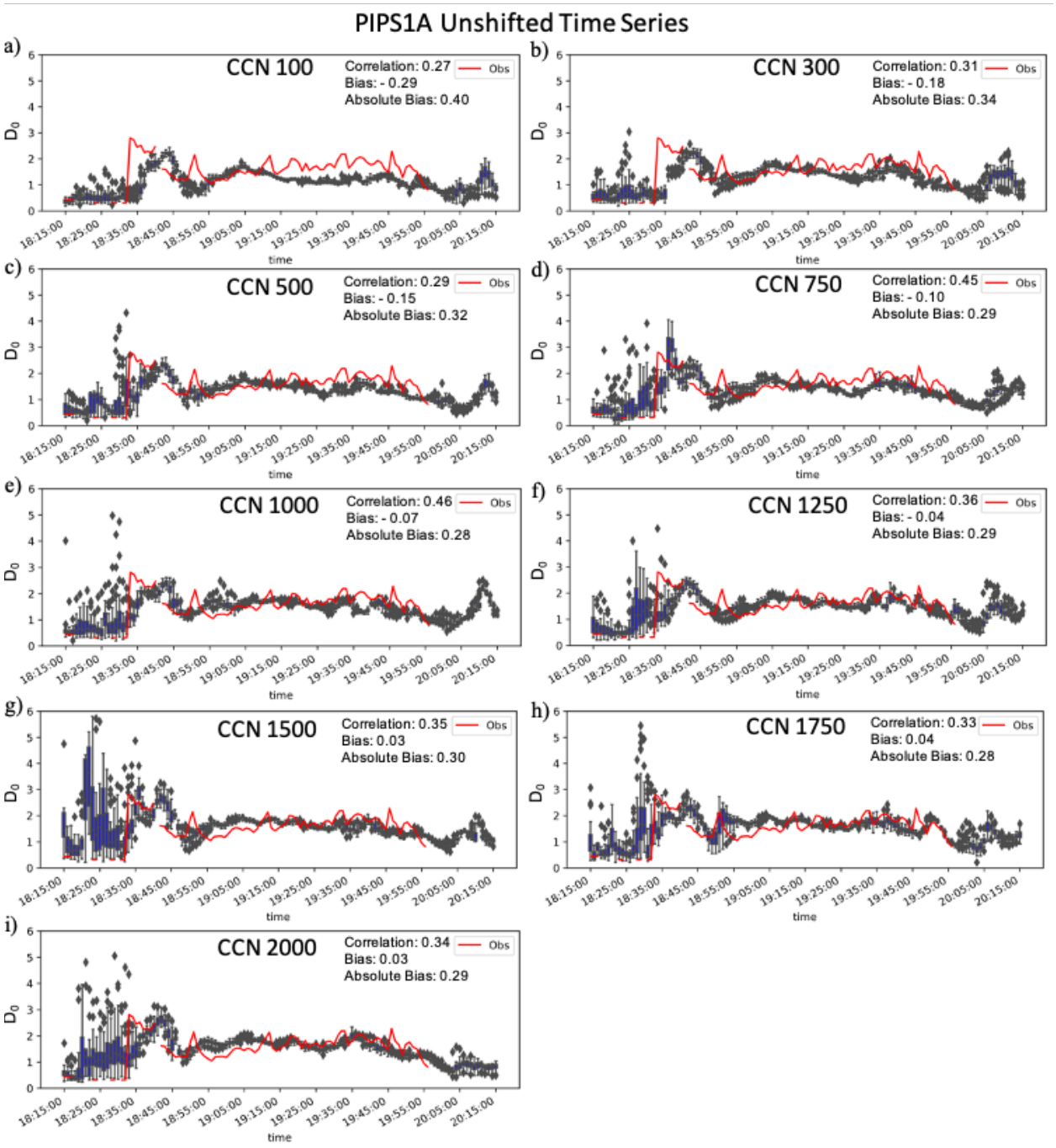

Figure 6-5. The unshifted ensemble member spread of D_0 (mm) (blue box plots) and the observed D_0 (red line) for PIPS1A for the following 1-km experiment CCN concentrations in units of cm^{-3}: (a) 100; (b) 300; (c) 500; (d) 750; (e) 1,000; (f) 1,250; (g) 1,500; (h) 1,750; and (i) 2,000.

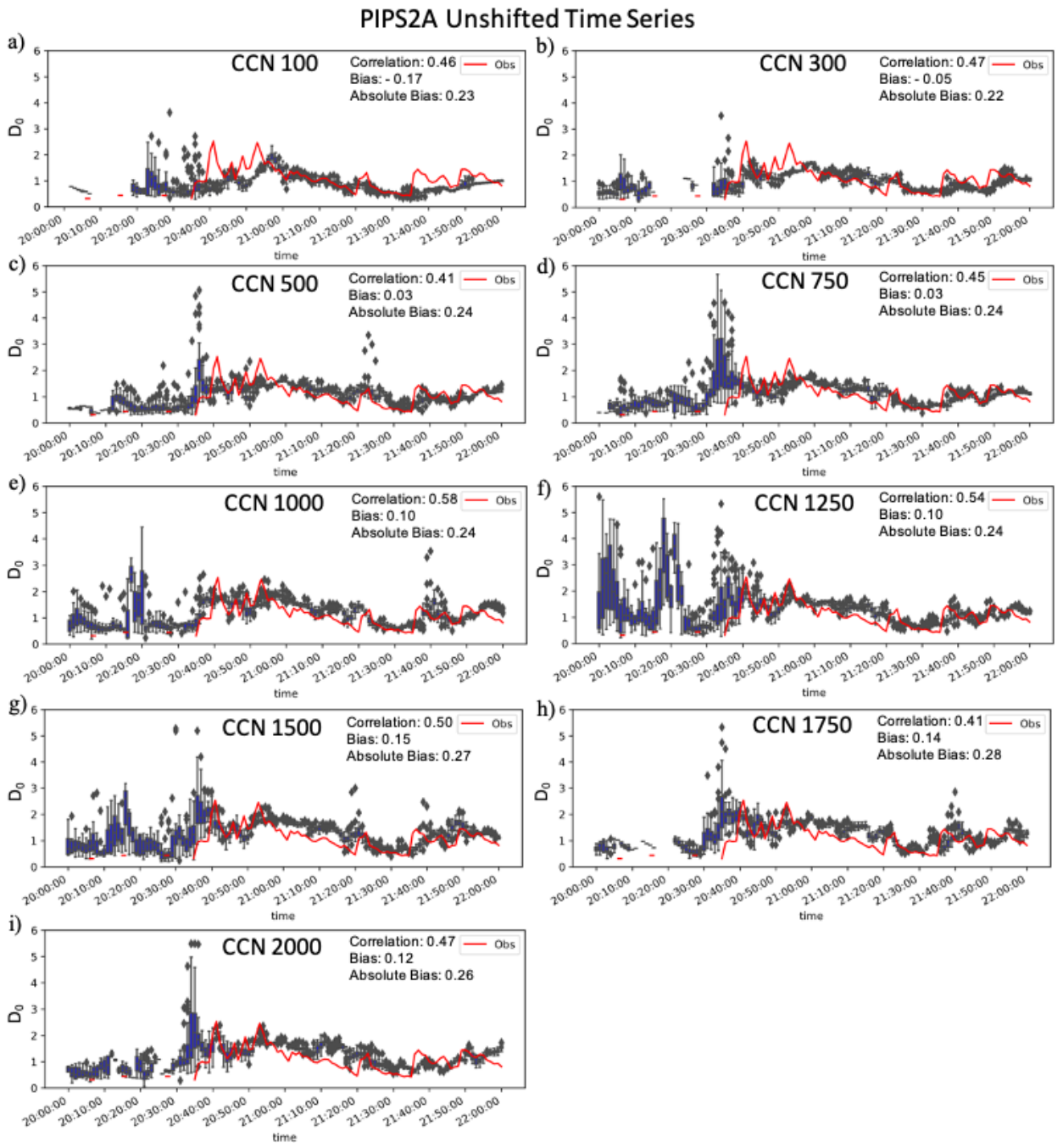

Figure 6-6. As in Fig. 6.5, but for PIPS2A.

6.3.2 Shifted D_0 comparisons

The differences in timing between the observed and the model output D_0 were accounted for by shifting the model output up to 6 min forward in time to align the onset of precipitation in the model close to the observed onset of precipitation by the PIPS. The shifts were applied on a per-variable basis such that the shift in model output that aligns closest to observations could be different between variables (D_0, Z, Z_{DR}, etc.). Aligning the model output to the observed onset of precipitation corresponded to the overall lowest absolute bias and highest correlation between a variable and the observed variable for each PIPS location in all the CCN concentration experiments. This also resulted in more of an equal comparison when analyzing the statistics for the CCN concentration experiments by eliminating differences in timing.

The same results relating to D_0 increasing as the CCN concentration increases are evident in Fig. 6.7 and Fig. 6.8. For all-time series where the model output was shifted and the statistics were recalculated, the lower CCN concentration experiments were shifted the most (typically 4–5 min). The intermediate and higher CCN concentrations were shifted most frequently 1–3 min. There were several intermediate and higher CCN concentration simulations that did not require a shift since the unshifted model output aligned with the onset of precipitation. This occurred for the CCN 500 cm^{-3} experiment (Fig. 6.7d) but did not occur for PIPS2A (Fig. 6.8). Aside from creating a more equivalent comparison shifting the model output to account for timing differences also resulted in 1) the peaks and valleys from the model output aligning closer to the observed peaks and valleys in the observations, and 2) a decrease in the absolute bias and an increase in correlation.

Shifting the model output also made it easier to qualitatively evaluate the accuracy of the modeled D_0. For example, the 4 min time shift present in Fig. 6.7b (CCN 100 cm^{-3}) shifted the spike associated with the leading convective region of the QLCS from the model output to the

spike in the observations, but the overall maxima and minima throughout the trailing stratiform region were not captured in the model output except from 1945–1955 UTC and the model output D_0 was still approximately 1 mm underpredicted. In Fig. 6.7f (CCN 1,000 cm $^{-3}$), the mean modeled D_0 was within approximately 0.5 mm of the observations throughout the trailing stratiform region. The different model shifts aligned the initial spike in modeled D_0 to the observed D_0 and helped align the maxima and minima in D_0 throughout the time series. The overall trend in D_0 of a subtle increase throughout the trailing stratiform region is still evident and the intermediate simulations align closer to the observations.

At PIPS2A, the benefit of the shift in model output is still present with the onset of higher D_0, but the model output is now more correlated with the maxima and minima throughout the trailing stratiform region of the QLCS in the observed D_0. For example, in the shifted CCN 100 cm^{-3} time series (Fig. 6.8b), the initial spike in D_0 is captured by the model but is still underpredicted. However, the secondary peak (~2055 UTC) and the decrease from the peak from (2100–2140 UTC) now aligns close to observations. The final peak in D_0 is not observed at 2140 UTC as a convective core passed over PIPS2A. The remaining CCN concentration experiments of CCN 500 (Fig. 6.7d), 1,000 (Fig. 6.7f), 1,5000 (Fig. 6.7h), and 2,000 cm^{-3} (Fig. 6.7j) better accord with the initial peaks in D_0 at 2040–2055 UTC and the peak at 2140 UTC. However, the higher CCN concentrations still overpredict the D_0 in the trailing stratiform region for the shifted model output. For all PIPS including those not discussed, the correlation increased, and the absolute bias decreased for the shift of model output. A further evaluation of the unshifted and shifted statistics for D_0 will be evaluated in the next section.

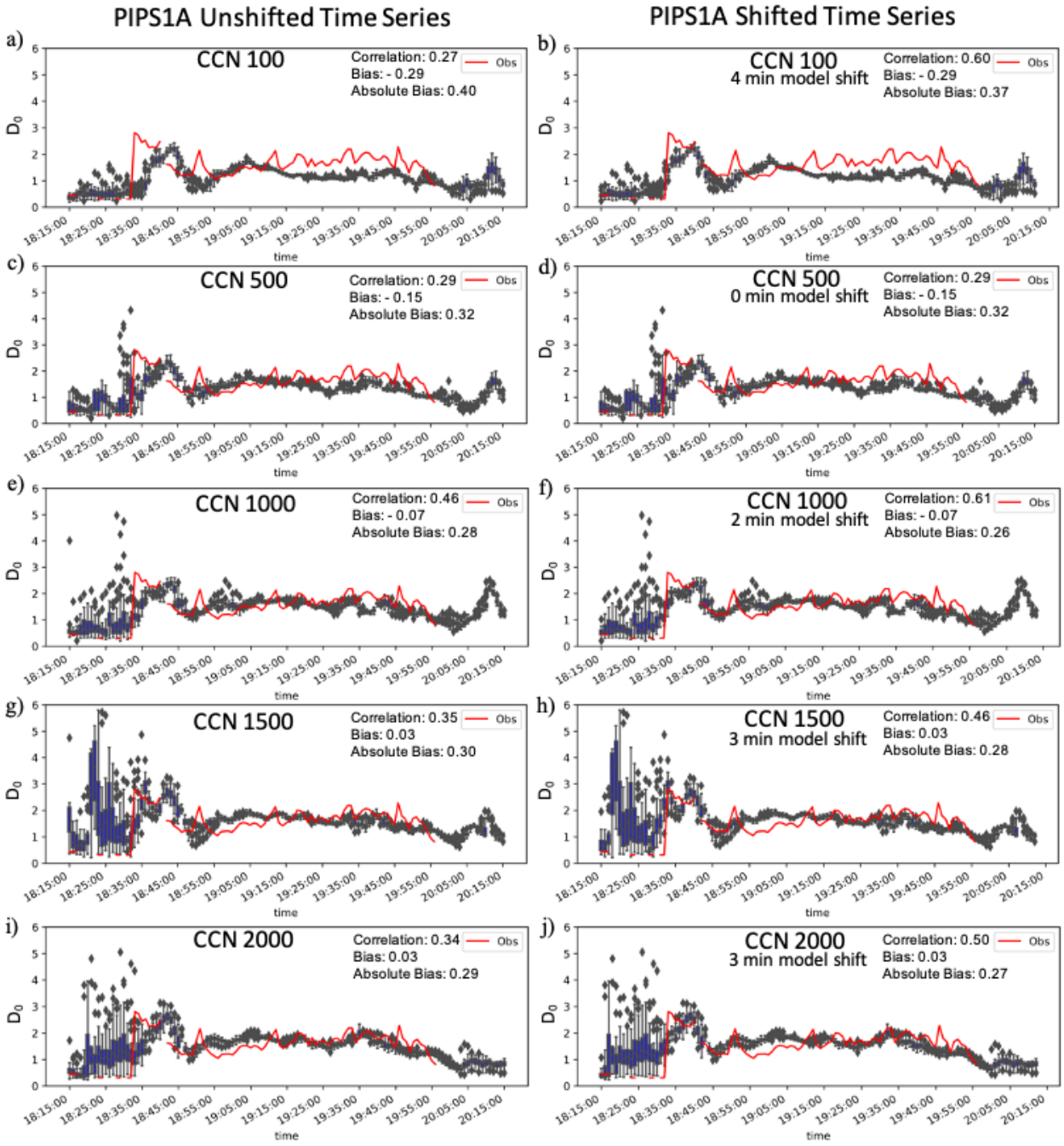

Figure 6-7. The ensemble member spread of D_0 (mm) (blue box plots) and observed D_0 (red line) from PIPS1A for the CCN concentrations of 100 cm^{-3}, 500 cm^{-3}, 1,000 cm^{-3}, 1,500 cm^{-3}, and 2,000 cm^{-3} for the unshifted 1-km experiment time series (left) and model shifted time series (right). The duration of the shift for each CCN concentration is listed on their respective panel.

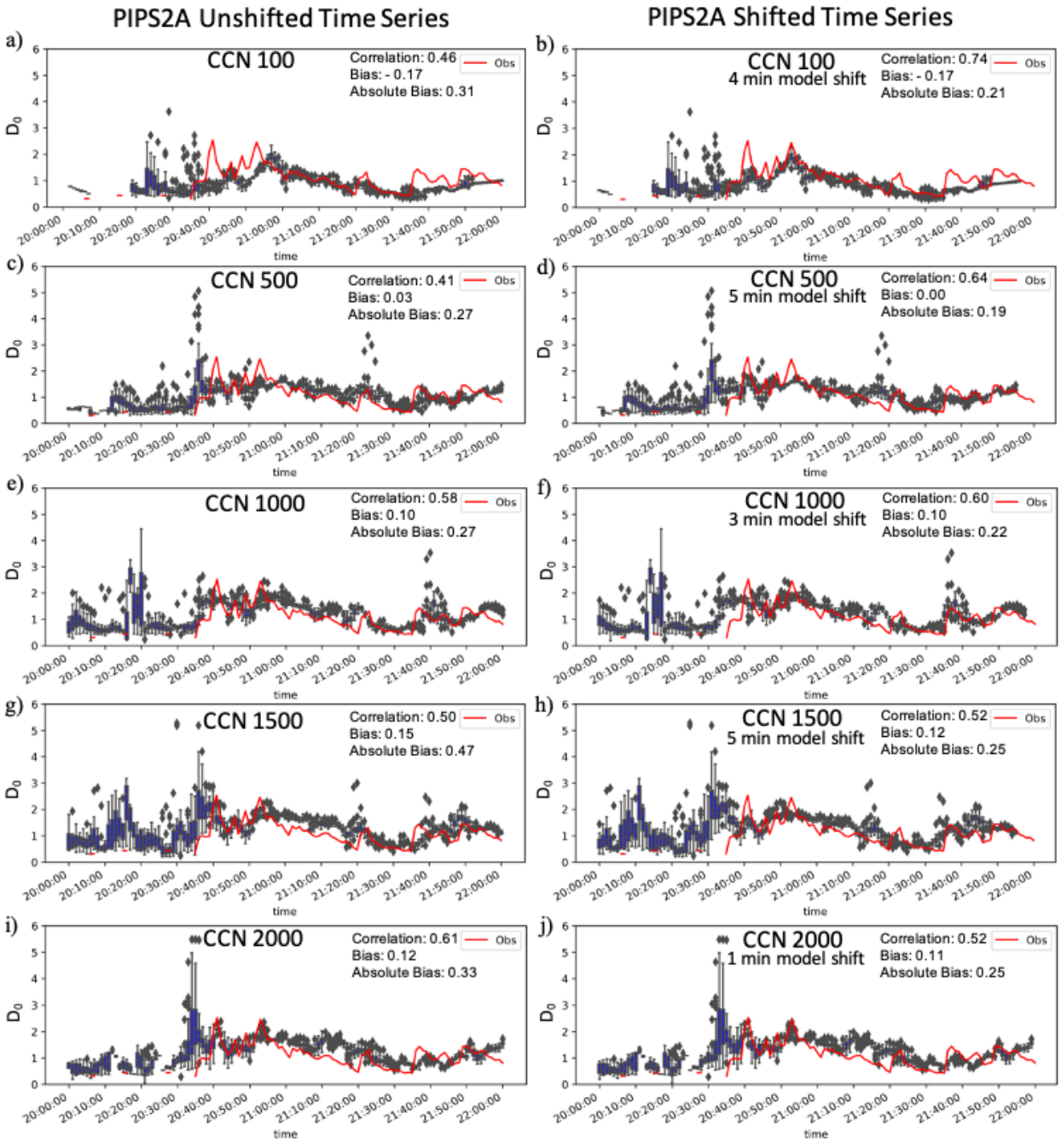

Figure 6-8. As in Fig. 6.7, but for PIPS2A.

6.3.3 Statistical D_0 comparisons

As described in section 5.2.3, the bias, absolute bias, and correlation were calculated for each PIPS across all CCN concentration experiments. The unshifted D_0 bias (Fig. 6.9a) reveals a negative to increasingly positive bias as the CCN concentration increases across all PIPS locations. The shifted D_0 (Fig. 6.9b) bias demonstrates a similar trend, but the shifted biases are of lesser magnitude than the unshifted D_0 biases. The combined unshifted and shifted D_0 biases (Fig. 6.9c) show the shift of a negative to increasingly positive bias. This trend in bias accords well with previous results since the lower (higher) CCN concentrations underpredict (overpredict) D_0 as cold rain processes dominate for the higher CCN concentrations resulting in larger drops. Overall, the unshifted and shifted intermediate CCN concentrations (close to CCN 1,000 cm^{-3}) have the lowest bias for D_0.

The absolute bias for D_0 revealed similar results (Fig. 6.9d–f). A minimum in absolute bias for D_0 exists across all PIPS locations for CCN 750–1,000 cm^{-3}. The same trend is true for the shifted D_0 absolute bias with the lower and higher CCN concentrations having a larger absolute bias than the intermediate CCN concentration simulations. The combined D_0 absolute bias for the unshifted model output agrees with the previous statement, however, the combined D_0 absolute bias for the shifted model output is highest for the CCN 100 cm^{-3} experiment before decreasing to approximately 0.20 mm for the CCN 300–1,000 cm^{-3} experiments. The shifted absolute bias increases for the CCN 1,000–1,250 cm^{-3} experiments. This result suggests the high end lower to intermediate CCN concentration experiments (CCN 300–1,000 cm^{-3}) better represent the observed D_0 than the higher CCN concentration experiments.

The correlation for the unshifted D_0 (Fig. 6.9g) across all PIPS locations for the varying CCN concentrations reveals a maximum in correlation for CCN 1,000 cm^{-3}. The correlation

increases for the shifted model output across all of the PIPS for the different CCN concentrations (Fig. 6.9h), as visible in the combined correlation (Fig. 6.9i). The combined correlations are above 0.85 and statistically significant (p-value < α for $\alpha = 0.05$) or each of the CCN concentrations. No statistically significant trend is present for the combined shifted D_0 correlation (p-value < α).

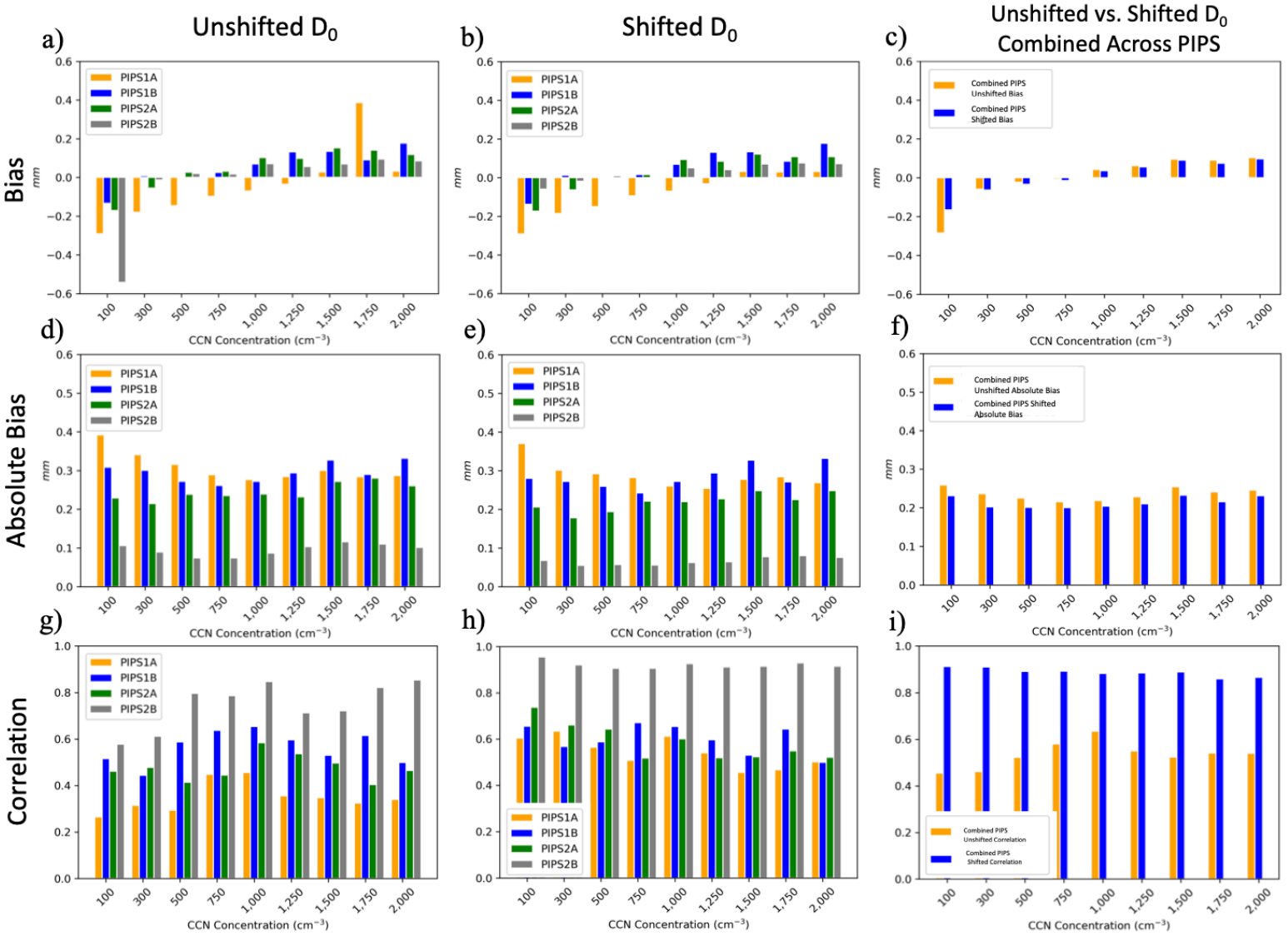

Figure 6-9. The bias, absolute bias, and correlation (horizontal) for D_0 (mm) for the unshifted model output, shifted model output, and combined unshifted and shifted statistics for all PIPS locations (vertical).

6.3.4 Unshifted Z comparisons

The lowest level of Z from the model output was compared with the derived observed Z from the PIPS data as described in section 5.2.2. Quantitative comparisons of the model output Z and Z_{DR} with lowest level radar data from local WSR-88Ds are planned as future work. Z is influenced by the size and quantity of the hydrometeors. A couple of large hydrometeors can result in a greater Z than a greater quantity of small hydrometeors though the total water content could be the same. Fig. 6.10 and Fig. 6.11 compare the calculated observed Z at the respective PIPS location with the model output at 1-min intervals.

The time delay observed for the D_0 plots are observed in Z. Lower CCN concentration simulations are delayed more with the onset of precipitation and different maxima and minima throughout the time series than the higher CCN concentration experiments. For example, in Fig. 6.10a, the onset of precipitation is offset by approximately 4 min. Later in the time series, the peak in Z from 1925–1940 UTC in the observations was delayed until 1930–1945 UTC in the model resulting in a 15–20 dBZ difference during this timeframe (Fig. 6.10a). The intermediate and higher CCN concentration experiments (Fig. 6.10b–i) are faster than the CCN 100 cm^{-3} experiment. However, the frequency of spurious showers ahead of the QLCS increases as CCN concentration increases as described when analyzing D_0 (Fig. 6.10).

The reflectivities for most ensemble members are less than 10 dBZ as indicated by the blue boxes at each minute indicating only several members have showers present ahead of the QLCS as the CCN concentration increases. The initial peak in Z is underpredicted across all experiments. The lower CCN concentration experiments have a tighter cluster with reflectivities closer to the observed magnitude than the higher CCN concentration experiments where the range in ensemble

member Z for the initial convective region of the QLCS is a larger range and lesser in magnitude. Z throughout the trailing stratiform region for all the experiments shown in Fig. 6.10 accords well with observations, with the intermediate and higher CCN concentration experiments capturing the secondary peak better. The absolute bias is largest in magnitude for the CCN 100 cm^{-3} because of the delay in the onset of precipitation and the large difference in the observed and modeled Z from 1925–140 UTC. For PIPS1A, the intermediate and higher CCN concentration simulations better represent the observed Z.

The spurious showers resulted in Z values in the model output that were not observed ahead of the QLCS are significantly reduced for the PIPS2A location (Fig. 6.11f–i). Showers were still present ahead of the QLCS at this time (Fig. 6.4) but may have not passed over the grid point of PIPS2A and therefore are not in some of the time series shown (Fig. 6.11). The timing for PIPS2A is better across the CCN concentration experiments with the onset of precipitation (Fig. 6.11) than PIPS1A (Fig. 6.10). The initial peak in magnitude of Z is not as well modeled for the lower CCN concentrations for PIPS2A and underpredicts the initial peak near 2040 UTC by 15–25 dBZ (Fig. 6.11a–c). For the intermediate and higher CCN concentration experiments, the initial peak is only underpredicted by 10–15 dBZ. Additionally, the secondary surge of showers that passed over PIPS2A from 2135–2200 UTC was underpredicted or delayed across all CCN concentration experiments. The timing of the model output aligned closer to the observations for the CCN 1,000–1,500 cm^{-3} experiments but was still lower than the observed D_0 for this time frame. The CCN concentrations shown in Fig. 6.11 have a trailing stratiform region from 2055–2115 UTC close to the observed calculated Z. The observed lull in precipitation was captured by all the experiments from approximately 2130–2135 UTC.

The different CCN concentrations diverge on how they handled the convective cores passing over PIPS2A from 2140–2200 UTC. The lowest (CCN 100 cm^{-3}) and highest (CCN 2,000 cm^{-3}) CCN concentrations significantly underpredict the Z during this time. The experiments with CCN concentrations of 750–1,750 cm^{-3} reveal two peaks in Z from approximately 2140–2200 UTC but are off with the timing. The difference in magnitude varies between the CCN concentrations at this time, but overall the intermediate simulations better capture the magnitude and timing of the passing of these convective cores from 2140–2200 UTC. The correlation is above 0.79 for all CCN concentrations for PIPS2A. The two PIPS not discussed (PIPS1B and PIPS2B) support the intermediate to higher CCN concentrations being more representative of the observed Z as discussed in section 6.3.6.

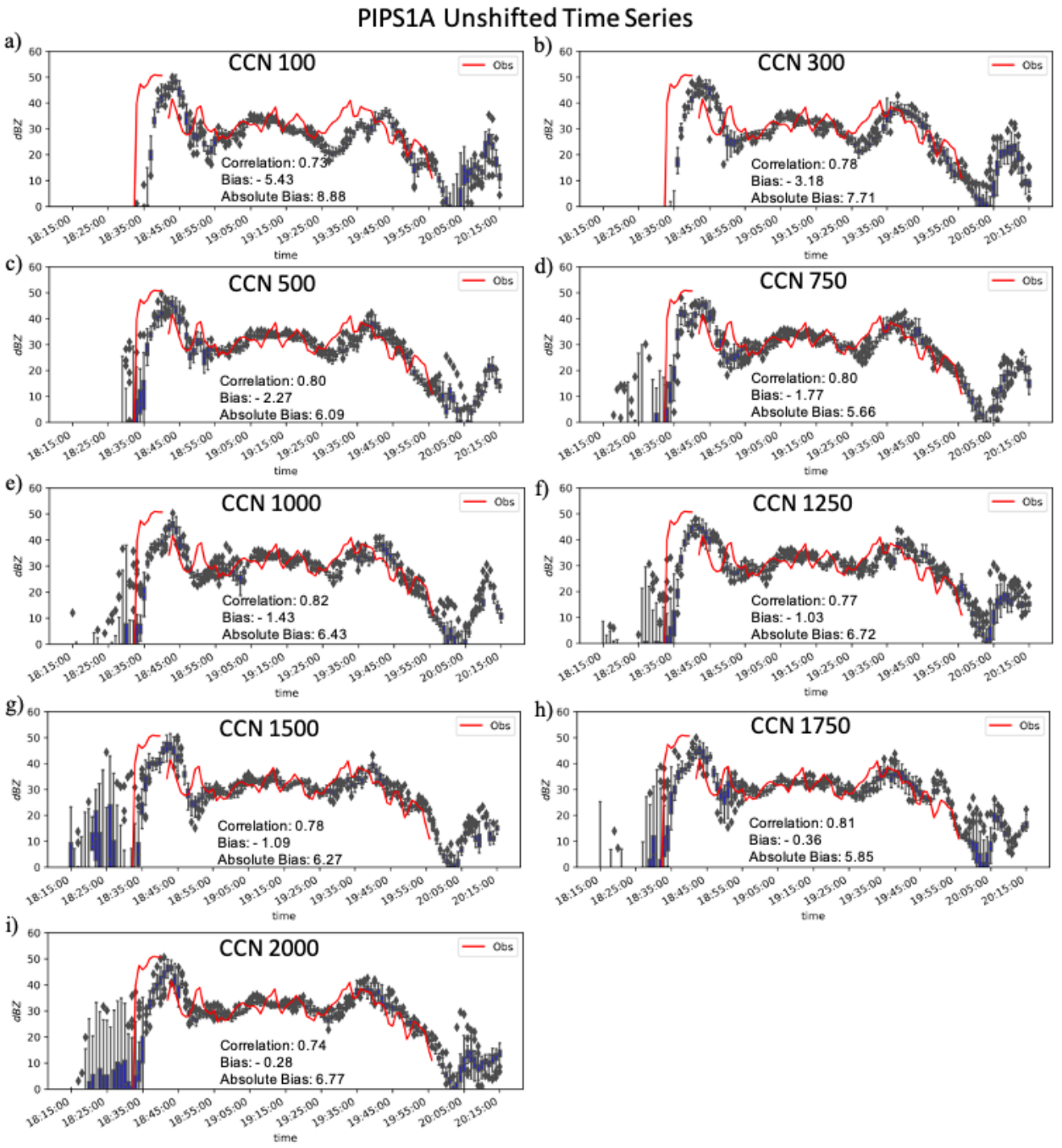

Figure 6-10. The unshifted ensemble member spread of Z (dBZ) (blue box plots) and observed Z (red line) for PIPS1A for the following CCN concentration 1-km experiments in units of cm^{-3}: (a) 100, (b) 300, (c) 500; (d) 750, (e) 1,000, (f) 1,250, (g) 1,500, (h) 1,750, and (i) 2,000.

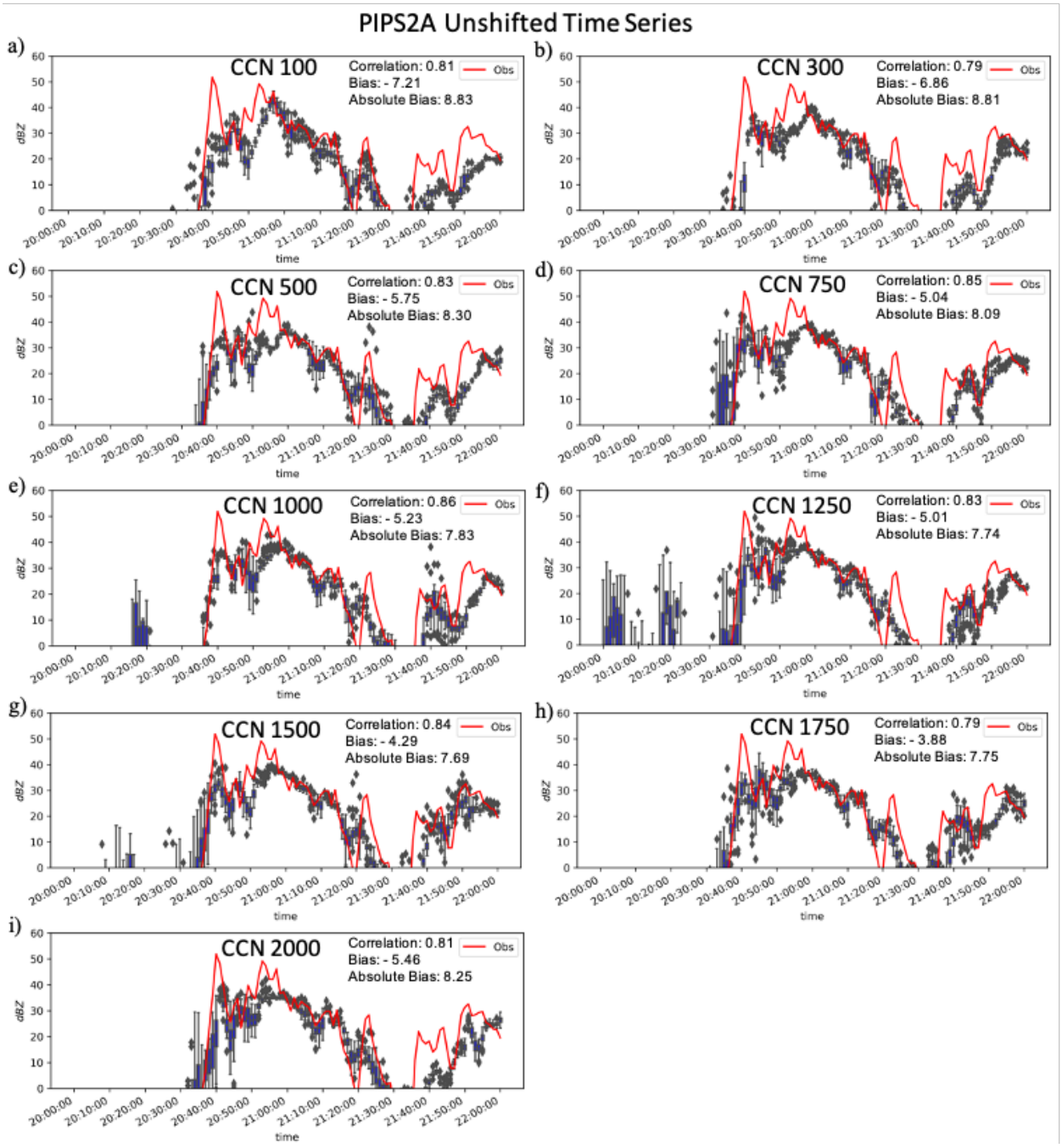

Figure 6-11. As in Fig. 6.10, but for PIPS2A.

6.3.5 Shifted Z comparisons

Z time series were shifted as described for D_0 in section 6.3.2. The time series for the lowest CCN concentration (CCN 100 cm^3) were shifted 4 min for PIPS1A (Fig. 6.12a) and 2 min for PIPS2A (Fig. 6.13a), the largest shift of any of the CCN concentrations for the respective PIPS locations. The spikes in Z associated with the showers ahead of the QLCS are not in the CCN 100 cm^{-3} experiment but are observed for the intermediate and higher CCN concentration experiments (Fig. 6.12, 6.13). The shift of the model output in the time series for Z for the PIPS1A time series aligns with the onset of precipitation in the respective experiments with the onset of observed precipitation (Fig. 6.12a, d, f, h, j). The initial peak in magnitude of Z associated with the leading convective region of the QLCS aligns better with observations across the lower CCN concentrations (Fig. 6.12a, c). The intermediate and higher CCN concentrations underpredict the initial peak in Z by an average of 5–10 dBZ with only a few ensemble members approaching the calculated observed Z at PIPS1A (as indicated by the outliers in the box plots in Fig. 6.12f, h, j). This is also present across PIPS1B and PIPS2B (not shown).

The discrepancies between the model output and calculated observed Z for the lower CCN concentrations arise during the trailing stratiform region for the lower CCN concentration simulations for PIPS1A (Fig. 6.12b). Z is underpredicted as was D_0 for the lower CCN concentrations because of warm rain processes resulting in smaller drops than if cold rain processes were dominating. The warm rain processes result in the lower reflectivities (Fig. 6.12b). Z increases as the CCN concentration increases in the trailing stratiform region (Fig. 6.12). Overall, the calculated observed Z falls within the spread of the model output for the ensemble Z across the intermediate and higher CCN concentration experiments (Fig. 6.12d, f, h, j). The timing of the local maxima and minima in the model output now accords better with the calculated

observed Z . For example, the peak in Z from 1925–1945 UTC in the CCN 1,000 cm^{-3} unshifted model output lags the calculated observed Z by up to 3 min (Fig. 6.12e). Shifting the model output removes this delay and better displays the alignment between the model output and observed Z . The statistics also improve (absolute bias and correlation) for the shifted model output. Similar examples can be made for the other CCN concentration experiments shown in Fig. 6.12.

Z time series for PIPS2A across the CCN concentration experiments did not require as much of a shift as PIPS1A, PIPS1B, and PIPS2B (Fig. 6.13). The lower CCN concentrations were shifted only 1-2 min (Fig. 6.13b, d) while the intermediate CCN concentrations required no shift at all (Fig. 6.13f, h). The CCN 2,000 cm^{-3} experiment required a shift of only 1 min (Fig. 6.13j). The experiments where the time series was shifted resulted in lower absolute bias and higher correlation. The same general statements can be made of the unshifted Z plots for PIPS2A in section 6.3.4. The unshifted time series for the CCN concentrations of 1,500 cm^{-3} (Fig. 6.13h) and 1,250 cm^{-3} (not shown) accord best with the calculated observed Z. As discussed for D_0, the CCN concentration experiments where there was a shift resulted in better accordance of the model output to the observations. The intermediate CCN concentrations still appear to best align overall with the observed Z.

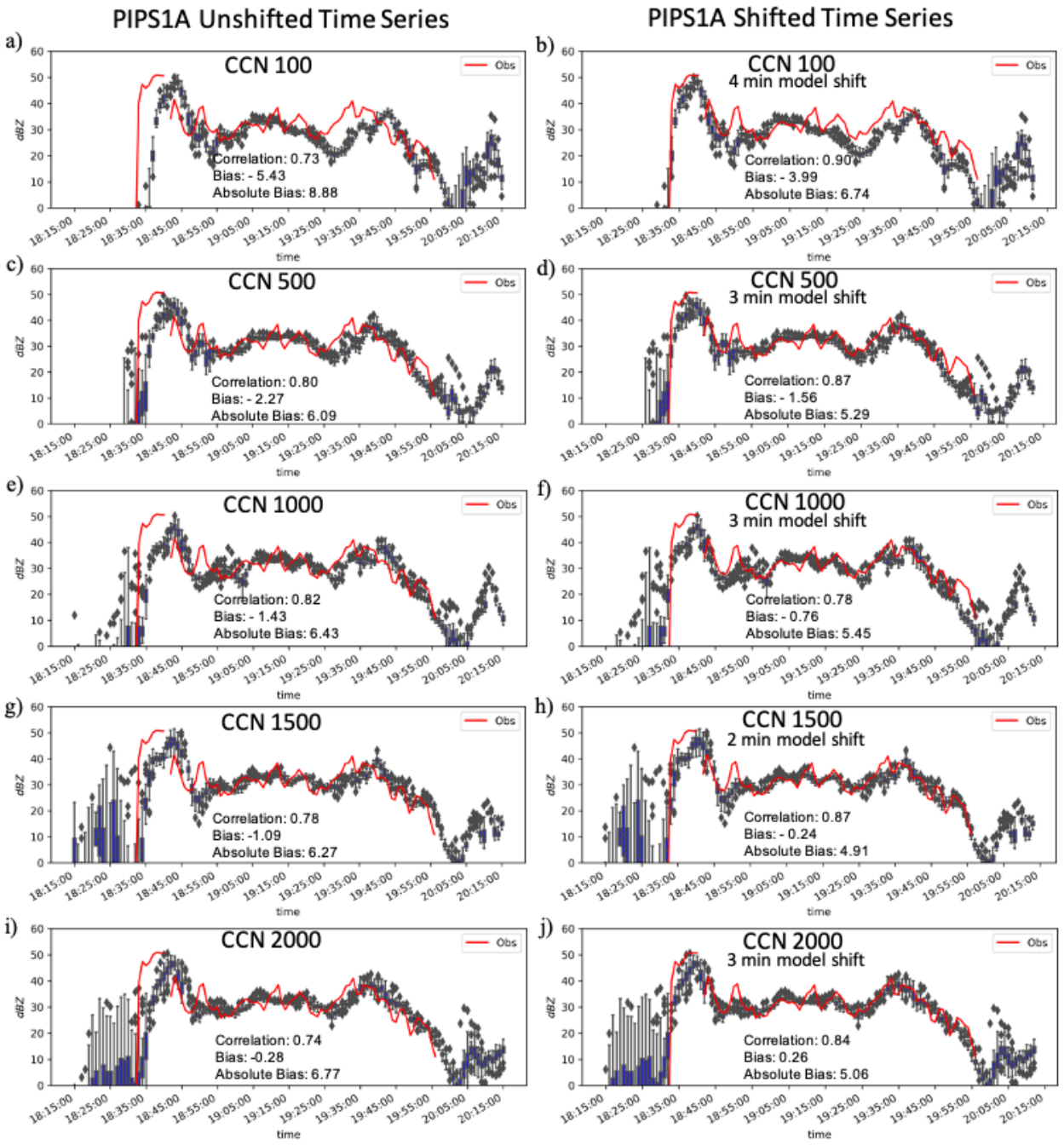

Figure 6-12. The ensemble member spread of Z (dBZ) (blue box plots) and observed Z (red line) from PIPS1A for the CCN concentrations of 100 cm^{-3}, 500 cm^{-3}, 1,000 cm^{-3}, 1,500 cm^{-3}, and 2,000 cm^{-3} for the unshifted 1-km experiment time series (left) and model shifted time series (right). The duration of the shift for each CCN concentration is listed on their respective panel.

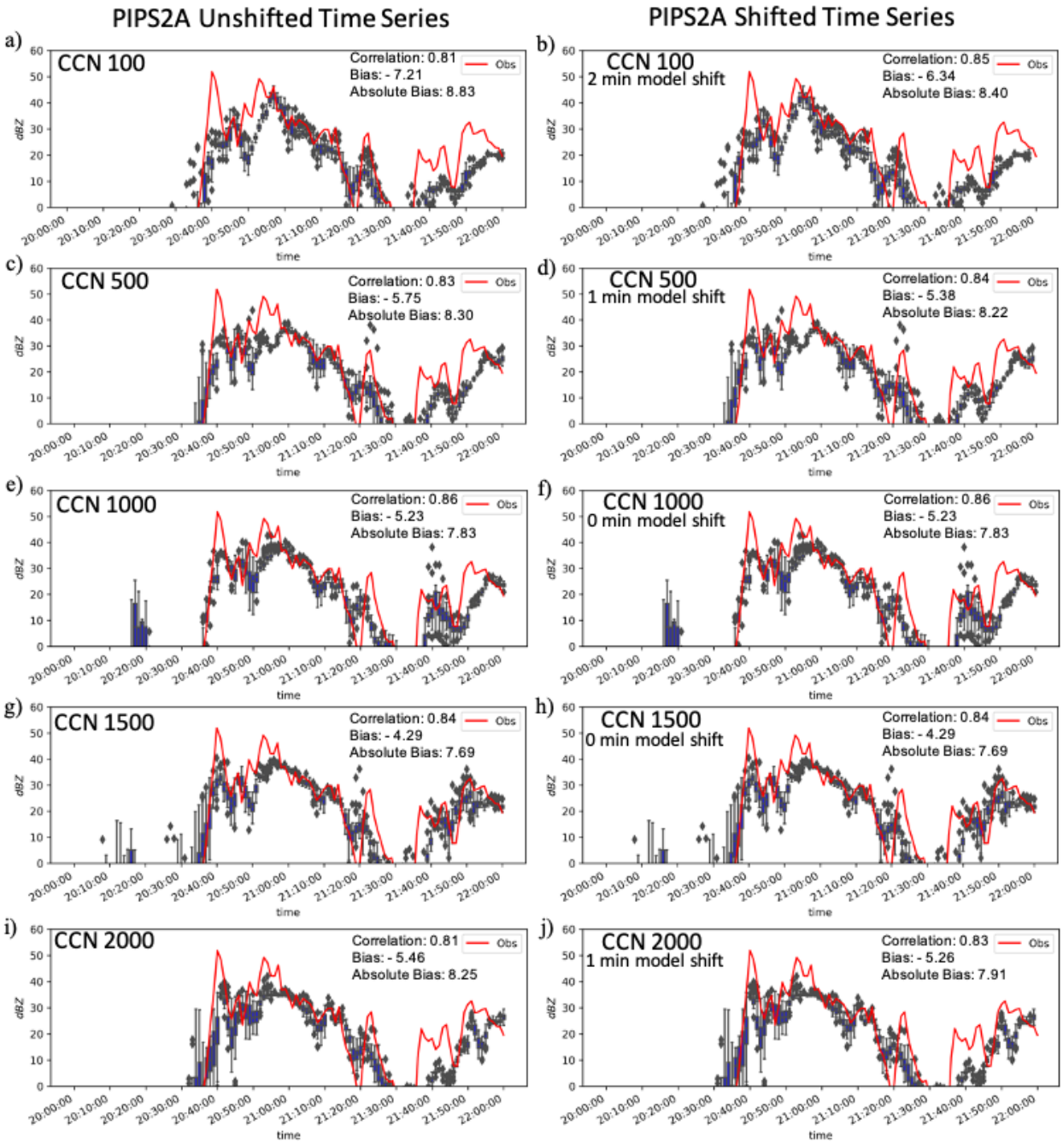

Figure 6-13. As in Fig. 6.12, but for PIPS2A.

6.3.6 Statistical Z comparisons

The bias, absolute bias, and correlation were also calculated for Z. Unlike the bias for D_0 where there was a trend of a negative to increasingly positive bias, the bias for Z was negative for all CCN concentrations with the bias becoming less negative as the CCN concentration increases (Fig. 6.14a–c). The CCN 100 cm^{-3} experiment had the largest bias across each of the PIPS locations in both the unshifted (Fig. 6.14a) and shifted statistics (Fig. 6.14b). The combined bias for Z remains nearly constant for the intermediate and higher CCN concentrations (Fig. 6.14c). The larger bias for the lower CCN concentration experiments accords with Fig. 6.13 since the model output consistently underpredicting Z throughout the trailing stratiform region. Since the bias is negative for the CCN concentrations across all PIPS locations but the CCN concentrations of 1,250 cm^{-3} and 2,000 cm^{-3} for PIPS1B (Fig. 6.14a), the trends in absolute bias are similar to the bias (Fig. 6.14d–f).

The correlation for PIPS1A, PIPS1B, and PIPS2A were above 0.70 before shifting the model output (Fig. 6.14g), which indicates ARPS-EnKF coupled with the NSSL-TM microphysics scheme adequately simulates the observed Z over these PIPS locations. PIPS2B is lower because of the differences in timing between the model output Z and calculated observed Z (Fig. 6.14g). However, the shifted model output has a correlation above 0.80 which is statistically significant across all of PIPS for each of the CCN concentration experiments (Fig. 6.14h). The high correlation between the lowest level model output Z and Z calculated at the PIPS location agrees with previous studies of model output Z best aligning with observations closer to the ground due to liquid phase particles dominating (Tao et al. 2012). No statistically significant trend exists in the correlation of the different CCN concentrations.

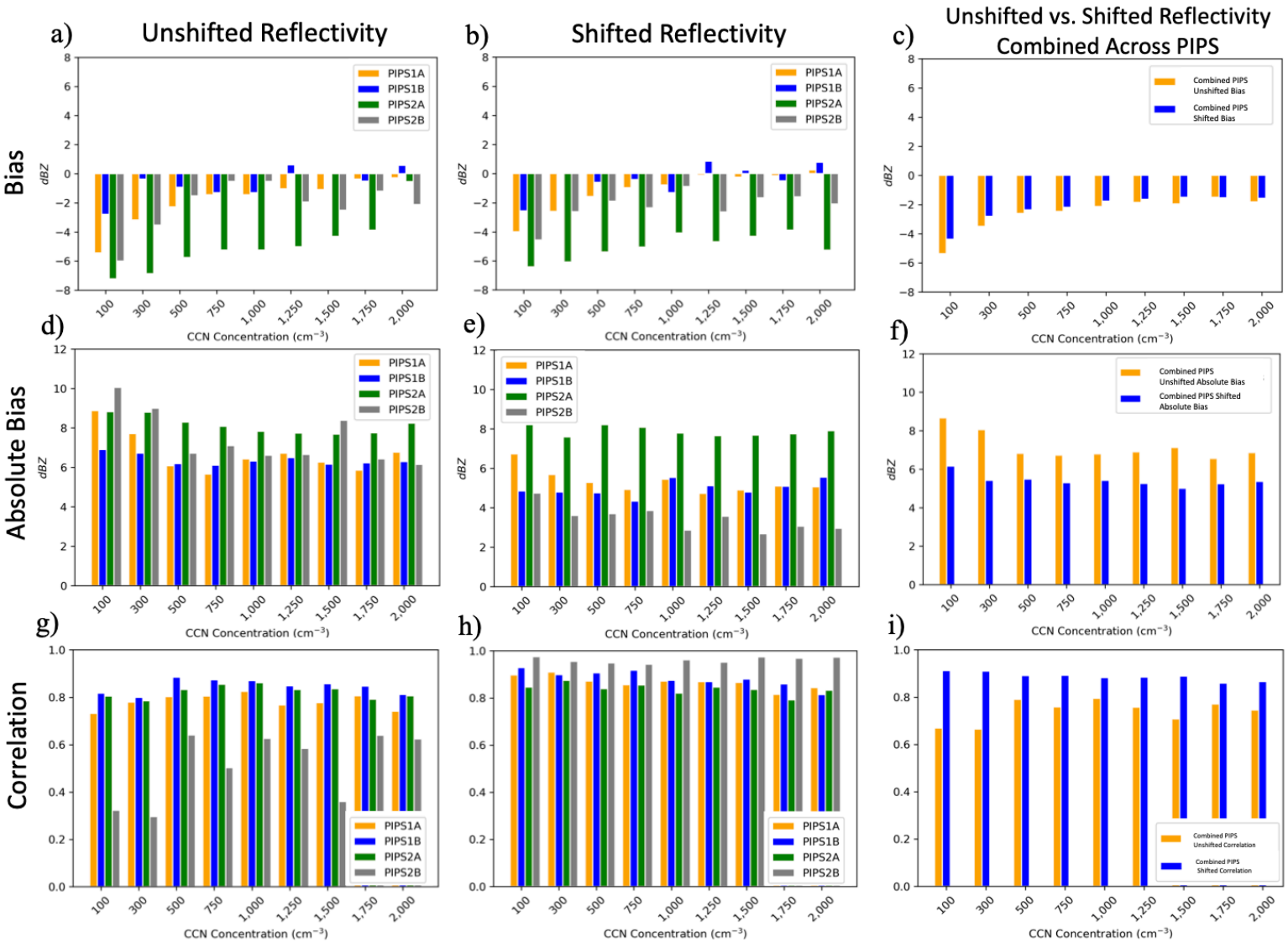

Figure 6-14. The bias, absolute bias, and correlation (horizontal) for Z (dBZ) for the unshifted model output, shifted model output, and combined unshifted and shifted statistics for all PIPS (vertical).

6.3.7 Unshifted Z_{DR} comparisons

Z_{DR} is the logarithmic ratio of the horizontally polarized reflectivity (Z_H) to the vertically polarized reflectivity (Z_V) (American Meteorological Society 2020). Positive values represent hydrometeors that are larger in the horizontal than the vertical, with larger positive values of Z_{DR} (3–6 dB) associated with larger rain drops. Values near zero represent hydrometeors approximately the same size in the horizontal and vertical. Z_{DR} is beneficial in discriminating large rain drops (large positive Z_{DR}) from hail (Z_{DR} near zero). Lower values of Z_{DR} (1–3 dB) are associated with smaller rain drops. Given this relationship, similar results are found for Z_{DR} and D_0.

The calculated observed Z_{DR} (Fig. 6.15; Fig. 6.16) has more fluctuations than the observed D_0 or calculated Z. As CCN concentration increases, Z_{DR} increases for the showers ahead of the QLCS, which is the same trend observed with D_0 or Z. Z_{DR} is 3–5 dB for the showers in some ensemble members ahead of the QLCS for the experiments with CCN concentrations above 1,250 cm^{-3} (Fig. 6.15; Fig. 6.16) indicating the presence of large drops which is confirmed by the D_0 time series for the same time (Fig. 6.5; Fig. 6.6). The spread of Z_{DR} for ensemble members is large for the intermediate and higher CCN concentrations ahead of the onset of observed precipitation for PIPS1A (Fig. 6.15d–i) and the CCN 1,000–1,500 cm^{-3} experiments for PIPS2A. The CCN 1,750 cm^{-3} and 2,000 cm^{-3} at PIPS2A did not have showers pass over the PIPS location, but showers were present ahead of the QLCS in some ensemble members as discussed in section 6.3.4.

The onset of precipitation and subsequent increase in Z_{DR} is better timed across the intermediate and higher CCN concentration experiments for PIPS1A. The magnitude of the initial peak in Z_{DR} is close to the observed peak, but the model is delayed by 3–5 min (Fig. 6.15a–b). A trend exists across all PIPS including PIPS1A (Fig. 6.15) and PIPS2A (Fig. 6.16) of Z_{DR} increasing as the CCN concentration increases, which supports cold rain processes dominating in higher CCN

concentrations. However, Z_{DR} is overpredicted throughout the trailing stratiform region from approximately 1855–1915 UTC in all experiments for PIPS1A in Fig. 6.15. Higher CCN concentrations result in more smaller cloud droplets, leading to more dominant cold rain processes (i.e. riming and enhanced freezing) that in turn lead to higher Z_{DR} for the resulting rain DSDs derived from the melting ice hydrometeors (Tao et al. 2012). The maxima in Z_{DR} near 1930 UTC and subsequent decrease is better captured by the intermediate and higher CCN concentrations than the lower CCN concentrations.

For PIPS2A, the initial peak in Z_{DR} was not in the ensemble member output for the lower CCN concentrations. The peak was present for the intermediate and higher CCN concentrations; however, the timing of the model output was ahead of the observations. This peak in the intermediate and higher CCN concentrations is not from the onset of precipitation associated with the passage of the QLCS, but instead the showers present in some ensemble members with large rain drops (Fig. 6.16d–i). The onset of precipitation from the QLCS at the different PIPS was behind (not ahead) as previously discussed. The same trend of Z_{DR} increasing as CCN concentration increases is found for PIPS2A (Fig. 6.16). The intermediate and higher CCN concentration experiments better accord with the calculated observed Z_{DR} in the trailing stratiform region from 2045–2055 UTC, but the lower CCN concentrations align with the calculated observed Z_{DR} from 2100–2130 UTC. The intermediate and higher CCN concentrations overestimate the Z_{DR} from 2100–2130 UTC. In summary, the model output Z_{DR} does not align with the calculated observed Z_{DR} continuously for any of the CCN concentrations. There are points in the time series of the CCN concentrations where different concentrations align better with observations than others, but no range of CCN concentrations is superior over the others as indicated by the statistics in Fig. 6.15 and Fig. 6.16.

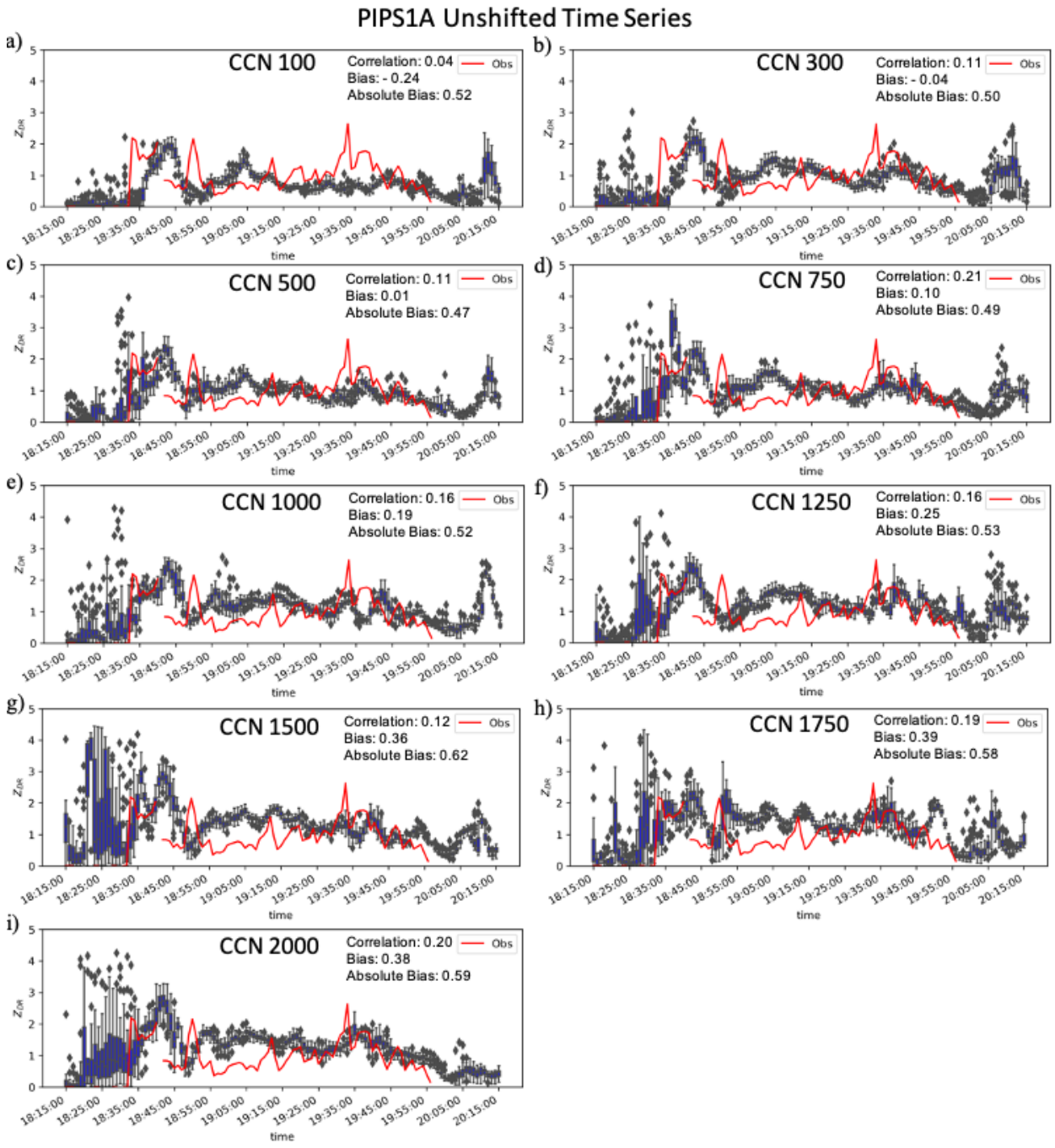

Figure 6-15. The unshifted ensemble member spread of Z_{DR} (dB) (blue box plots) and observed Z_{DR} (red line) for PIPS1A for the following CCN concentration 1-km experiments in units of cm^{-3}: (a) 100, (b) 300, (c) 500; (d) 750, (e) 1,000, (f) 1,250, (g) 1,500, (h) 1,750, and (i) 2,000.

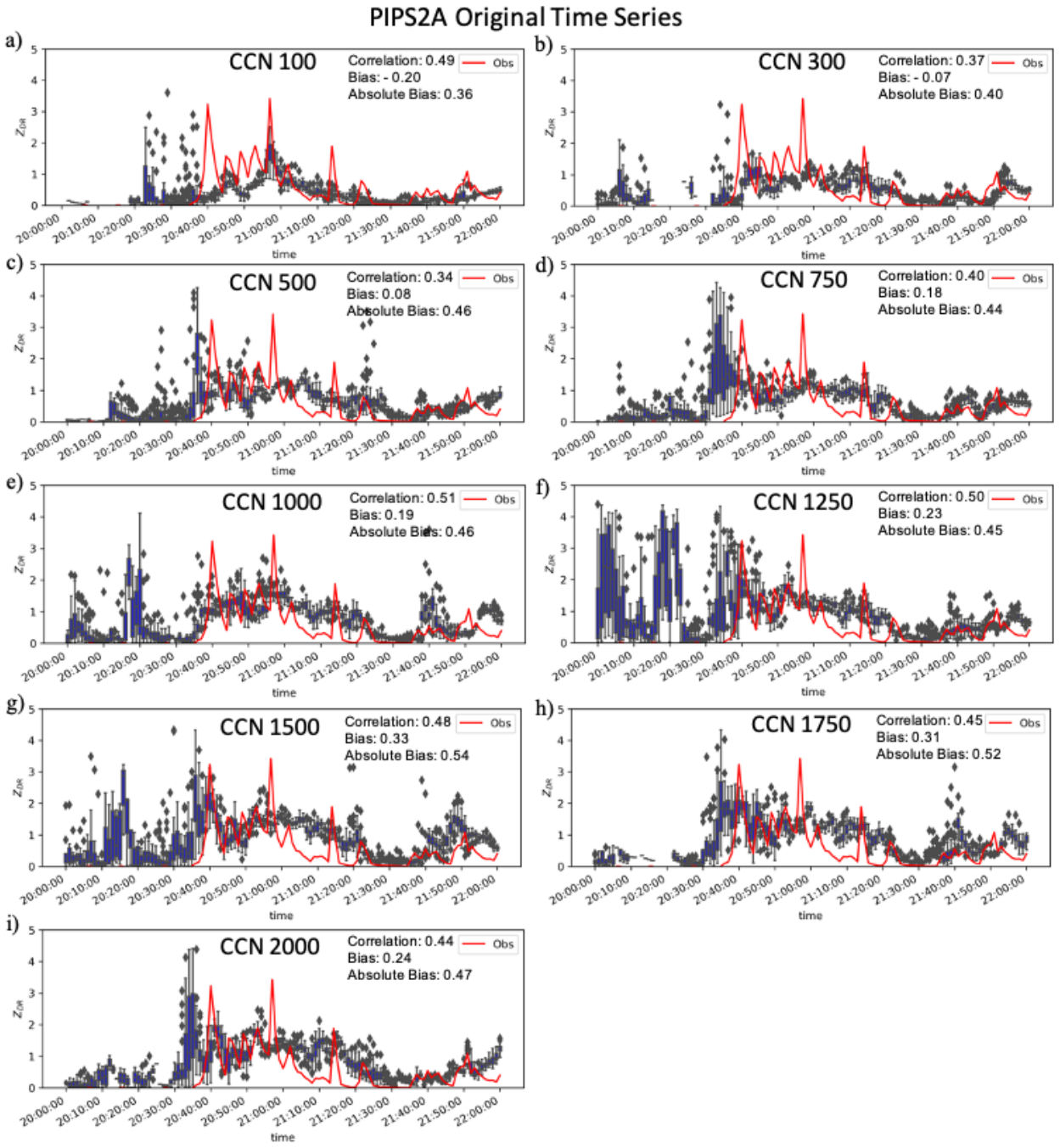

Figure 6-16. As in Fig. 6.15, but for PIPS2A.

6.3.8 Shifted Z_{DR} comparisons

When shifting the model output to the onset of precipitation, the trend of increasing Z_{DR} as the CCN concentration increases holds true. The magnitude of the initial peak in Z_{DR} of the lower and intermediate CCN concentration experiments aligns closer to the calculated observed Z_{DR} for PIPS1A (Fig. 6.17b–f). The shifted higher CCN concentrations overpredict the initial peak of Z_{DR} in the leading convective region as well as throughout the trailing stratiform region from 1855–1930 UTC. The absolute bias is the lowest for the CCN 1,000 cm^{-3} experiment. The shifted lower and higher CCN concentration simulations still underpredict and overpredict Z_{DR} by 1–2 dB at times (Fig. 6.17b, h, j). For the shifted PIPS2A time series (Fig. 6.18), the initial peaks in Z_{DR} associated with the onset of precipitation in the leading convective region align closer to the observed calculated Z_{DR} for the intermediate and higher CCN concentrations (Fig. 6.18f, h, j). However, the CCN 100 cm^{-3} experiment accords well with the low Z_{DR} observed during the trailing stratiform region from 2100–2200 UTC. The intermediate and higher CCN concentration experiments overpredict the Z_{DR} by 1–2 dB during this time. This is indicated in the absolute bias for PIPS2A by the CCN 100 cm^3 experiment having the lowest absolute bias. None of the CCN concentrations continuously represent the calculated observed Z_{DR} for any of the PIPS locations including those not shown (PIPS1B and PIPS2B). The increasing magnitude of Z_{DR} as the CCN concentration increases is an important takeaway.

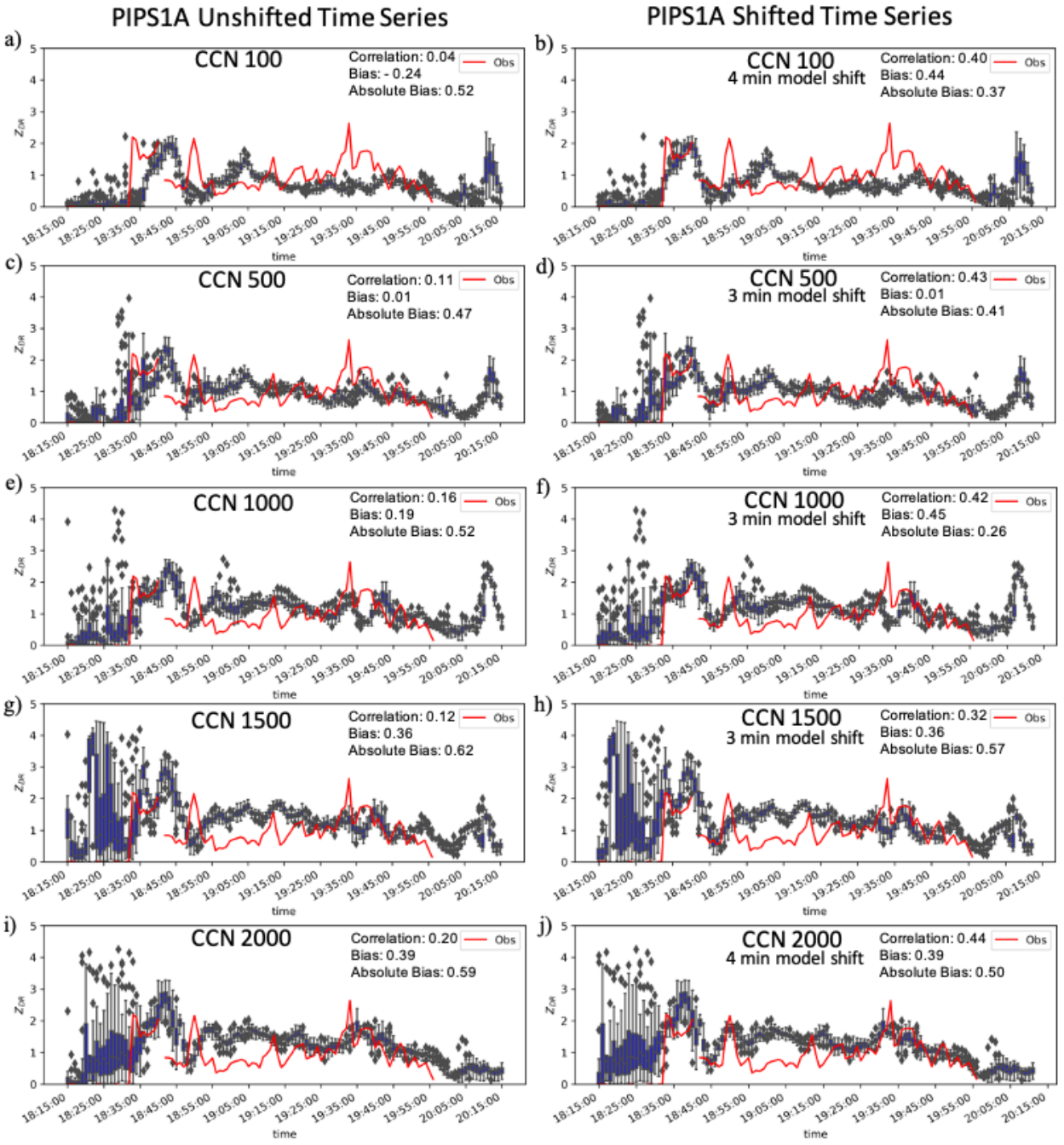

Figure 6-17. The ensemble member spread of Z_{DR} (dB) (blue box plots) and Z_{DR} observed (red line) from PIPS1A for the CCN concentrations of 100 cm^{-3}, 500 cm^{-3}, 1,000 cm^{-3}, 1,500 cm^{-3}, and 2,000 cm^{-3} for the unshifted 1-km experiment time series (left) and model shifted time series (right). The duration of the shift for each CCN concentration is listed on their respective panel.

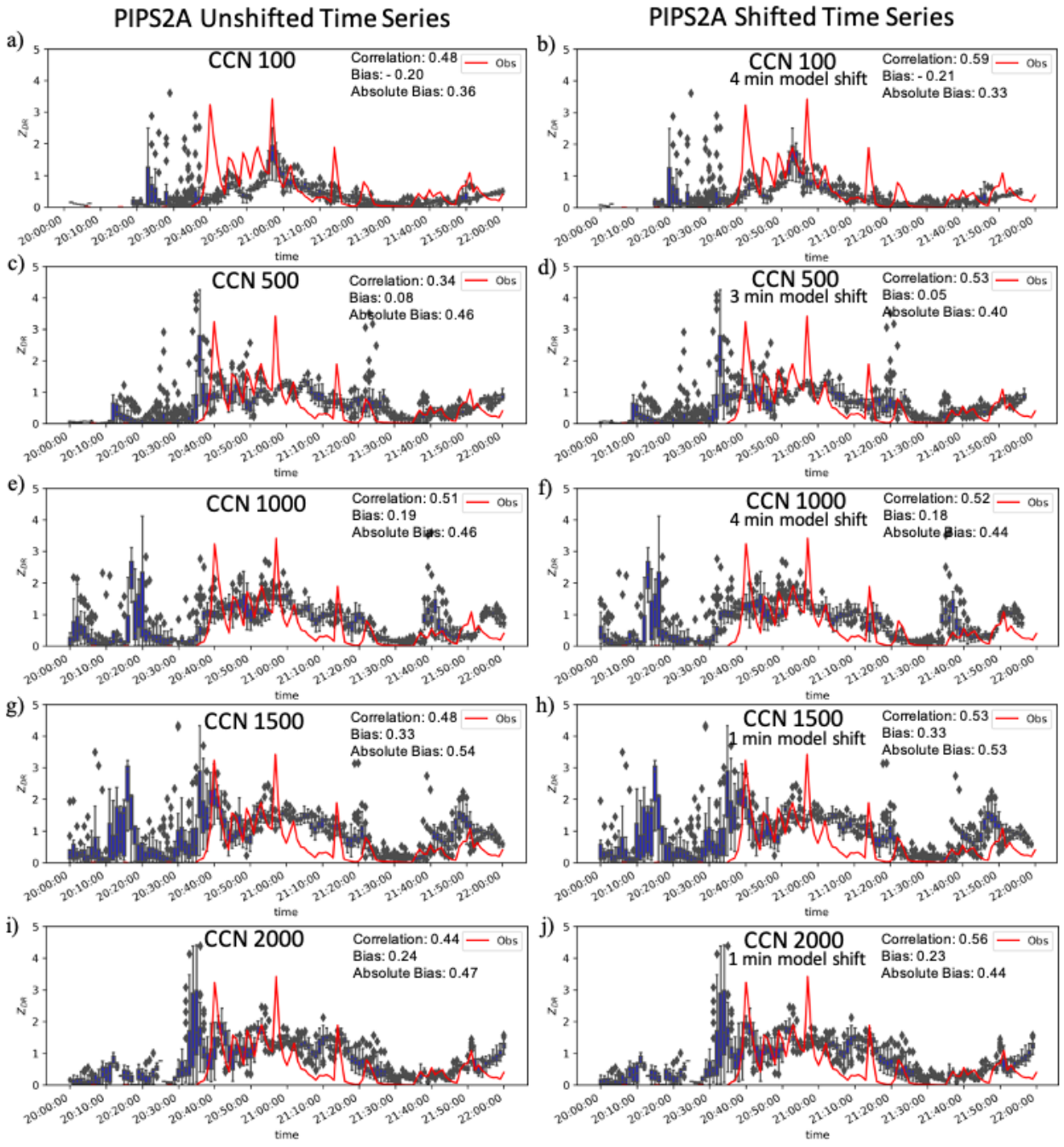

Figure 6-18. As in Fig. 6.17, but for PIPS2A.

6.3.9 Statistical Z_{DR} comparisons

The statistical trends for Z_{DR} are slightly different than those of D_0 and Z. The bias is negative for the lowest CCN concentrations and is increasingly positive as the CCN concentration increases which aligns with the bias for D_0 (Fig. 6.19). This aligns with the previous discussion since Z_{DR} is overpredicted across the intermediate and higher CCN simulations. The shifting of the model output lowers the bias by 0.1 dB across the CCN concentration experiments (Fig. 6.19c). The absolute bias is the lowest across for the CCN 100 cm^3 experiments before remaining constant for the CCN 300–1,000 cm^{-3} experiments (Fig. 6.19a). The absolute bias is the highest for CCN concentrations above 1,250 cm^3. The same statements can be made for the shifted Z_{DR} absolute bias (Fig. 6.19). The correlation is the lowest for Z_{DR} when compared to the correlation for D_0 and Z (Fig. 6.19) because of the sudden increases and decreases in the observations of Z_{DR} that were not well simulated. The combined correlation for the shifted statistics is better (~ 0.60) for each of the CCN concentrations.

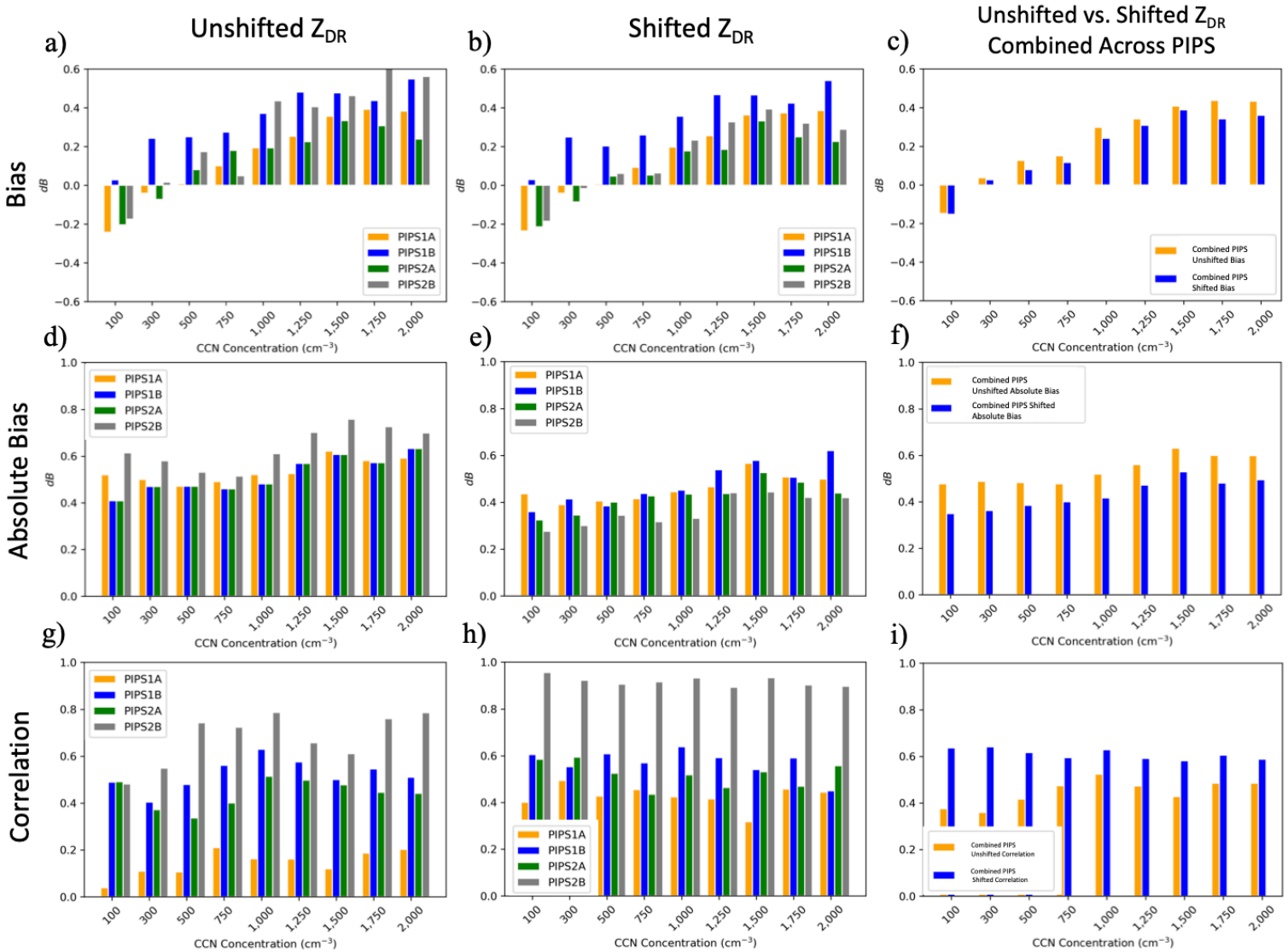

Figure 6-19. The bias, absolute bias, and correlation (horizontal) for Z_{DR} (dB) for the unshifted model output, shifted model output, and combined unshifted and shifted statistics across all PIPS locations (vertical).

6.4 1-km ARPS simulations to PIPS thermodynamic comparisons

To make additional comparisons between the CCN concentration experiments and observations, various thermodynamic variables were analyzed including θ, θ_e, and *w*. Model shifted time series are not discussed when analyzing θ, θ_e, and *w* for any of the CCN concentration experiments since the model output either consistently overpredicts or underpredicts the observed variable and shifting the model not significantly improving the statistics aside from the correlation.

Both θ and θ_e are evaluated since θ_e includes moisture and θ does not. The time series for θ at PIPS1A (Fig. 6.20) and PIPS2A (Fig. 6.21) both reveal the same result; all CCN concentration experiments have a warm bias in θ. This warm bias does not arise until the passage of the gust front and the associated decrease in temperature. Therefore, the warm bias is not an issue with the initial conditions of the model near the surface. A larger drop in θ is observed at PIPS2A (Fig. 6.21), which supports a larger sudden drop in θ_e at the PIPS2A location (Fig 6.25) than the three PIPS in north-central Alabama (PIPS1A, PIPS1B, and PIPS2B). θ increases as the CCN concentration which is not present in θ_e time series, and also indicated by the increase in absolute bias for θ as the CCN concentration increases. The larger hydrometeors present in the higher CCN concentration experiments lead to reduced evaporational cooling and therefore weaker and warmer cold pools in higher CCN concentration environments.

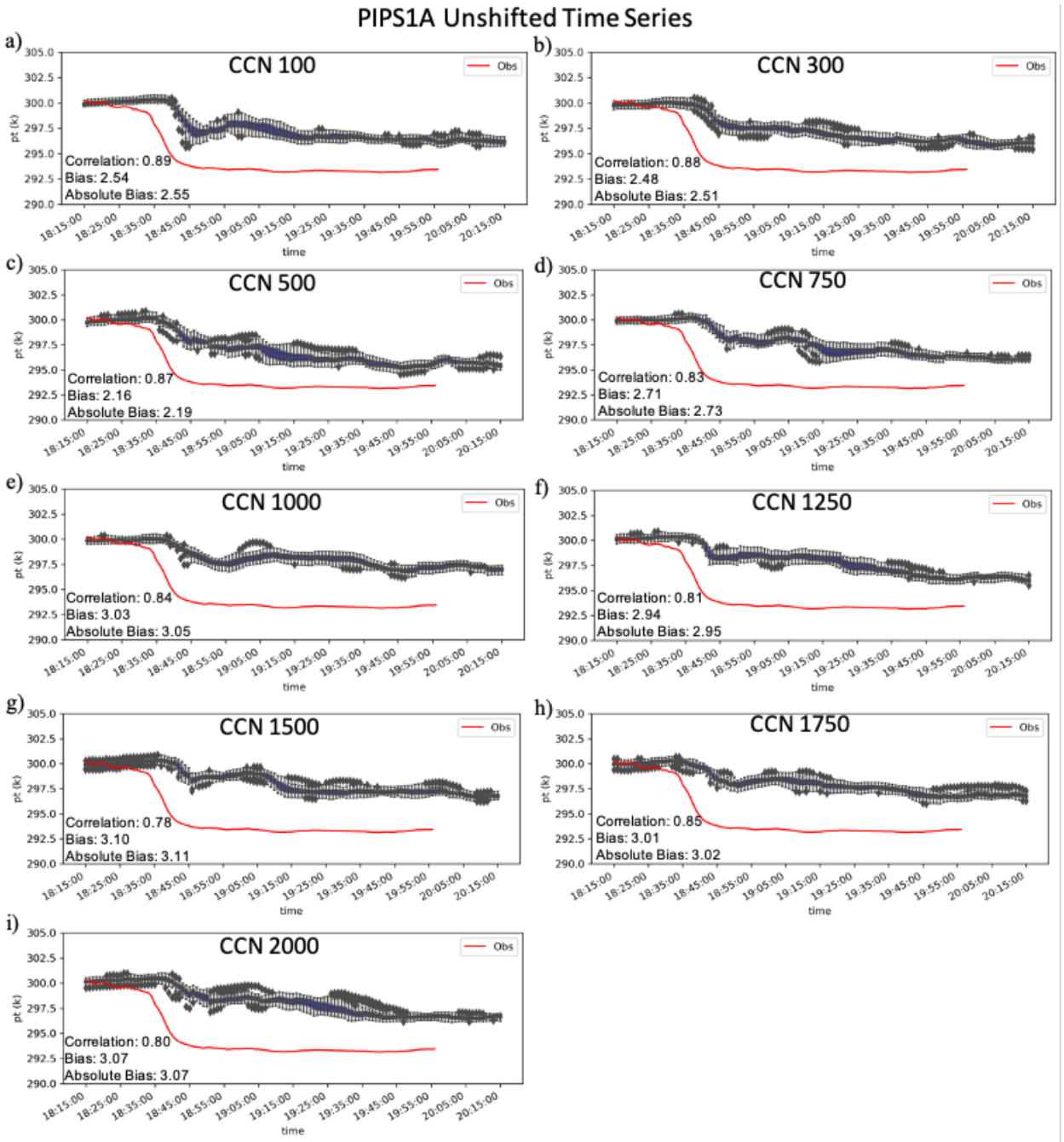

Figure 6-20. The unshifted ensemble member spread of θ (K) (blue box plots) and observed θ (red line) for PIPS1A for the following CCN concentration 1-km experiments in units of cm^{-3}: (a) 100, (b) 300, (c) 500; (d) 750, (e) 1,000, (f) 1,250, (g) 1,500, (h) 1,750, and (i) 2,000.

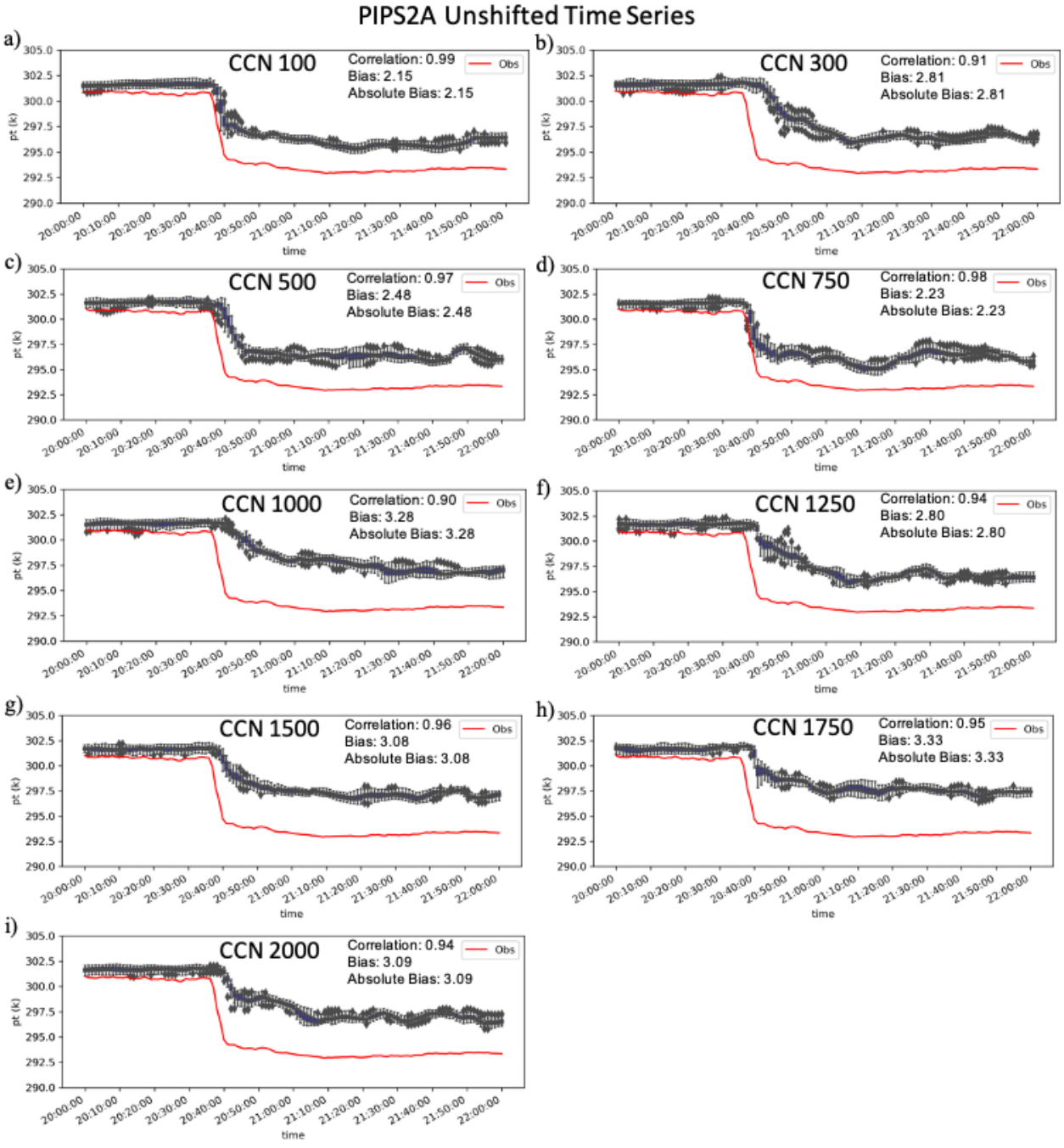

Figure 6-21. As in Fig. 6.20, but for PIPS2A.

Differences in θ_e from the three PIPS located in north-central Alabama and PIPS2A in northeastern Alabama are observed. The QLCS was mature (Fig. 6.3) by the time it approached the three PIPS in north-central Alabama at approximately 1845 UTC (Fig. 6.22), however, the cold pool was not as spatially expansive and uniformly as cold as when the cold pool approached PIPS2A (Fig. 6.23). At 1845 UTC, the cold pool as shown by the ensemble mean θ_e across the CCN concentration experiments in Fig. 6.22 is coldest in areas where the heavier cores of ensemble mean forecast Z are located (Fig. 6.3). The cold pool is not uniformly cold at 1845 UTC but does become more uniformly colder in the mean forecast θ_e by 2045 UTC (Fig. 6.23). As discussed in section 6.1, starting the 1-km experiments earlier in time improved the initial spatial coverage and magnitude of the cold pool as indicated over the three PIPS in north-central Alabama as indicated in the time series for θ_e for PIPS1A (Fig. 6.24).

The results for the time series of θ_e at the PIPS1B and PIPS2B locations are similar to the results of PIPS1A because of the close proximity of PIPS1A, PIPS1B, and PIPS2B. θ_e is overpredicted by approximately 2–3 K at the beginning of the time series for PIPS1A (Fig. 6.24) for all CCN concentration experiments. As the gust front ahead of the QLCS moves over PIPS1A at approximately 1835 UTC, θ_e starts to decrease slowly (Fig. 6.24). θ_e does not sharply drop at PIPS1A nor PIPS1B or PIPS2B, and the model output reflects this. However, the model output for θ_e for nearly all CCN concentrations is underpredicted from 1845 UTC onwards. The CCN concentrations of 1,250 cm^{-3} and 1,500 cm^{-3} are the closest to the observed θ_e. The spread in θ_e among the ensemble members for the CCN concentrations of 1,250 cm^{-3} and 1,500 cm^{-3} is not as large and the statistics reflect this. The large spread in θ_e for some of the CCN concentrations during the passage of the leading convective region of the QLCS over the PIPS location can be attributed to the presence of heavier convective cores in some of the ensemble members causing

the large spread of θ_e. This is visible in several of the CCN concentration experiments from 1845–1900 UTC (Fig. 6.24).

The observed θ_e decreases more suddenly (~5–7 K) at PIPS2A than the previously discussed three PIPS associated with the passage of the gust front ahead of the QLCS from 2035–2040 UTC (Fig. 6.25). Aside from the slight delay of the passage of the gust front and drop in temperature of up to 2 min across several of the experiments (Fig. 6.25), the model output accounts for the sudden decrease in θ_e in the observations. Additionally, the majority of the ensemble members during the trailing stratiform region of the QLCS have a forecast θ_e close to the observed θ_e (Fig. 6.25). A large spread of θ_e is still present among ensemble members during the passage of the leading convective region of the QLCS near 2040 UTC. This is associated with the presence of heavier convective cores passing over PIPS2A in the ensemble members in the CCN concentration experiments this occurs. However, the temperature in the cold pool in the trailing stratiform region of the PIPS2A time series aligns closer to observations than θ_e in the trailing stratiform region of the three PIPS in north-central Alabama. This is reflected in the mean absolute bias across the three PIPS in north-central Alabama across the CCN concentrations (CCN 100–2,000 cm^3) of 4.37 K whereas for PIPS2A the mean absolute bias is 2.79 K. The cold pool θ_e drop is better analyzed for PIPS2A which is consistent with a longer period of data assimilation.

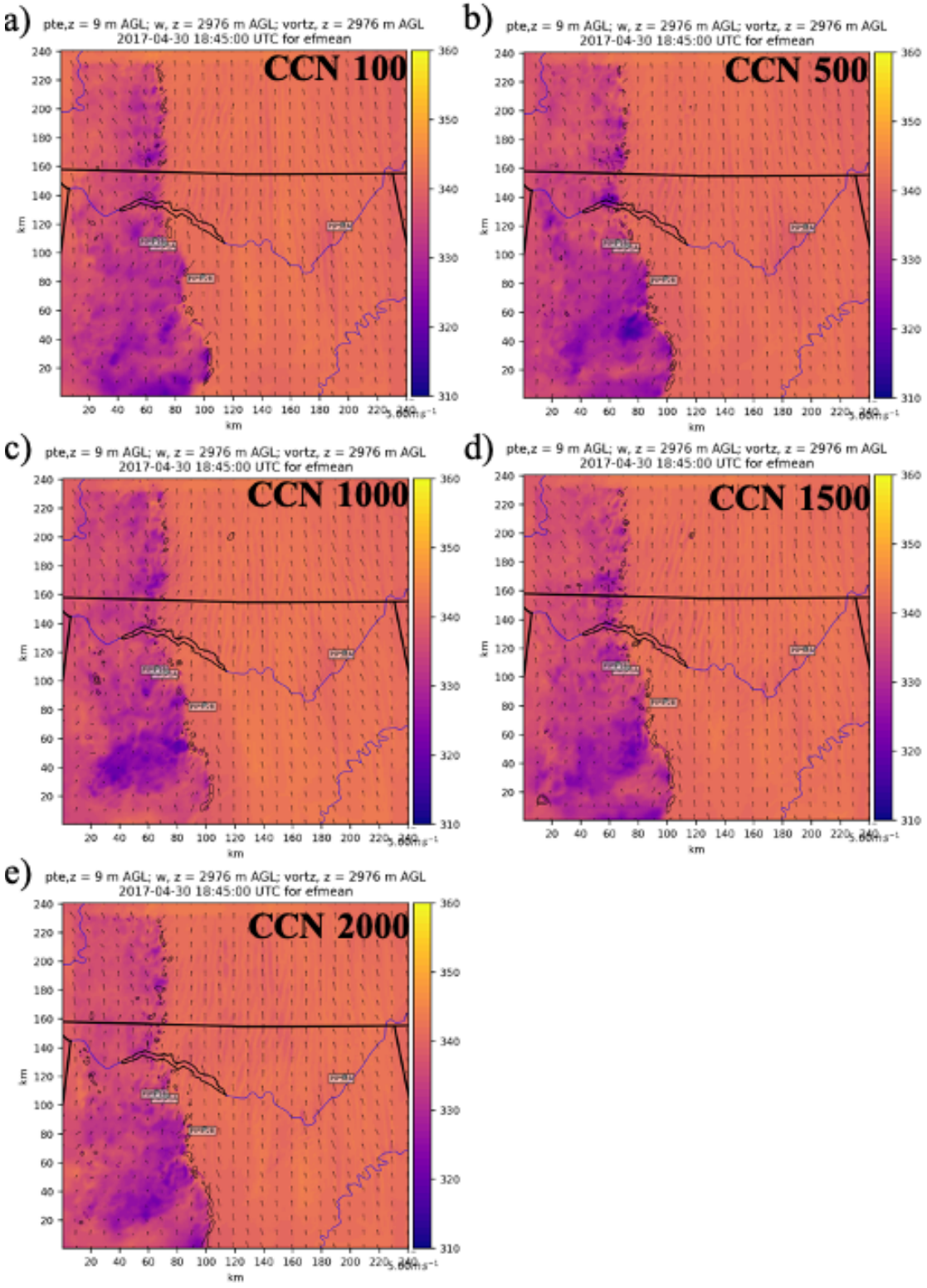

Figure 6-22. The forecast mean θ_e (K), vertical vorticity (purple contours), and vertical velocity (black contours) of all 40 ensemble members for 1845 UTC for the 1-km experiments for the following CCN concentrations in units of cm^{-3} (a) 100; (b) 500; (c) 1,000; (d) 1,500; and (e) 2,000.

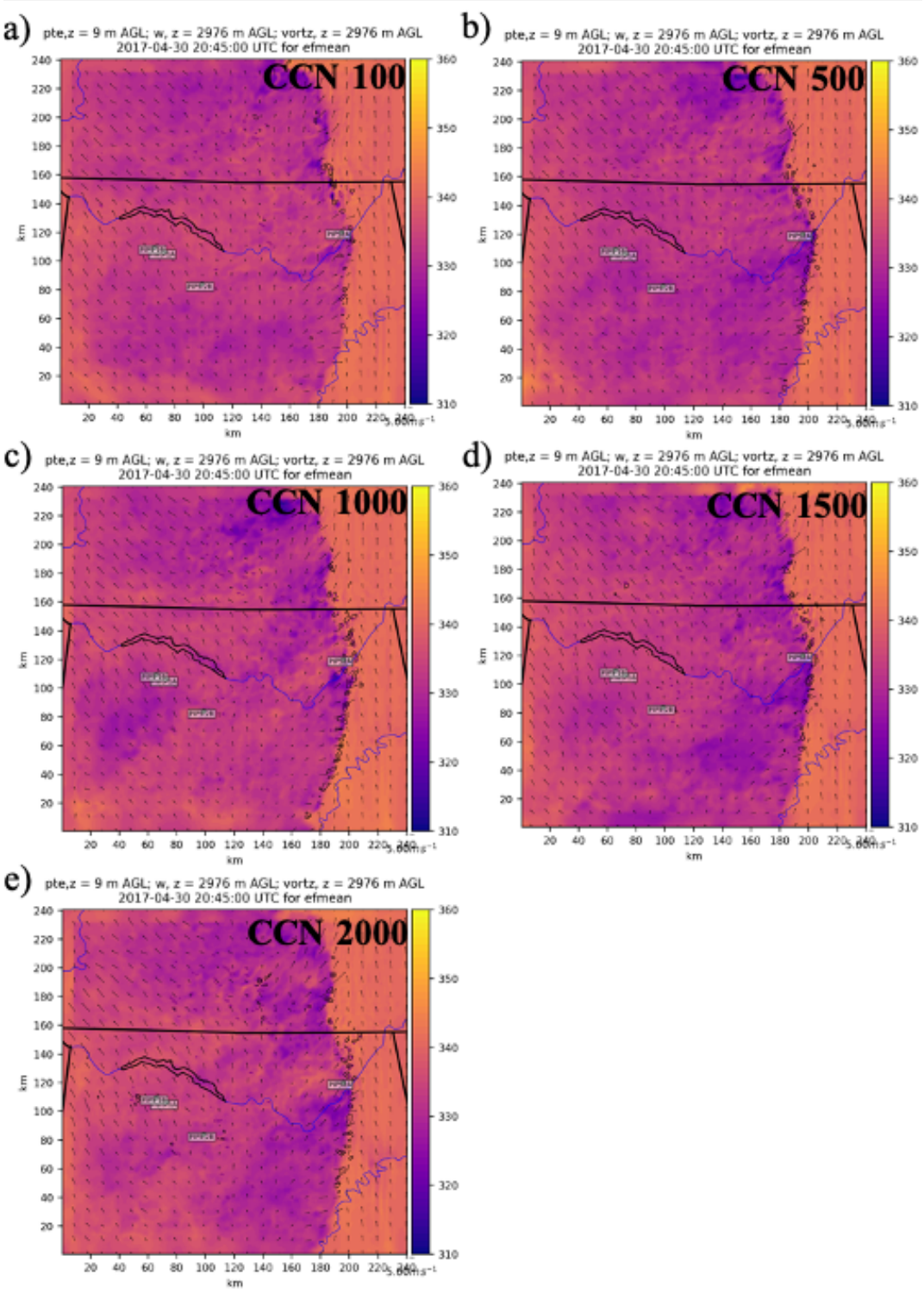

Figure 6-23. As in Fig. 6.22, but for 2045 UTC.

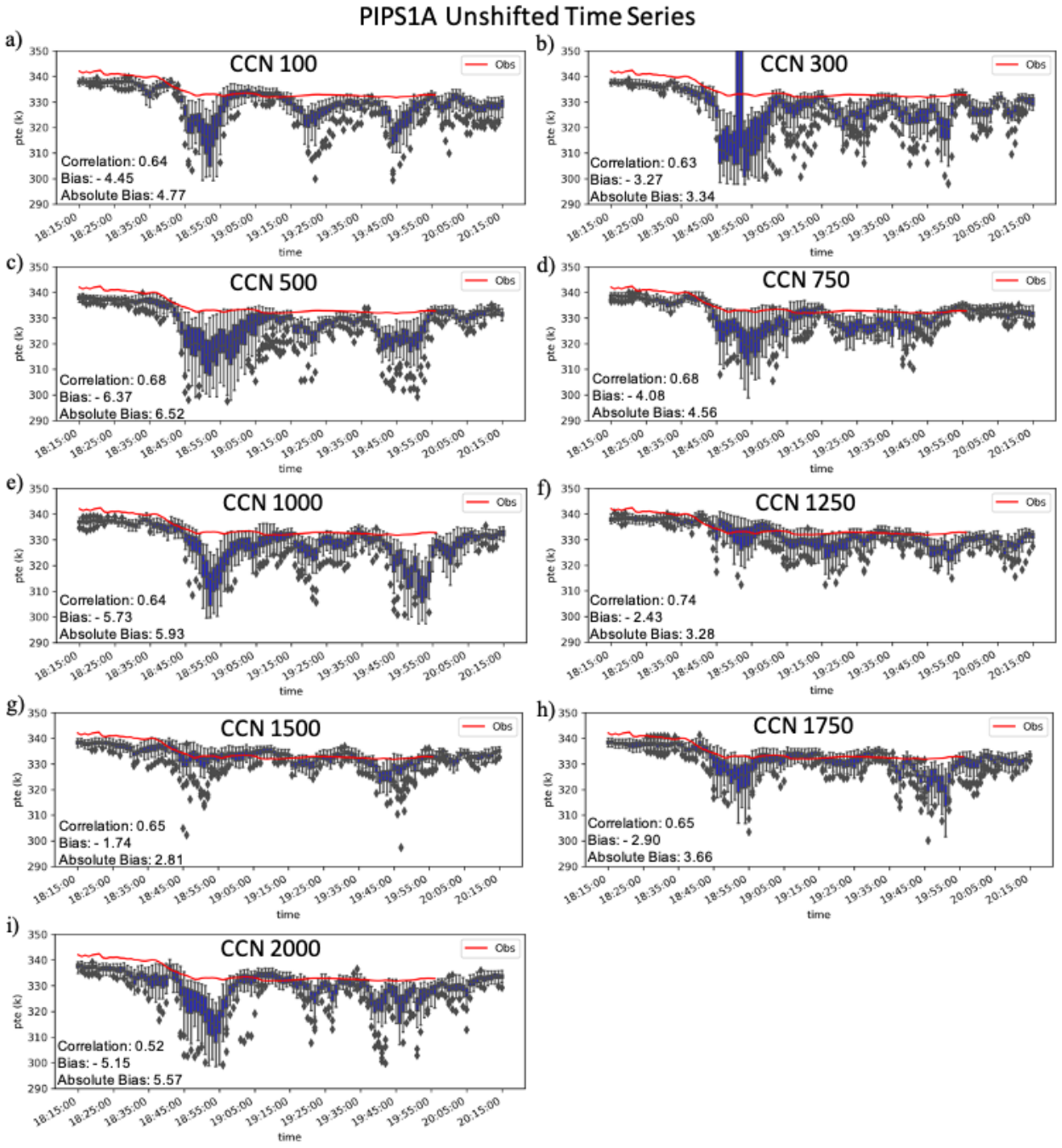

Figure 6-24. The unshifted ensemble member spread of θ_e (K) (blue box plots) and observed θ_e (red line) for PIPS1A for the following CCN concentration 1-km experiments in units of cm^{-3}: (a) 100, (b) 300, (c) 500; (d) 750, (e) 1,000, (f) 1,250, (g) 1,500, (h) 1,750, and (i) 2,000.

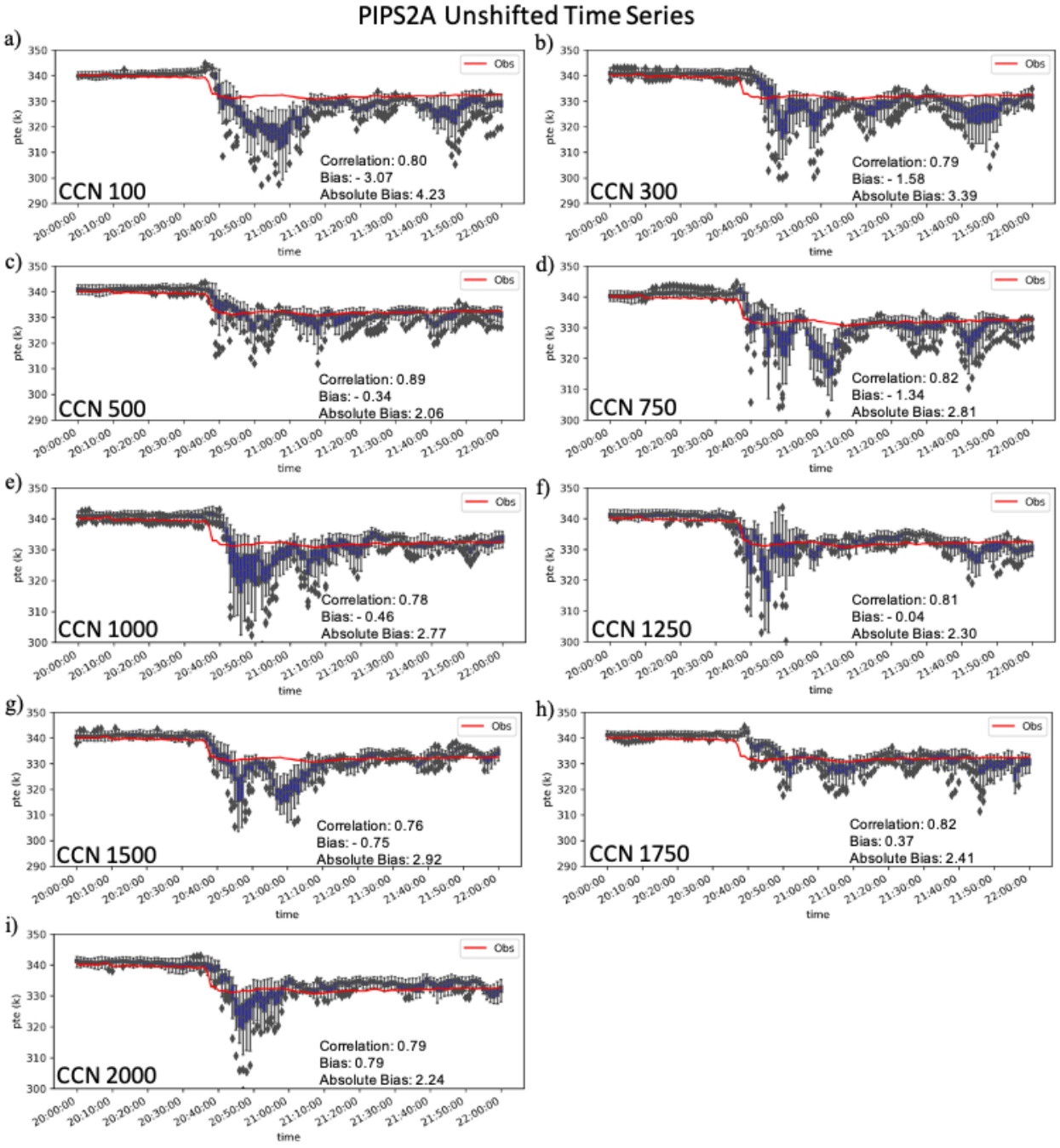

Figure 6-25. As in Fig. 6.24, but for PIPS2A.

How can θ_e be underpredicted (sometimes significantly) in several of the CCN concentration experiments, but θ be overpredicted? θ_e depends on both moisture and temperature. To analyze differences in moisture between the model output and observations, *w* is discussed for PIPS1A (Fig. 6.26). Initially, the model output *w* is within 0.01 kg kg^{-1} of the observed *w*. Differences in *w* arise as the gust front passes and the cold pool moves over the PIPS location. The cold pool is drier than the observations by 0.02–0.04 kg kg^{-1} at PIPS1A and the PIPS now shown. The drier environment throughout the CCN concentration experiments in the cold pool causes the negative biases of θ_e.

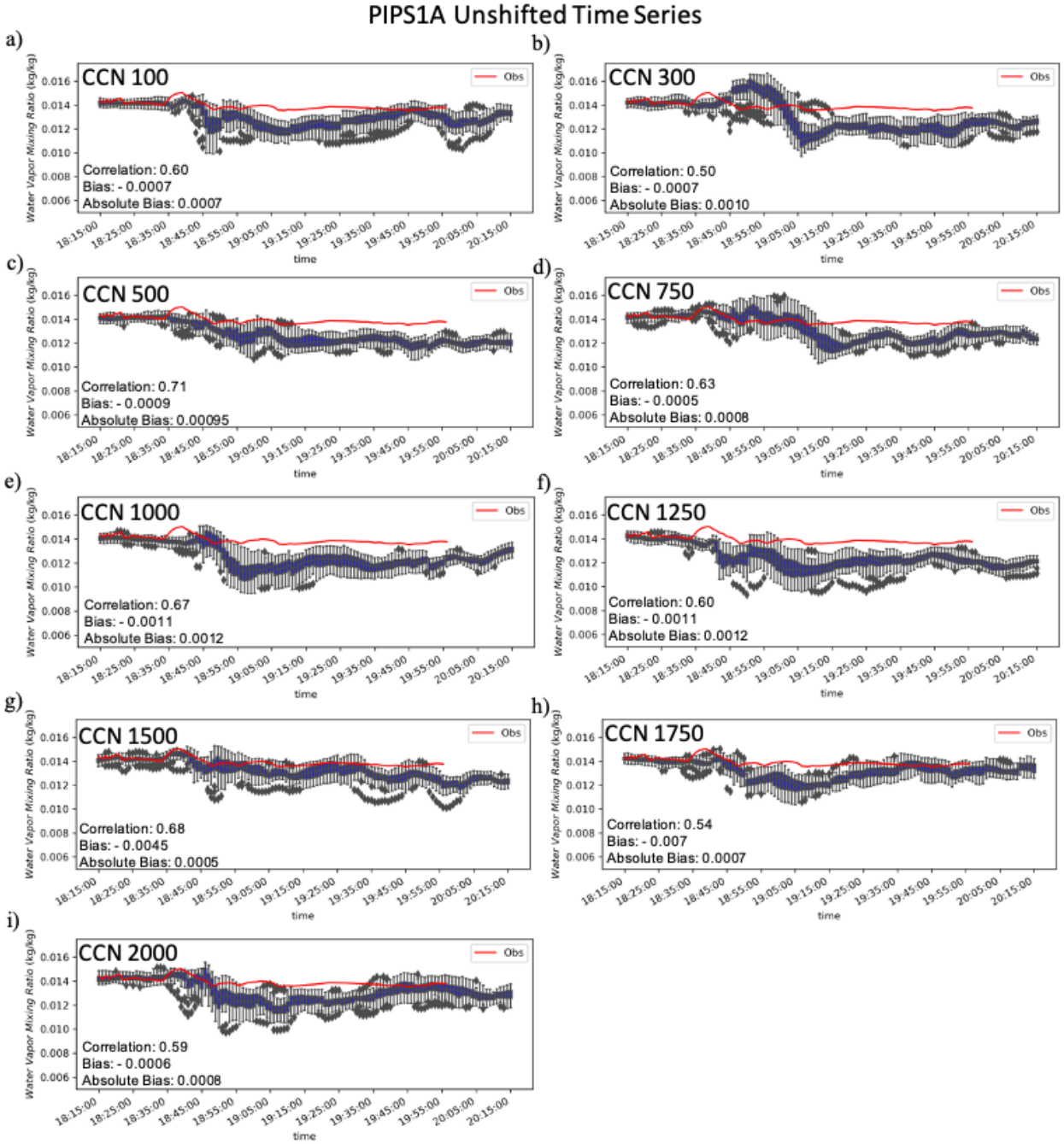

Figure 6-26. The unshifted ensemble member spread of w (kg kg^{-1}) (blue box plots) and observed w (red line) for PIPS1A for the following CCN concentration 1-km experiments in units of cm^{-3}: (a) 100, (b) 300, (c) 500; (d) 750, (e) 1,000, (f) 1,250, (g) 1,500, (h) 1,750, and (i) 2,000.

6.5 1-km ARPS simulations to PIPS kinematic comparisons

Comparisons between the unshifted observed wind speed (m s^{-1}) and wind direction (°) at the PIPS locations and the model output from the CCN concentration experiments will now be discussed. The results from only PIPS1A are discussed since the results from the other PIPS (PIPS1B, PIPS2A, and PIPS2B) all demonstrate similar results. The lowest level of model output is approximately 9 m AGL, whereas the PIPS observations are approximately 1.8 m AGL. The model output wind speed is overpredicted in all CCN concentration experiments because of the difference in elevation (Fig. 6.27). Boundary layer approximations for neutral conditions using the Monin-Obukov similarity theory suggest the wind speed at height 9 m can be 2–4 m s^{-1} stronger than the height at 2 m (Stull 1988). Taking this into account, the model output wind speed for the CCN concentration experiments align closer to the magnitudes of the observed wind speed. More importantly, the peak in wind speed in the model output associated with the passage of the gust front of the QLCS is captured by the CCN concentration experiments, but slightly delayed.

Wind direction is not influenced by the difference between the height of the PIPS and lowest level of model output. Aside from the large spread in ensemble member wind direction from 1945–2000 UTC in the CCN 300 cm^{-3} experiment (Fig. 6.28b), the rest of the CCN concentration experiments adequately predict the switch from southerly to westerly winds with the passage of the gust front (Fig. 6.28). There are subtle differences in timing of the wind shift, but the wind shift is present in each of the CCN concentration experiments. The shift from westerly back to southerly winds throughout the passage of the trailing stratiform region is also observed in each of the experiments. Overall, wind speed and wind direction are well modeled by the CCN concentrations experiments and no clear trend exists.

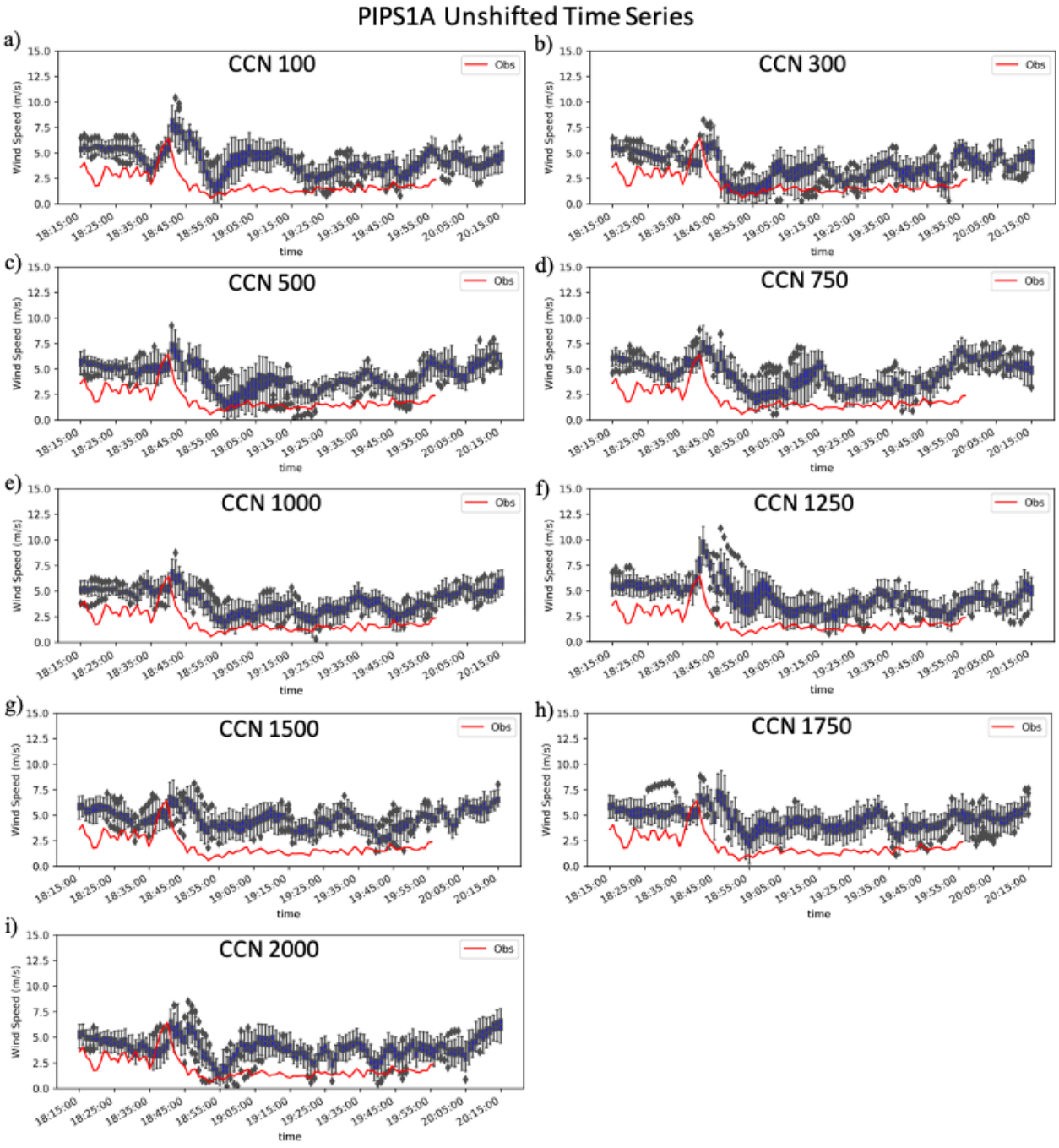

Figure 6-27. The unshifted ensemble member spread of wind speed (m s^{-1}) (blue box plots) and observed wind speed (red line) for PIPS1A for the following CCN concentration 1-km experiments: (a) 100, (b) 300, (c) 500; (d) 750, (e) 1,000, (f) 1,250, (g) 1,500, (h) 1,750, and (i) 2,000.

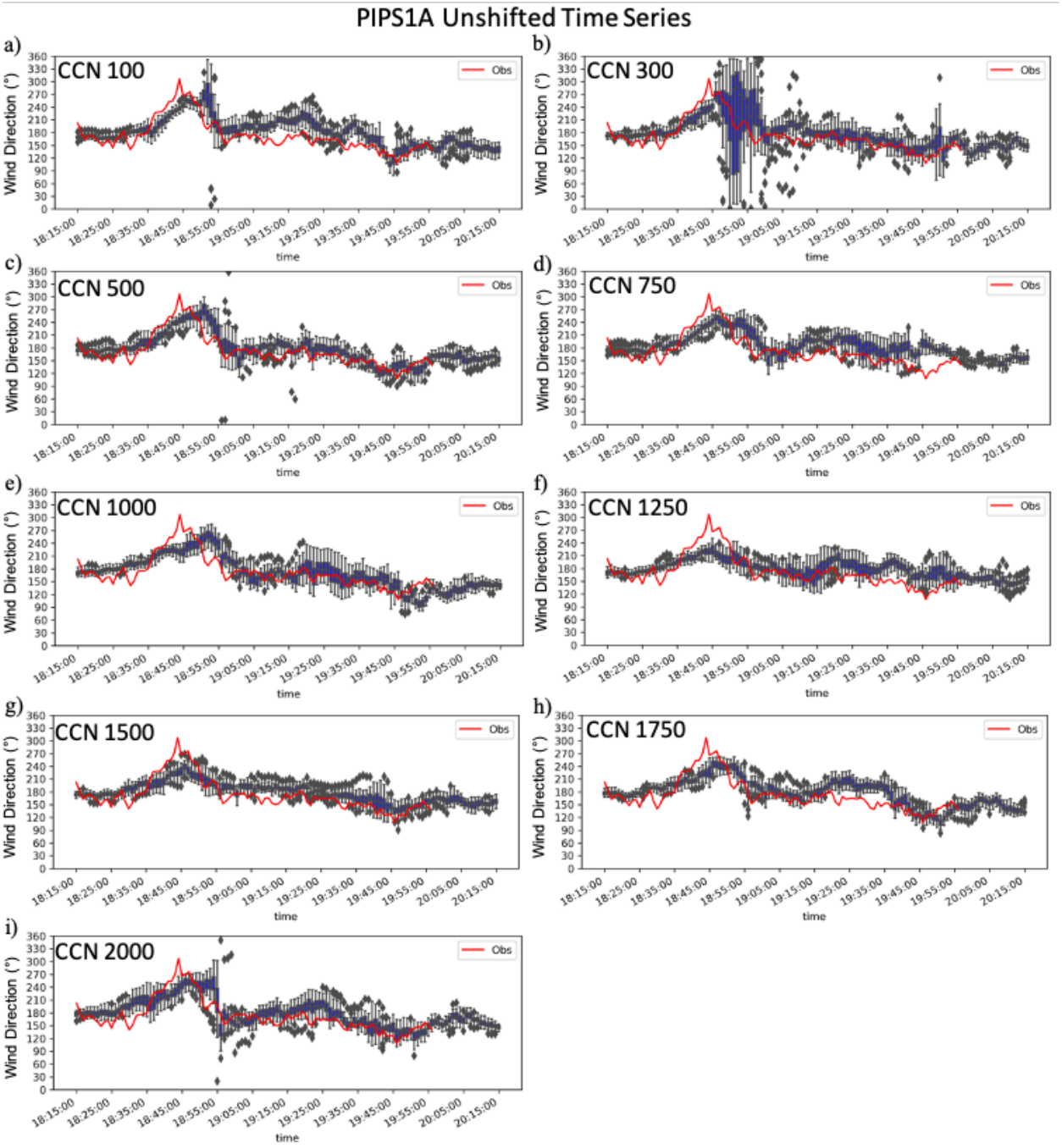

Figure 6-28. As in Fig. 6.27, but for wind direction (°) at PIPS1A.

CHAPTER 7. CONCLUSION AND DISCUSSION

In this study, the sensitivity of the DSD variability to CCN concentrations is evaluated. DSDs from ARPS-EnKF model analyses and forecasts using the NSSL-TM microphysics scheme are compared with observed DSDs from four PIPS deployed during the 30 April 2017 tornadic QLCS. Nine different experiments with CCN concentrations ranging from 100 cm^{-3} (maritime) to 2,000 cm^{-3} (continental) are conducted. The key takeaway points are:

1. The overall structure of the QLCS is well modeled by the CCN concentration experiments.
2. The NSSL-TM microphysics scheme produces model output that aligns closely to the observations for all the different CCN concentration experiments.
3. The shifted time series align with the observations better than the unshifted time series and result in lower absolute bias and higher correlation.
4. D_0 increases as the CCN concentration increases as indicated by the trend from a negative to increasingly positive bias. This agrees with previous work indicating the influence of cold rain processes in higher CCN concentrations resulting in DSDs characterized by larger drops.
5. The intermediate CCN concentrations close to CCN 1,000 cm^{-3} produce D_0 closest to the observed D_0 throughout the trailing stratiform region. The lower (higher) CCN concentrations underpredict (overpredict) D_0 in the trailing stratiform region.
6. The assimilation of clear air radar data suppresses spurious convection ahead of the QLCS.
7. Lower CCN concentrations have a larger Z closer to the calculated observed Z than the intermediate and higher CCN concentrations for the leading convective edge of the QLCS.

The intermediate and higher CCN concentration experiments produce Z in the trailing stratiform region that aligns closer to observations.

8. Z_{DR} increases as the CCN concentration increases which supports the result of D_0 increasing as CCN concentration increases. Z_{DR} is overpredicted for the intermediate and higher CCN concentrations.
9. θ is overpredicted in the cold pool for all CCN concentration experiments. All experiments have a dry bias in the cold pool as indicated in the w plots. Since θ_e is based on moisture and temperature, this results in the model output θ_e being lower than the observed θ_e. Starting the 3-km and 1-km experiments earlier in time eliminated the magnitude of the warm bias since the QLCS and associated cold pool were more mature in the model.
10. Other variables such as the wind speed and wind direction accord closely to observations.

The timing differences of the QLCS and observations are important. The CCN concentration experiments are delayed by up to 4 min with the onset of precipitation and therefore maximums and minimums in the observed variables throughout the passage of the QLCS. On the one hand, the fact that virtually all the experiments show such a delay is consistent with the fact that the radar data are assumed to be valid at the same time when in reality they are valid at different times for different heights over a 5-min period prior to the assimilation. The assimilation of radar data could be restructured to account for this, which could improve the raw model output timing. On the other hand, the lower CCN concentrations are delayed more than the intermediate and higher CCN concentrations. The timing differences between CCN concentrations may be due to how the different CCN concentrations influence precipitation processes. For example, higher CCN concentration simulations can delay autoconversion and accretion processes which can delay the onset of precipitation (Saleeby et al. 2010).

A novel aspect of this study is the direct comparison of model output DSDs with observed DSDs using the NSSL-TM microphysics scheme. This work reveals that the NSSL-TM microphysics scheme can adequately represent surface rain DSDs as compared with disdrometer observations for a QLCS in the SE-US. This was quantified by examining the time series of several DSD-related parameters including D_0.

In conclusion, consistent trends are observed with surface DSDs that are well removed from the change in CCN concentration. The CCN concentration was set to an initially horizontally homogeneous value in the outer 6-km grid at the beginning of the experiment. The CCN concentration was not altered on the 1-km or 3-km experiments. Instead, the inner domain experiments inherited the CCN concentration field from the outer domain through the ICBC. Since no other variables were changed in any of the simulations, the changes observed in surface DSDs are ultimately due to the change in CCN concentration between the different experiments and the relative influence of different microphysical processes. The implications of modeling convective storm environments in the SE-US is that intermediate CCN concentrations (750–1,250 cm^{-3}) close to those of the central Plains, produce model output that aligns closest to observations. Understanding a range of appropriate CCN concentrations to use in a numerical model can not only help better predict several microphysical variables, but also potentially better forecast tornadoes because of the impact of microphysics on thunderstorm dynamics.

Future work includes assessing microphysical process rates to further evaluate differences between the various CCN concentration experiments. The relative influence of warm and cold rain processes will be analyzed to investigate how this affects ice processes aloft along with surface DSDs. Model output DSDs will also be put through a "Parsivel simulator" to account for instrumental error and sampling effects of the surface rain DSDs. These simulated model DSDs

could improve the relationship with the observed DSDs. This will aid in further evaluating the model microphysics. Additionally, comparisons of WSR-88D Z and Z_{DR} with model output are planned as future work to further evaluate the different CCN concentration experiments. Upper-air profiles can also be computed from the model output and directly compared with radiosondes collected by the NWS and VORTEX-SE collaborators. Expanding this work to more VORTEX-SE case studies such as other QLCS events and cellular storm modes is necessary to further increase the robustness of these results. Furthermore, the magnitude and source region of the advection of air is likely sensitive to different environmental set ups. These include how strong the southerly flow is from the Gulf of Mexico to the SE-US and what kind of air is advected inland (pristine maritime air or modified polluted air from Mexico).

REFERENCES

Aksoy, A., D. C. Dowell, and C. Snyder, 2010: A multicase comparative assessment of the ensemble Kalman filter for assimilation of radar observations. Part II: Short-range ensemble forecasts. *Mon. Wea. Rev*., **138**, 1273–1292.

American Meteorological Society, cited 2021: "Differential reflectivity". Meteorology Glossary. [Available online at https://glossary.ametsoc.org/wiki/Differential_reflectivity].

Anderson-Frey, A. K., Y. P. Richardson, A. R. Dean, R. L. Thompson, and B. T. Smith, 2019: Characteristics of tornado events and warnings in the southeastern United States. *Wea. Forecasting*, **34**, 1017–1034.

Andreae, M. O., D. Rosenfeld, P. Artaxo, A. A. Costa, G. P. Frank, K. M. Longo, and M. A. F. Silva-Dias, 2004: Smoking rain clouds over the Amazon, *Science*, **303**, 1337–1342.

Ashley, W. S., 2007: Spatial and temporal analysis of tornado fatalities in the United States: 1880–2005. *Wea. Forecasting*, **22,** 1214–1228.

——, A. J. Krmenec, and R. Schwantes, 2008: Vulnerability due to nocturnal tornadoes. *Wea. Forecasting,* **23**, 795–807.

Atkins, N. T., J. M. Arnott, R. W. Przybylinski, R. A. Wolf, and B. D. Ketcham, 2004: Vortex structure and evolution within bow echoes. Part I: Single-Doppler and damage analysis of the 29 June 1998 derecho. *Mon. Wea. Rev.*, **132**, 2224–2242.

Atlas, D., and C. W. Ulbrich, 1977: Path- and area-integrated rainfall measurement by microwave attenuation in the 1–3 cm band. *J. Appl. Meteor*., **16**, 1322–1331.

Bergthorsson, P., B. Doos, S. Frykland, O. Hang, and R. Linquist, 1955: Routine forecasting with the barotropics model, *Tellus,* **7**, 329–340.

Bolton, D., 1980: The computation of equivalent potential temperature. *Mon. Wea. Rev*., **108**, 1046-1053.

Brotzge, J., and S. Erickson, 2010: Tornadoes without NWS warning. *Wea. Forecasting,* **25**, 159–172.

Cao, Q., G. Zhang, E. A. Brandes, T. Schuur, A. Ryzhkov, and K. Ikeda, 2008: Analysis of video disdrometer and polarimetric radar data to characterize rain microphysics in Oklahoma. *J. Appl. Meteor. Climatol.,* **47**, 2238–2255.

Charney, J. G., R. Fjørtoft, and J. von Neuman, 1950: Numerical integration of the barotropic vorticity equation. *Tellus,* **2**, 237–254.

Chen, B., J. Wang, and D. Gong, 2016: Raindrop size distribution in a midlatitude continental squall line measured by Thies optical disdrometers over east China, *J. Appl. Meteor. Climatol.,* **55**, 621-634.

Cheng, C. T., W. C. Wang, and J. P. Chen, 2010: Simulation of the effects of increasing cloud condensation nuclei on mixed-phase clouds and precipitation of a front system. *Atmos. Res.*, **96**, 461–476.

Chou, M. D. 1990: Parameterization for the absorption of solar radiation by O2 and CO2 with application to climate studies. *J. Climate*. **3**, 209–217.

——, 1992: A solar radiation model for climate studies. *J. Atmos. Sci.* **49**, 762–772.

——, M. J. Suarez, 1994: An efficient thermal infrared radiation parameterization for use in general circulation models, *NASA Tech. Memo.* **104606**, 85 pp.

Cohard, J. M. and J. P. Pinty, 2000: A comprehensive two-moment warm microphysical bulk scheme. I: Description and tests. *Q.J.R. Meteorol. Soc.*, **126**, 1815–1842.

Davis, J. M., and M. D. Parker, 2012: Radar climatology of tornadoes occurring in high shear/low CAPE environments in the mid-Atlantic and Southeast. Preprints, *26th Conf. on Severe Local Storms*, Nashville, TN, Amer. Meteor. Soc., 9.2. [https://ams.confex.com/ams/26SLS/webprogram/Paper211761.html].

——, and M. D. Parker, 2014: Radar climatology of tornadic and nontornadic vortices in high-shear, low-CAPE environments in the mid-Atlantic and southeastern United States. *Wea. Forecasting,* **29**, 828–853.

Dawson, D. T., and M. Xue, 2006: Numerical forecasts of the 15–16 June 2002 southern Plains mesoscale convective system: Impact of mesoscale data and cloud analysis. *Mon. Wea. Rev.,* **134**, 1607–1629.

——, ——, J. A. Milbrandt, and M. K. Yau, 2010: Comparison of evaporation and cold pool development between single-moment and multimoment bulk microphysics schemes in idealized simulations of tornadic thunderstorms. *Mon. Wea. Rev.*, **138**, 1152–1171.

——, L. J. Wicker, E. R. Mansell, and R. L. Tanamachi, 2012: Impact of the environmental low-level wind profile on ensemble forecasts of the 4 May 2007 Greensburg, Kansas, tornadic storm and associated mesocyclones. *Mon. Wea. Rev.*, **140**, 696–716.

——, ——, ——, Y. Jung, and M. Xue, 2013: Low-level polarimetric radar signatures in EnKF analyses and forecasts of the May 8, 2003 Oklahoma City tornadic supercell: Impact of multimoment microphysics and comparisons with observation. *Adv. Meteor.*, **2013**, Article ID 818394, 13 pages.

——, E. R. Mansell, Y. Jung, L. J. Wicker, M. R. Kumjian, and M. Xue, 2014: Low-level Z_{DR} signatures in supercell forward flanks: The role of size sorting and melting of hail. *J. Atmos. Sci.*, **71**, 276–299.

——, M. Xue, J. A. Milbrandt, and A. Shapiro, 2015: Sensitivity of real-data simulations of the 3 May 1999 Oklahoma City tornadic supercell and associated tornadoes to multimoment microphysics. Part I: Storm- and tornado-scale numerical forecasts. *Mon. Wea. Rev.*, **143**, 2241–2265.

——, ——, ——, ——, and A. D. Schenkman, 2016: Sensitivity of real-data simulations of the 3 May 1999 Oklahoma City tornadic supercell and associated tornadoes to multimoment microphysics. Part II: Analysis of buoyancy and dynamic pressure forces in simulated tornado-like vortices. *J. Atmos. Sci.*, **73**, 1039–1061.

Dean, A. R., and R. S. Schneider, 2008: Forecast challenges at the NWS Storm Prediction Center relating to the frequency of favorable severe storm environments. Preprints, *24th Conf. Severe Local Storms*, Savannah GA, Amer. Meteor. Soc., 9A.2. [https://ams.confex.com/ams/24SLS/webprogram/Paper141743.html].

Dowell, D. C., F. Zhang, L. J. Wicker, C. Snyder, and N. A. Crook, 2004b: Wind and temperature retrievals in the 17 May 1981 Arcadia, Oklahoma, supercell: Ensemble Kalman filter experiments. *Mon. Wea. Rev.*, **132**, 1982–2005.

——, L. J. Wicker, and C. Snyder, 2011: Ensemble Kalman filter assimilation of radar observations of the 8 May 2003 Oklahoma City supercell: Influences of reflectivity observations on storm-scale analyses. *Mon. Wea. Rev.*, **139**, 272–294.

Earth Observing Laboratory, cited 2020: Purdue University Portable in Situ Precipitation Stations (PIPS) Data. [Available online at https://data.eol.ucar.edu/dataset/541.029].

Earth Resources Observation and Science Center/U.S. Geological Survey/U.S. Department of the Interior, 1997: USGS 30 ARC-second Global Elevation Data, GTOPO30. Research Data Archive at the National Center for Atmospheric Research, Computational and Information Systems Laboratory, Boulder, CO. 10 Dec 2020.

Evensen, G, 1994: Sequential data assimilation with a non-linear quasi-geostrophic model using Monte Carlo methods to forecast error statistics. *J. Geo. Research*, **99**, 10143–10162.

——, 2009: Data Assimilation: The Ensemble Kalman Filter. Springer. 307 pp.

Friedrich, K., E. A. Kalina, F. J. Masters, and C. R. Lopez, 2013: Drop-size distributions in thunderstorms measured by optical disdrometers during VORTEX2. *Mon. Wea. Rev.*, **141**, 1182–1203.

Gilmore, M. S., J. M. Straka, and E. N. Rasmussen, 2004: Precipitation uncertainty due to variations in precipitation particle parameters within a simple microphysics scheme. *Mon. Wea. Rev.,* **132**, 2610–2627.

Gunn, R., and Kinzer, G. D., 1949: The terminal velocity of fall for water droplets in stagnant air, *J. Atmos. Sci.*, **6**, 243-248.

Hart, J., P. Marsh, and R. Thompson., 2017: SPC Mesoscale Analysis Pages, NOAA NWS Storm Prediction Center, Accessed 3 July 2020 [http://catalog.eol.ucar.edu/vortex-se_2017/analysis/2017/04/30].

Hirth, B. D., J. L. Schroeder, and C. C. Weiss, 2008: Surface analysis of the rear-flank downdraft outflow in two tornadic supercells. *Mon. Wea. Rev.*, **136**, 2344–2363.

Hosking, J. R., 1992: Moments or *L* moments? An example comparing two measures of distributional shape, *The American Statistician*, **46**, 186–189.

Houtekamer, P. L. and H. L. Mitchell, 1998: Data assimilation using an ensemble Kalman filter technique. *Mon. Wea. Rev*., **126**, 796–811.

Johnson, K. W., J. Bauer, G. A. Riccardi, K. K. Droegemeier, and M. Xue, 1994: Distributed processing of a regional prediction model. *Mon. Wea. Rev*., **122**, 2558–2572.

Jones, T. A., P. Skinner, K. Knopfmeier, E. Mansell, P. Minnis, R. Palikonda, and W. Smith, 2018: Comparison of cloud microphysics schemes in a warn-on-forecast system using synthetic satellite objects. *Wea. Forecasting*, **33**, 1681–1708.

Jouan, C., and J. A. Milbrandt, 2019: The importance of the ice-phase microphysics parameterization for simulating the effects of changes to CCN concentrations in deep convection. *J. Atmos. Sci.*, **76**, 1727–1752.

Jung, Y., G. Zhang, and M. Xue, 2008a: Assimilation of simulated polarimetric radar data for a convective storm using the ensemble Kalman filter. Part I: Observation operators for reflectivity and polarimetric variables. *Mon. Wea. Rev*., **136**, 2228–2245.

——, M. Xue, G. Zhang, and J. M. Straka, 2008b: Assimilation of simulated polarimetric radar data for a convective storm using the ensemble Kalman filter. Part II: Impact of polarimetric data on storm analysis. *Mon. Wea. Rev.,* **136**, 2246–2260.

——, ——, and M. Tong, 2012: Ensemble Kalman Filter Analyses of the 29–30 May 2004 Oklahoma Tornadic Thunderstorm Using One- and Two-Moment Bulk Microphysics Schemes, with Verification against Polarimetric Radar Data. *Mon. Wea. Rev.*, **140**, 1457–1475.

Kalnay, E., 2003: Atmospheric modeling, data assimilation, and predictability. Cambridge University Press. 369 pp.

Kalina, E. A., K. Friedrich, H. Morrison, and G. Bryan, 2014: Aerosol Effects on Idealized Supercell Thunderstorms in Different Environments, *J. Atmos. Sci*, **71**, 4558-4580.

Khain, A. P., D. Rosenfeld, and A. Pokrovsky, 2005: Aerosol impact on the dynamics and microphysics of deep convective clouds. *Quart. J. Roy. Meteor. Soc.,* **131**, 2639–2663.

Kidwell, K. B. E., 1990: Global Vegetation Index User's guide, USDOC/NOAA National Climate Data Center, Satellite Data Services Division, Washington DC.

Kineman J. J., M.A. Ohrenschall, 1992: Global Ecosystem Database (CD-ROM) Version 1.0 Documentation Manual. EPA/600/R-96/194b, NGDC Key to Geophysical Records Documentation No 27, National Geophysical Data Center, NOAA, Boulder, CO.

Kumjian, M. R., Z. J. Lebo, and H. C. Morrison, 2015: On the mechanisms of rain formation in an idealized supercell storm. *Mon. Wea. Rev*., **143**, 2754–2773.

Lilly, D. K., 1990: Numerical prediction of thunderstorms—Has its time come? *Quart. J. Roy. Meteor. Soc.*, **116**, 779–798.

Löffler-Mang, M., and J. Joss, 2000: An optical disdrometer for measuring size and velocity of hydrometeors. *J. Atmos. Ocean. Technol*., **17**, 130–139.

Mahale, V. N., J. A. Brotzge, and H. B. Bluestein, 2012: An analysis of vortices embedded within a quasi-linear convective system using x-band polarimetric radar. *Wea. Forecasting,* **27**, 1520–1537.

Maki, M., T. D. Keenan, Y. Sasaki, and K. Nakamura, 2001: Characteristics of the raindrop size distribution in tropical continental squall lines observed in Darwin, Australia. *J. Appl. Meteor.*, **40**, 1393–1412.

Markowski, P. M., J. M. Straka, and E. N. Rasmussen, 2003: Tornadogenesis resulting from the transport of circulation by a downdraft: Idealized numerical simulations. *J. Atmos. Sci.*, **60**, 795–823.

——, and Y. P. Richardson, 2010: *Mesoscale Meteorology in Midlatitudes*. John Wiley and Sons, Ltd, 407 pp.

Marshall, J. S., and W. M. Palmer, 1948: The size distribution of raindrops. *Q. J. R. Meteorol. Soc.*, **76**, 16–36.

Mansell, E. R., C. L. Ziegler, and E. C. Bruning, 2010: Simulated electrification of a small thunderstorm with two-moment bulk microphysics. *J. Atmos. Sci.*, **67**, 171–194.

Midwest Regional Climate Center, cited 2021: Tornado Tracks 1950-2017. [Available online at https://mrcc.illinois.edu/gismaps/cntytorn.htm#].

Milbrandt, J. A., and M. K. Yau, 2005a: A multimoment bulk microphysics parameterization. Part I: Analysis of the role of the spectral shape parameter. *J. Atmos. Sci.,* **62**, 3051–3064.

——, and M. K. Yau, 2005b: A multimoment bulk microphysics parameterization. Part II: A proposed three-moment closure and scheme description. *J. Atmos. Sci.,* **62**, 3065–3081.

——, and R. McTaggart-Cowan, 2010: Sedimentation-induced errors in bulk microphysics schemes. *J. Atmos. Sci.*, **67**, 3931–3948.

Moumouni, S., M. Gosset, and E. Houngninou, 2008: Main features of rain drop size distributions observed in Benin, West Africa, with optical disdrometers. *Geophys. Res. Lett.*, **35**, L23807.

Nzeukou, A., H. Sauvageot, A. D. Ochou, and C. M. F. Kebe, 2004: Raindrop size distribution and radar parameters at Cape Verde. *J. Appl. Meteor.*, **43**, 90–105.

NCEI Automated Surface Observing System (ASOS), cited 2020: 5-minute ASOS data. [Available online at https://www.ncdc.noaa.gov/data-access/land-based-station-data/land-based-datasets/automated-surface-observing-system-asos].

NCEI North American Mesoscale Forecast System (NAM), cited 2020. NAM forecasts archive [Available online at https://www.ncdc.noaa.gov/data-access/model-data/model-datasets/north-american-mesoscale-forecast-system-nam].

NCEI Radar Data, cited 2020: NEXRAD data archive, inventory, and access. [Available online at https://www.ncdc.noaa.gov/nexradinv/].

NWS Huntsville, Alabama, cited 2020 Damaging winds and an isolated tornado on April 30, 2017. [Available online at https://www.weather.gov/hun/event_043017].

NWS Storm Prediction Center, cited 2020: Severe weather climatology (1982-2011). [Available online at https://www.spc.noaa.gov/new/SVRclimo/climo.php?parm=anySvr].

——, cited 2020: Severe weather event: April 30, 2017. [Available online at https://www.spc.noaa.gov/exper/archive/event.php?date=20170430].

NSSC, 1994: State Soil Geographic (STATSGO) Data Base. Miscellaneous Publication Number 1492, National Soil Survey Center, United States Department of Agriculture.

Park, S. G., H. L. Kim, Y. W. Ham, and S. H. Jung, 2017: Comparative evaluation of the OTT PARSIVEL2 using a collocated two-dimensional video disdrometer. *J. Atmos. Ocean. Technol*., **34**, 2059–2082.

Park, S. K., and Liang, X, 2013: Data Assimilation for Atmospheric, Oceanic and Hydrologic Applications - Vol. II. Springer. 715 pp.

Rasmussen, E. N., 2015: VORTEX-Southeast program overview. National Severe Storms Laboratory Rep., 36 pp.

Rauber, R. M., 2003: Handbook of Weather, Climate, and Weather: Atmospheric Chemistry, Hydrology, and Societal Impacts. Wiley. 966 pp.

Raupach, T. H., and A. Berne, 2015: Correction of raindrop size distributions measured by Parsivel disdrometers, using a two-dimensional video disdrometer as a reference. *Atmos. Meas. Tech*., **8**, 343–365.

Richardson, L. F., 1922: Weather prediction by numerical process. Cambridge University Press, Cambridge. Reprinted by Dover (1965, New York) with a new introduction by Sydney Chapman.

Rosenfeld, D., 1999, TRMM observed first direct evidence of smoke from forest fires inhibiting rainfall. *Geophys. Res. Lett*., **26**, 3105–3108.

——, and W. L. Woodley, 2000: Convective clouds with sustained highly supercooled liquid water down to −37°C, *Nature*, **405**, 440–442.

——, and C. W. Ulbrich, 2003: Cloud microphysical properties, processes, and rainfall estimation opportunities. *Meteor. Monogr*., **52**, 237–258.

Saleeby, S. M., W. Berg, S. van den Heever, and T. L'Ecuyer, 2010. Impact of Cloud-Nucleating Aerosols in Cloud-Resolving Model Simulations of Warm-Rain Precipitation in the East China Sea, *J. Atmos. Sci*., **67**, 3916-3930.

Schenkman, A. D., M. Xue, A. Shapiro, K. Brewster, and J. Gao, 2011: Impact of CASA radar and Oklahoma Mesonet data assimilation on the analysis and prediction of tornadic mesovortices in a MCS. *Mon. Wea. Rev.*, **139**, 3422–3445.

——, ——, and ——, 2012: Tornadogenesis in a simulated mesovortex within a mesoscale convective system. *J. Atmos. Sci*., **69**, 3372–3390.

Schneider, R. S., A. R. Dean, S. J. Weiss, and P. D. Bothwell, 2006: Analysis of estimated environments for 2004 and 2005 severe convective storm reports. Preprints, *23rd Conf. on Severe Local Storms,* St. Louis, MO, Amer. Meteor. Soc., 3.5. [https://ams.confex.com/ams/pdfpapers/115246.pdf.].

Seaborn, cited 2021: Seaborn Boxplot [Available online at https://seaborn.pydata.org/generated/seaborn.boxplot.html].

Sherburn, K. D., and M. D. Parker, 2014: Climatology and ingredients of significant severe convection in high-shear, low-CAPE environments. *Wea. Forecasting,* **29**, 854–877.

——, ——, 2019: The development of severe vortices within simulated high-shear, low-CAPE convection. *Mon. Wea. Rev*., **147**, 2189–2216.

Skinner, P. S., Wicker, L. J., Wheatley, D. M., and Knopfmeier, K. H., 2016: Application of Two Spatial Verification Methods to Ensemble Forecasts of Low-Level Rotation, *Wea. Forecasting*, **31**, 713-735.

Smith, B. T., R. L. Thompson, J. S. Grams, C. Broyles, and H. E. Brooks, 2012: Convective modes for significant severe thunderstorms in the contiguous United States. Part I: Storm classification and climatology. *Wea. Forecasting*, **27**, 1114–1135.

Smull, B. F., and R. A. Houze, 1987: Rear inflow in squall lines with trailing stratiform precipitation. *Mon. Wea. Rev.*, **115**, 2869–2889.

Snook, N., and M. Xue, 2008: Effects of microphysical drop size distribution on tornadogenesis in supercell thunderstorms. *Geophys. Res. Lett.,* **35**, L24803.

——, ——, and Y. Jung, 2012: Ensemble probabilistic forecasts of a tornadic mesoscale convective system from ensemble Kalman filter analyses using WSR-88D and CASA radar data. *Mon. Wea. Rev*., **140**, 2126–2146.

——, ——, and ——, 2019: Tornado-resolving ensemble and probabilistic predictions of the 20 May 2013 Newcastle–Moore EF5 tornado. *Mon. Wea. Rev.,* **147**, 1215–1235.

Snyder, C., and F. Zhang, 2003: Assimilation of simulated Doppler radar observations with an ensemble Kalman filter. *Mon. Wea. Rev.*, **131**, 1663–1677.

Spracklen, D. V., K.S. Carslaw, U. Pöschl, A. Rap, and P. M. Forster, 2011: Global cloud condensation nuclei influenced by carbonaceous combustion aerosol. *Atmos. Chem. Phys*., **11**, 9067–9087.

Squires, P., 1958: The microstructure and colloidal stability of warm clouds. *Tellus*, **10**, 256–271.

——, and S. Twomey, 1966: A comparison of cloud nucleus measurements over central North America and Caribbean Sea. *J. Atmos. Sci*., **23**, 401–404.

Stensrud, D. J., and Coauthors, 2009: Convective-scale warn-on-forecast system: A vision for 2020. *Bull. Amer. Meteor. Soc.,* **90**, 1487–1500.

Storer, R. L., S. C. van den Heever, and G. L. Stephens, 2010: Modeling aerosol impacts on convective storms in different environments. *J. Atmos. Sci.*, **67**, 3904–3915.

Stull, R. B., 1988: An introduction to boundary layer meteorology. Kluwer Academic Publishers, Dordrecht, Boston and London, 666 pp.

Sun, J., 2005: Convective-scale assimilation of radar data: Progress and challenges. *Quart. J. Roy. Meteor. Soc.*, **131**, 3439–3463.

Supinie, T. A., Y. Jung, M. Xue, D. J. Stensrud, M. M. French, and H. B. Bluestein, 2016: Impact of VORTEX2 Observations on Analyses and Forecasts of the 5 June 2009 Goshen County, Wyoming, Supercell. *Mon. Wea. Rev.*, **144**, 429-449.

Tanamachi, R. L., L. J. Wicker, D. C. Dowell, H. B. Bluestein, D. T. Dawson, and M. Xue, 2013: EnKF assimilation of high-resolution, mobile Doppler radar data of the 4 May 2007 Greensburg, Kansas, supercell into a numerical cloud model. *Mon. Wea. Rev*., **141**, 625–648.

Tao, W. K., J. P. Chen, Z. Li, C. Wang, and C. Zhang, 2012: Impact of aerosols on convective clouds and precipitation, *Rev. Geophys.,* **50**, RG2001.

Thompson, R. L., R. Edwards, and C. M. Mead, 2004: An update to the supercell composite and significant tornado parameters. Preprints, *22nd Conf. Severe Local Storms,* Hyannis, MA, Amer. Meteor. Soc., P8.1. [https://ams.confex.com/ams/11aram22sls/webprogram/Paper82100.html.].

——, B. T. Smith, A. R. Dean, and P. T. Marsh, 2013: Spatial distributions of tornadic near-storm environments by convective mode. *Electronic J. Severe Storms Meteor.*, **8**, 1–22.

Thurai, M., and V. N. Bringi, 2005: Drop Axis Ratios from a 2D Video Disdrometer, *J. Atmos. Ocean. Technol*., **22**, 966-978.

——, W. Petersen, A. Tokay, C. Schultz, and P. Gatlin, 2011: Drop size distribution comparisons between Parsivel and 2-D video disdrometers. *Adv. Geosci*., **30**, 3–9.

——, V. N. Bringi, W. A. Petersen, and P. N. Gatlin, 2013: Drop Shapes and Fall Speeds in Rain: Two Contrasting Examples, *J. Appl. Meteor.*, **52**, 2567-2581.

——, C. R. Williams, and V. N. Bringi, 2014: Examining the correlations between drop size distribution parameters using data from two side-by-side 2D-video disdrometers. *Atmos. Res.*, **144**, 95–110.

——, and V. N. Bringi, 2018: Application of the generalized gamma model to represent the full rain drop size distribution spectra. *J. Appl. Meteor.*, ***57***, 1197–1210.

Tong, M., and M. Xue, 2005: Ensemble Kalman filter assimilation of Doppler radar data with a compressible nonhydrostatic model: OSS Experiments. *Mon. Wea. Rev.*, **133**, 1789–1807.

Tokay, A., and D. A. Short, 1996: Evidence from tropical raindrop spectra of the origin of rain from stratiform versus convective clouds. *J. Appl. Meteor.,* **35**, 355–371.

——, W. A. Petersen, P. Gatlin, and M. Wingo, 2013: Comparison of raindrop size distribution measurements by collocated disdrometers, *J. Atmos. Ocean. Technol*., **30**, 1672–1690.

——, D. B. Wolff, and W. A. Petersen, 2014: Evaluation of the new version of the laser-optical disdrometer, OTT Parsivel2. *J. Atmos. Oceanic Technol*., **31**, 1276–1288.

Ulbrich, C. W., 1983: Natural variations in the analytical form of the raindrop size distribution. *J. Climate Appl*. *Meteor*., **22**, 1764–1775.

——, and D. Atlas, 1984: Assessment of the contribution of differential polarization to improve rainfall measurements. *Radio Sci*., **19**, 49–57.

——, 1985. The effects of drop size distribution truncation on rainfall integral parameters and empirical relations. *J. Appl. Meteor. Climatol.* **24**, 580–590.

——, 1993: Corrections to empirical relations derived from rainfall disdrometer data for effects due to drop size distribution truncation. *Atmos. Res.,* **34**, 207–215.

——, and D. Atlas, 1998: Rainfall microphysics and radar properties: Analysis methods for drop size spectra. *J. Appl. Meteor.,* **37**, 912–923.

van den Heever, S. C., and W. R. Cotton, 2004: The impact of hail size on simulated supercell storms, *J. Atmos. Sci*., **61**, 1596–1609.

——, G. G. Carrió, W. R. Cotton, P. J. DeMott, and A. J. Prenni, 2006: Impacts of nucleating aerosol on Florida storms. Part I: Mesoscale simulations. *J. Atmos. Sci.,* **63**, 1752–1775.

Vivekanandan, J., G. Zhang, and E. Brandes, 2004: Polarimetric radar estimators based on a constrained gamma drop size distribution model. *J. Appl. Meteor*. **43**, 217–230.

Warner, J., and S. Twomey, 1967: The production of cloud nuclei by cane fires and the effects on cloud droplet concentration. *J. Atmos. Sci*., **24**, 704–706.

——, 1968: A reduction in rainfall associated with smoke from sugar-cane fires: An inadvertent weather modification?. *J. Appl. Meteorol*., **7**, 247–251.

Weisman, M. L., 1992: The role of convectively generated rear-inflow jets in the evolution of long-lived mesoconvective systems. *J. Atmos. Sci.*, **49**, 1826–1847.

——, and R. J. Trapp, 2003: Low-level mesovortices within squall lines and bow echoes. Part I: Their genesis and implications. *Mon. Wea. Rev.,* **131**, 2779–2803.

Xue M, J. Zong, K. K. Droegemeier 1996: Parameterization of PBL turbulence in a multi-scale non-hydrostatic model. Preprints, *Eleventh Conference on Numerical Weather Prediction*, Norfolk, VA, Amer. Meteor. Soc., 363–365 pp.

——, K. K. Droegemeier, and V. Wong, 2000: The Advanced Regional Prediction System (ARPS) - A multi-scale nonhydrostatic atmospheric simulation and prediction model. Part I: Model dynamics and verification. *Meteor. Atmos. Phys*., **75**, 161–193.

——, ——, and ——, A. Shapiro, K. Brewster, F. Carr, D. Weber, Y. Liu and D. Wang, 2001: The Advanced Regional Prediction System (ARPS) – A multi-scale nonhydrostatic atmospheric simulation and prediction tool. Part II: Model physics and applications. *Meteor. Atmos. Phys*., **75**, 143–165.

——, D. H. Wang, J. D. Gao, K. Brewster, and K. K. Droegemeier, 2003: The Advanced Regional Prediction System (ARPS), storm-scale numerical weather prediction and data assimilation. *Meteor. Atmos. Phys.*, **82**, 139–170.

——, M. Tong, and K. K. Droegemeier, 2005: Impact of radar configuration and scan strategy on assimilation of radar data using ensemble Kalman filter. Preprints, *Ninth Symp. on Integrated Observing and Assimilation Systems or the Atmosphere, Oceans, and Land Surface*, San Diego, CA, Amer. Meteor. Soc., 9.3. [http://ams.confex.com/ams/pdfpapers/86681.pdf.].

——, M. Hu, and A. D. Schenkman, 2014: Numerical prediction of the 8 May 2003 Oklahoma City tornadic supercell and embedded tornado using ARPS with the assimilation of WSR-88D Data. *Wea. Forecasting*, **29**, 39–62.

Yue, Z., and Coauthors, 2019: Automated Mapping of Convective Clouds (AMCC) thermodynamical, microphysical, and CCN properties from SNPP/VIIRS satellite data. *J. Appl. Meteor. Climatol.,* **58**, 887–902.

Ziegler, C. L., 1985: Retrieval of thermal and microphysical variables in observed convective storms. Part 1: Model development and preliminary testing. *J. Atmos. Sci.,* **42**, 1487–1509.